ISSN Print: 2518-4245
ISSN Online: 2518-4253
Vol. 62(2), June 2025

PROCEEDINGS
OF THE PAKISTAN ACADEMY OF SCIENCES:
A. Physical and Computational Sciences

PAKISTAN ACADEMY OF SCIENCES
ISLAMABAD, PAKISTAN

Proceedings of the Pakistan Academy of Sciences: Part A Physical and Computational Sciences

***President*:** Kauser Abdullah Malik
***Secretary General*:** M. Aslam Baig
***Treasurer*:** Saleem Asghar

Proceedings of the Pakistan Academy of Sciences A. Physical and Computational Sciences is the official flagship, the peer-reviewed quarterly journal of the Pakistan Academy of Sciences. This open-access journal publishes original research articles and reviews on current advances in the field of Computer Science (all), Materials Science (all), Physics and Astronomy (all), Engineering Sciences (all), Chemistry, Statistics, Mathematics, Geography, Geology in English. Authors are not required to be Fellows or Members of the Pakistan Academy of Sciences or citizens of Pakistan. The journal is covered by Print and Online ISSN, indexed in Scopus, and distributed to scientific organizations, institutes and universities throughout the country, by subscription and on an exchange basis.

Editor-in-Chief:

M. Javed Akhtar, Pakistan Academy of Sciences, Islamabad, Pakistan; editor@paspk.org

Managing Editor:

Ali Ahsan, Pakistan Academy of Sciences, Islamabad, Pakistan; editor@paspk.org

Discipline Editors:

Chemical Sciences: Guo-Xin Jin, Inorganic Chemistry Institute, Fudan University, Shanghai, China
Chemical Sciences: Haq Nawaz Bhatti, Department of Chemistry University of Agriculture, Faisalabad, Pakistan
Geology: Peng Cui, Key Laboratory for Mountain Hazards and Earth Surface Process, CAS, Institute of Mountain Hazards & Environment, CAS Chengdu, Sichuan, People's Republic of China
Computer Sciences: Sharifullah Khan, Faculty of Electrical, Computer, IT & Design(FECID), Pak-Austria Fachhochschule: Institute of Applied Sciences and Technology (PAF-IAST), Mange, Haripur, Pakistan
Engineering Sciences: Akhlesh Lakhtakia, Evan Pugh University Professor and The Charles G. Binder (Endowed), Engineering Science and Mechanics, Pennsylvania State University, University Park, USA
Mathematical Sciences: Ismat Beg, Department of Mathematics and Statistical Sciences, Lahore School of Economics, Lahore, Pakistan
Mathematical Sciences: Jinde Cao, Department of Mathematics, Southeast University Nanjing, P. R. China
Physical Sciences: Asghari Maqsood, Department of Physics, E-9, PAF Complex Air University, Islamabad
Physical Sciences: Niemela J. Joseph, The Abdus Salam International Center for Theoretical Physics (ICTP-UNESCO), Trieste- Italy

Editorial Advisory Board:

Saeid Abbasbandy, Department of Mathematics, Imam Khomeini International University Ghazvin, 34149-16818, Iran
Muazzam Ali Khan Khattak, Department of Computer Science, Quaid-i-Azam University, Islamabad, Pakistan
Muhammad Sharif, Department of Mathematics, University of the Punjab, Lahore, Pakistan
Faiz Ullah Shah, Department of Civil, Environmental and Natural Resources Engineering, Lulea University of Technology, Luleå, Sweden
Kashif Nisar, Lecturer of Computer Science, School of Arts and Sciences, The University of Notre Dame, Australia
Guoqian Chen, Laboratory of Systems Ecology and Sustainability Science, College of Engineering, Peking University, Beijing, China
Bhagwan Das, Department of Electronic Engineering, Quaid-e-Awam University of Engineering, Science and Technology Nawabshah, Sindh, Pakistan
Muhammad Sadiq Ali Khan, Department of Computer Science, University of Karachi, Pakistan

Annual Subscription: **Pakistan:** Institutions, Rupees 8000/-; Individuals, Rupees 4000/- (Delivery Charges: Rupees 300/-)
Other Countries: US$ 200.00 (includes air-lifted overseas delivery)

© *Pakistan Academy of Sciences.* Reproduction of paper abstracts is permitted provided the source is acknowledged. Permission to reproduce any other material may be obtained in writing from the Editor.
The data and opinions published in the *Proceedings* are of the author(s) only. The *Pakistan Academy of Sciences* and the *Editors* accept no responsibility whatsoever in this regard.

HEC Recognized; Scopus Indexed

Published by **Pakistan Academy of Sciences**, 3 Constitution Avenue, G-5/2, Islamabad, Pakistan
Email: editor@paspk.org; **Tel:** 92-51-920 7140 & 921 5478; **Websites:** www.paspk.org/proceedings/; www.ppaspk.org

Printed at **Graphics Point.,** Office 3-A, Wasal Plaza, Fazal-e-Haq Road Blue Area Islamabad.
Ph: 051-2806257, **E-mail:** graphicspoint16@gmail.com

PROCEEDINGS OF THE
PAKISTAN ACADEMY OF SCIENCES: PART A
Physical and Computational Sciences

CONTENTS

Volume 62, No. 2, June 2025 **Page**

Research Articles

Instructions for Authors

Submission of Manuscripts: Manuscripts may be submitted as an e-mail attachment at editor@paspk.org or submit online at http://ppaspk.org/index.php/PPASA/about/submissions. Authors must consult the ***Instructions for Authors*** at the end of this issue or at the Website: www.paspk.org/proceedings/ or www.ppaspk.org.

Proceedings of the Pakistan Academy of Sciences: A Physical and Computational Sciences 62(2): 97-106 (2025)
Copyright © Pakistan Academy of Sciences
ISSN (Print): 2518-4245; ISSN (Online): 2518-4253
http://doi.org/10.53560/PPASA(62-2)688

Pakistan Academy of Sciences

Research Article

IoT based Oxygen Availability Monitoring and Automatic Control System for Clinical Patients

Sunardi Sunardi[1] and Muhammad Sholihul Abdillah[2*]

[1]Department of Electrical Engineering, Universitas Ahmad Dahlan, Yogyakarta, Indonesia
[2]Department of Electrical Engineering, Universitas Muhammadiyah Ponorogo, Ponorogo, Indonesia

Abstract: Oxygen is essential for human survival, comprising 2% of total body weight yet the brain consumes approximately 20% of the body's oxygen. Oxygen deficiency in the brain causes hypoxia, potentially leading to irreversible damage, liver dysfunction, and even fatality. Ensuring stable oxygen delivery in healthcare facilities requires an efficient centralized oxygen system. According to Indonesia's Ministry of Health Regulation No. 4 of 2016, centralized systems must maintain an output pressure of 4-5 bar. This study addresses the challenge of ensuring uninterrupted oxygen supply by developing an automatic supply-switching system. Utilizing programmable logic controller (PLC) Outseal control and IoT-based monitoring, the system detects cylinder pressure levels, switches supply to cylinders with pressure > 4 bar, and provides real-time data on pressure, flow, and cylinder status via human machine interface (HMI) and the Haiwell Cloud smartphone application. Rigorous testing demonstrated high precision, with error rates of 0.18% for Pressure Sensor A, 0.079% for Pressure Sensor B, and 0.89% for the flow sensor. This innovation enhances reliability and safety in medical oxygen systems.

Keywords: Human Machine Interface, Internet of Things, Automatic, PLC Outseal, Hypoxia.

1. INTRODUCTION

Oxygen is vital for human survival, constituting 2% of body weight but sustaining critical organs, particularly the brain, which consumes 20% of the body's oxygen. Hall and Hall [1] found that hypoxia—oxygen deprivation—can cause irreversible brain damage, neurological disorders, or death within minutes. Healthcare facilities, including hospitals and school health units, play a crucial role in ensuring oxygen availability for emergencies, particularly respiratory conditions. In schools, sudden incidents, such as shortness of breath during physical activities, demand immediate access to oxygen. However, many health units rely on single-cylinder systems, posing risks during simultaneous emergencies due to supply limitations. A survey at Ponorogo Muslimat Hospital and SMKN 1 Jenangan's health unit identified significant differences in oxygen supply management. Hospitals use centralized oxygen systems with backup cylinders, while schools depend on single-cylinder approaches. In centralized systems, oxygen supply switches manually to a backup cylinder upon depletion, triggered by an alarm. Although effective, manual switching introduces risks, including delays and operator errors. Mulyanto *et al.* [2] referred to the Indonesian Ministry of Health Regulation No. 4 of 2016 mandates that centralized oxygen systems maintain a minimum pressure of 4-5 bar, incorporating pipelines, shut-off valves, and medical gas alarms. Compliance with these standards in resource-constrained settings like schools remains a challenge. The IoT offers transformative potential by enabling real-time communication between devices, sensors, and users. Yudhanto and Aziz [3] investigated IoT systems improve monitoring and control by providing continuous access to system data, facilitating proactive interventions and decision-making. This study addresses the challenge of reliable oxygen supply by developing

---

Received: April 2025; Revised: May 2025; Accepted: June 2025
* Corresponding Author: Muhammad Sholihul Abdillah <justsholih@gmail.com>

an automatic control and monitoring system for oxygen supply in clinical settings based on internet of things (IoT). Utilizing a solenoid valve and programmable logic controller (PLC) out-seal, the system automates cylinder switching based on pressure sensor data. Integrated with a human machine interface (HMI) and cloud platform, it provides real-time monitoring and alerts via smartphones [4, 5]. By leveraging IoT, this solution minimizes manual intervention, ensures consistent oxygen availability, and enhances emergency preparedness, particularly in school health units.

2. MATERIALS AND METHODS

Numerous studies on the topic being discussed contribute to a more comprehensive understanding and offer insights into the background and main aspects being examined [6]. The study by Hendryani *et al.* [7] focused on monitoring oxygen cylinder pressure. The system successfully detected pressure levels below the standard threshold and, upon detection, automatically switched the primary gas cylinder to the secondary one. The system was developed using the Atmega328 microcontroller. While this study demonstrated a basic pressure-monitoring and switching mechanism, it lacked advanced features such as integrated flow monitoring or remote accessibility. Another study by Haryanto [8] employed the MPX 5700 sensor to detect medical gas pressure. An alarm was triggered when the pressure dropped below 150 kPa. Additionally, when the oxygen pressure in the main cylinder was depleted, the system automatically switched to a backup cylinder. The device interface, built using the Arduino WeMos D1 R1 WiFi UNO ESP8266 microcontroller, incorporated IoT-based monitoring via the telegram application. While the study effectively integrated internet of things (IoT), its scope was limited to pressure monitoring and lacked advanced control mechanisms. In a related work Nasrullah *et al.* [9] developed a system capable of real-time monitoring and displaying oxygen gas volume on a PC. A water flow sensor detected oxygen flow, while an ATMega32 microcontroller handled data processing and control. Although this study enabled central monitoring, it primarily focused on flow measurement without addressing automated switching or IoT integration. In the same way, Agustian *et el.* [10] has explored an IoT-enabled system for monitoring oxygen cylinder levels. The system used a Node MCU V3 microcontroller, with data displayed on a 2 × 16 LCD. When the system detected pressure levels below 10%, a buzzer was triggered, and the display alerted users about oxygen depletion. Data management and visualization were carried out using the IoT platform ThingSpeak; however, the system required extensive integration with HMI controls.

Although, previous studies have addressed oxygen cylinder pressure monitoring, automated switching, and partial IoT integration, a significant research gap remains in developing a unified system that combines these features with flow monitoring, advanced automation, and a user-friendly IoT-connected HMI interface. Current solutions focus on isolated aspects-pressure detection, IoT-based alerts, or flow measurement, but fail to provide a holistic approach for monitoring both pressure and flow simultaneously or enabling remote access and control through an integrated HMI. To address these gaps, the aims of the present research are:

- Integrate a pressure sensor for monitoring cylinder and automating valve switching between two cylinders.
- Incorporate a flow sensor to monitor the volume of distributed oxygen in real time.
- Develop a comprehensive HMI for seamless control and visualization of cylinder pressure and oxygen flow.
- Leverage IoT connectivity for remote monitoring and control via smartphones or computers, enhancing accessibility and operational efficiency.

In contrast to previous studies, our approach integrates pressure and flow monitoring within a unified system, incorporates PLC Outseal for enhanced control, and leverages IoT-enabled HMI for real-time visualization and remote accessibility. This combination provides a more comprehensive and reliable solution for oxygen monitoring. The system is designed under the assumption that merging flow and pressure monitoring with IoT and HMI technologies will improve both reliability and user interaction; this will eliminate the shortcomings of earlier models, which lacked such integration. The proposed design ensures continuous monitoring of critical parameters, including pressure thresholds and flow rates, while enabling automated responses to minimize the risk of oxygen depletion. IoT connectivity and HMI functionality further enable remote access and control, directly addressing existing limitations in hospital oxygen management systems. By addressing these gaps, our research seeks to make a substantial contribution to the field of medical gas monitoring systems. The following theories are presented as the foundation for conducting this research, with the aim of detailing conceptual framework and theoretical foundation that will guide development and implementation of this study [11].

The IoT offers innovative solutions to current challenges by integrating physical and virtual systems via advanced ICT [12]. Defined by Kevin Ashton in Making Sense of IoT, it connects sensors to the internet, enabling seamless data sharing and applications [13]. IoT allows devices to sense their environment and integrate into daily life. In healthcare, IoT connects medical devices for remote monitoring, reducing the need for physical visits and associated costs. Centralized monitoring systems enable real-time data tracking, improving patient care and reducing expenses, aligning with modern healthcare advancements and enhancing efficiency.

Programmable Logic Controller (PLC) is a digital device designed for industrial automation, managing inputs, processing data, and controlling outputs to operate machines efficiently. PLCs execute functions like logic, timing, and sequencing through programmable memory, offering reliability and flexibility in automation systems [14]. This study employs the Outseal Nano v5 PLC, an open-source automation solution developed by Indonesian engineers using Arduino-based technology. Its affordability and customizable hardware make it a practical choice for cost-sensitive applications [15]. The Outseal PLC is programmed using ladder diagrams via Outseal Studio, a visual platform with an intuitive interface in Indonesian language [16]. Once programming is transferred, the PLC operates autonomously without needing a continuous connection. Additionally, the Modbus protocol, a widely adopted standard for reliable data exchange, facilitates communication between the Outseal PLC and other devices, ensuring seamless integration in automated systems [17].

HMI connects users with machines, enabling intuitive system interaction. It provides real-time visualizations of operations, including sensor data, alarms, and graphical trends, ensuring effective supervision and control. Communication between HMI and controllers uses RS232, RS485, USB, or Ethernet ports [18]. Input data from sensors or actuators is processed by a PLC and visualized on HMI screens. In manufacturing, HMI typically functions as a Graphical User Interface (GUI), offering user-friendly displays of machine conditions, control elements, alarms, and performance data via graphs or tables [19]. This facilitates efficient decision-making and enhances operator-machine interactions.

The pressure sensor operates by converting mechanical strain into electrical signals, enabling the measurement of pressure from both liquids and gases. The principle behind its function is based on the change in the electrical resistance of the conductor material, which occurs as the length and cross-sectional area of the material change. When pressure is applied to the sensor, it induces deformation or bending of the wire, leading to a change in its resistance. The pressure transmitter, a type of pressure sensor used in this system, is highly effective for measuring pressure in industrial processing systems [20]. A flow sensor is a device used to measure the flow rate of gases or vapors. Flow measurement typically involves a transducer and a transmitter. The flow sensor, as a key component, is commonly integrated into flow meters [21].

A solenoid valve, features a coil that drives a piston, which can be activated by alternating current (AC) or direct current (DC) passing through the coil/solenoid. The solenoid valve typically has three main ports: the inlet, outlet, and exhaust. The inlet port is where pressurized air enters the valve, while the outlet port is where pressurized air exits once the valve is opened. When the solenoid coil is supplied with voltage, it generates a magnetic field that moves the piston within the valve. The piston's movement alters the valve's position, enabling the flow of air from the valve to the connected system [22]. The method is a systematic approach employed by researchers to collect the necessary data in the process of designing and constructing a device [23, 24].

2.1. Device Planning Method

Device planning method is designed to facilitate the planning, design and evaluation processes in preparation for the development and construction of the device, including observation, interview and discussion methods [25]. In this method there are four parts, namely component planning, system design, control design, and hardware planning, and software planning. Here is an explanation of these parts:

2.1.1. Component planning

The development of this system requires meticulous planning for component selection. Proper identification of each component is crucial to streamline the design process, enabling the creation of both electrical and mechanical designs [26]. This structured approach ensures that all necessary elements are effectively integrated into the system, optimizing performance and functionality; power supply (switching 24Vdc 2A), outseal PLC (nano v5.1), HMI (haiwell c7s-w), pressure sensor (transmitter sensor), flow sensor (SFAB-200U), solenoid valve (valve 3/2 pneumatic), tower lamp (red, yellow, and green), buzzer (24vdc 22mm), relay (my2n 24vdc), MCB (4A), box panel (30 × 40 cm), duct cable (25 × 40 mm), and block terminal.

2.1.2. System design

The key components of the design are described as follows:
- Tabung A and Tabung B, these are 2 medical-grade oxygen cylinders designated for A and B.
- Regulator A and Regulator B, each oxygen cylinder is equipped with a dedicated pressure regulator to control the oxygen flow.
- Sensor tekanan A and sensor tekanan B, these pressure sensors are installed at the outlet of each regulator on the flow paths of Cylinder A and Cylinder B to monitor oxygen pressure.
- Solenoid valves (SVA and SVB), are installed downstream of the pressure sensors on each flow path from Cylinder A and Cylinder B, respectively.
- Shuttle valve (or gate), positioned where the flow paths of Cylinder A and B converge, ensuring a seamless transition between oxygen supplies.
- Flow sensor, located downstream of the shuttle valve. It measures the volume of oxygen flowing out of the system.
- Sistem kontrol (control system), installed adjacent to the medical oxygen flow installation and serves as the central control hub for all actuators. Sensors and actuators are connected to the control panel, indicated by orange lines in the system design. Figure 1 highlights the placement of sensors and actuators [27]. This configuration ensures the system's ability to monitor and control oxygen supply, supporting real-time adjustments and operational reliability.

2.1.3. Control design

Encompasses 2 primary components: the system block diagram and the wiring diagram. The system block diagram, this provides a comprehensive overview of the system architecture, illustrating the interaction between various inputs, the PLC control unit, outputs, and the Human-Machine Interface (HMI) [28]. Figure 2 shows the system workflow, comprising input, process, output, and monitoring components. Two pressure sensors and an SFAB flow sensor measure oxygen pressure in Cylinders A and B and flow volume. Data is processed by

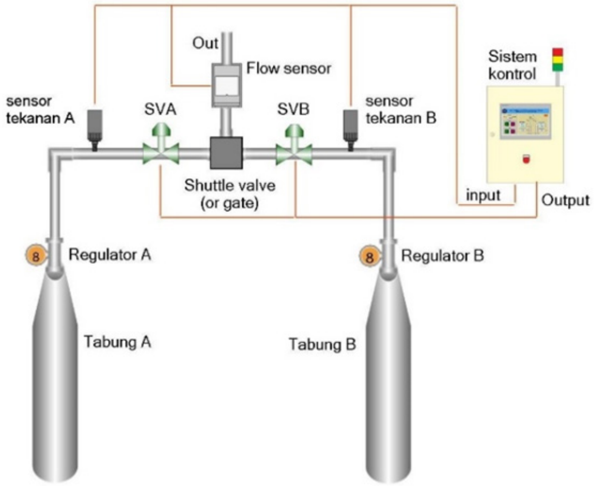

Fig. 1. Device system design.

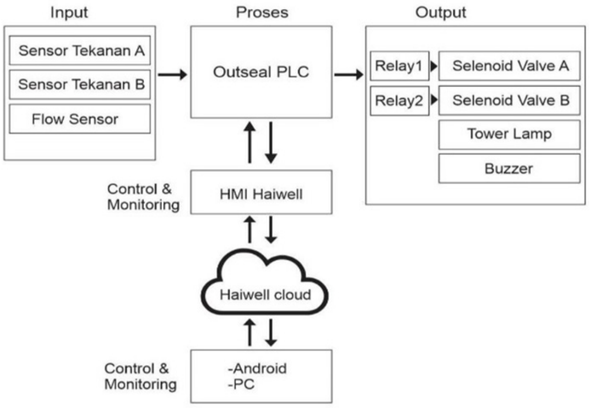

Fig. 2. System block diagram.

Outseal PLC, controlling solenoid valves for oxygen flow, a tower lamp for signals, and a buzzer for alerts. Monitoring is done through Haiwell HMI with IoT features, providing real-time visualization of oxygen pressure, flow, and system control.

The wiring diagram was created as a reference for connecting cables between the various components. The wiring design was developed using AutoCAD software. The wiring as illustrated in Figure 3 shows the relay contact outputs connected to the actuators and indicators, where the solenoid valve, buzzer, and indicator lights are connected through their respective relay contacts, with the following specifications:

(a) Contact no. K1 is connected to solenoid valve A (SVA).

(b) Contact no. K2 is connected to solenoid valve B (SVB).

(c) Contact no. K3 is connected to the buzzer LED (2H1).

(d) Contact no. K4 is connected to the green tower lamp (53H2).

(e) Contact no. K5 is connected to the yellow tower lamp (53H3).

(f) Contact no. K6 is connected to the red tower lamp (53H4).

2.1.4. Hardware planning

Hardware planning involves two main aspects: the control panel design and the medical oxygen flow system installation. These aspects details are given below:

(1) Control panel design: The control panel is housed in a 30 × 40 cm enclosure. Figure 4 illustrates the layout of both the front and internal components of the control panel. The front panel includes the HMI, a tower lamp, and a buzzer, with each component installed through appropriately sized cutouts on the enclosure. The layout shown in Figure 4 is designed for efficient wiring and a neat appearance. Key components are strategically placed for ease of installation and maintenance. The top section houses the MCB, power supply, and Outseal controller. The middle section contains relays, and the bottom row features terminal connectors for external interfaces. This arrangement ensures reliable operation and facilitates troubleshooting.

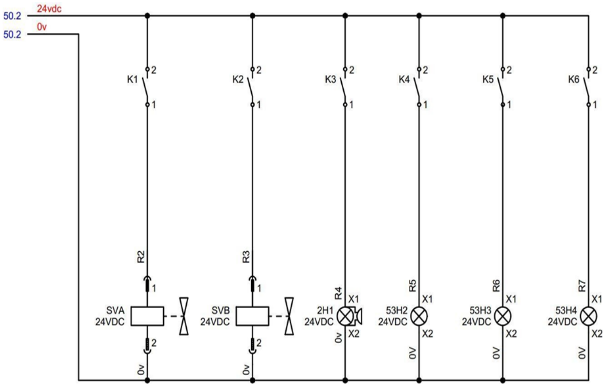

Fig. 3. Wiring diagram of the component output.

(2) Medical oxygen flow system installation: Figure 5 depicts the installation of the medical oxygen flow system. The configuration starts with oxygen cylinders A and B.

- For Cylinder A:

- Oxygen exits the cylinder and passes through Solenoid Valve A (SVA).
- A pressure sensor is installed between SVA and the cylinder to monitor pressure.

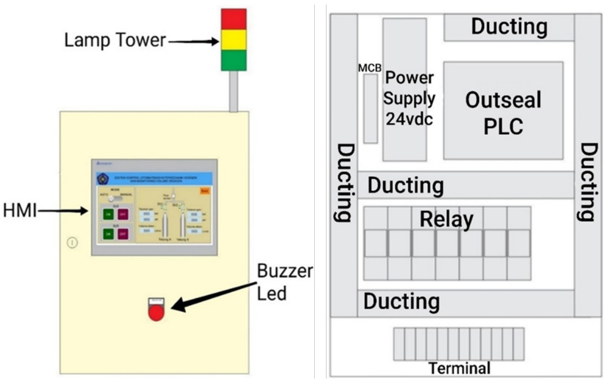

Fig. 4. Control system design, where the left side represents the external form, and the right side represents the internal form.

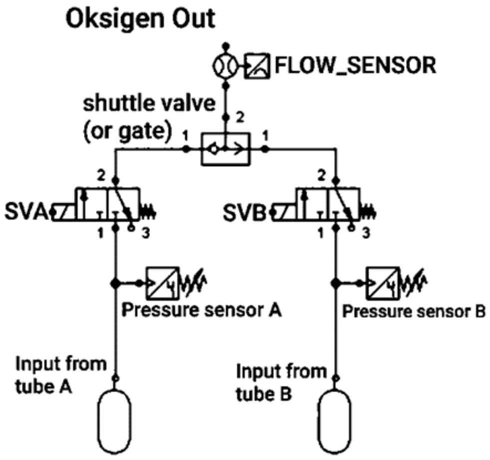

Fig. 5. Medical oxygen flow installation design.

- The output of SVA is routed to an OR gate, which then directs the flow to the flow sensor.
- After the flow sensor, the oxygen is distributed to the intended application.

\- For Cylinder B:

- Oxygen exits the cylinder and passes through Solenoid Valve B (SVB).
- A pressure sensor is installed between SVB and the cylinder to monitor pressure.
- The output of SVB is also routed to the OR gate, then to the flow sensor for distribution.

The oxygen flow system is connected using 4 mm pneumatic tubing, ensuring secure and efficient linkage between components. This design provides a seamless transition between oxygen sources, supporting consistent medical oxygen delivery.

2.1.5. Software planning

Process comprises two main components: PLC and HMI programming planning. Each component is described as follow:
(1) PLC Programming Planning: The first step in PLC programming planning is identifying PLC address allocation based on the wiring diagram. This step ensures that sensors and actuators are properly mapped to their respective addresses before programming the PLC.
(2) HMI Programming Planning: The HMI design serves as the interface for control and monitoring, and it is developed to provide detailed insights into the condition of each oxygen cylinder.

2.2. Device Design

Device design is a systematic approach that integrates various engineering principles to create efficient and effective devices tailored to meet specific user needs and requirements [29]. There are two parts that will be explained, namely hardware design and software design.

2.2.1. Hardware design

The system design comprises two main stages: the design of the equipment box and component layout, and the wiring installation design. Each stage is detailed below:
(1) Equipment Box and Component Layout Design: This design uses a 30×40cm panel box. The front panel features cutouts for components such as the HMI and buzzer, while a tower lamp is mounted on top as an indicator. Inside the box, space is organized to accommodate all components, ensuring efficient wiring connections. This layout promotes a neat and organized control system for optimal functionality.
(2) Wiring Installation Design: Following the component layout design, the next stage involves wiring installation. The wiring design adheres to the circuit diagram developed during the planning phase. Components are interconnected using appropriate wires, with each wire end fitted with cable lugs that match the wire gauge. The wiring process is carried out using basic hand tools such as screwdrivers, wire cutters, and crimping pliers. These tools ensure secure and reliable connections between components, contributing to the system's operational integrity.

2.2.2. Software design

The oxygen monitoring and control system requires specific software tools for design and implementation:
(1) Outseal Studio: Essential for PLC programming, Outseal Studio creates programs based on predefined flowcharts, processes sensor data, displays information on the HMI, and controls system output. After validation ensures compliance with design specifications. Debugging is performed if discrepancies arise before uploading the final program to Outseal Nano V5.1.
(2) Haiwell Cloud SCADA Designer: Used for HMI interface design, this software displays sensor data and system status. Validation ensures accuracy, and any errors are corrected before uploading the interface to the Haiwell HMI device.
(3) Haiwell Cloud Application: Installed on a smartphone, this app enables real-time monitoring of oxygen pressure and availability via the internet. Users can access system data remotely, ensuring continuous oversight of oxygen supply conditions, enhancing system efficiency and reliability.

2.3. Device Testing Method

The device testing method involves processes aimed at identifying and addressing potential software errors [30]. The first step is a thorough review of the developed program, where the author evaluates and corrects any errors or bugs. This step ensures the optimal functioning of the device components

[31-33]. Testing the automatic control and monitoring system for oxygen availability assesses overall system performance, ensuring it aligns with expected principles and functions without errors. This stage helps verify the device's reliability and confirms its readiness for practical application.

3. RESULTS AND DISCUSSION

The design results, illustrated in Figure 6, shows the complete internal arrangement of components within the enclosure, including proper wiring and layout. Visible in the upper section is the Outseal PLC module mounted on the DIN rail, responsible for system logic control. Below it are multiple relays and contactors used to manage connected actuators and indicators. The power supply unit is located on the upper left side. A tower signal light is mounted on the top of the cabinet to provide operational status feedback (green for normal, yellow for warning, red for error). The right-side door contains wiring routed through protective flexible spirals, ensuring cable safety and flexibility when the door is opened or closed. The black component with a red, yellow, and green wire is the emergency switch, yet to be mounted, which serves as the primary user interface for safety shutdown. This design ensures clear signal communication, structural durability, and operational reliability in demanding environments.

The result of the oxygen flow installation design is illustrated in Figure 7. This was constructed using an acrylic board, adhering closely to the planned design specifications for the medical oxygen flow system. Precision in the design process is critical to prevent potential leakage in the system. Connections involving threaded joints were sealed with insulating tape to ensure airtight and secure connections. This approach minimizes risks and ensures the system meets the necessary safety and performance standards for medical applications.

The software design for the PLC program was developed using Outseal Studio, with the hardware configured to Nano V5. The design process began with the creation of PLC tag variables, defining the input and output parameters required for the Outseal system. A ladder diagram was then constructed, guided by the program's flowchart. To ensure that the system meet operational requirements, the program underwent thorough functionality testing. The HMI was designed and implemented using Haiwell Cloud SCADA Designer. The process started with the creation of a new project, selecting the Haiwell C7S HMI type, and configuring the interface to connect the HMI with the Outseal PLC. This configuration adhered to the specifications of both interfaces. Input and output variable tags were created to address elements in the HMI visualization. After completing the visualization design, the project was downloaded to the Haiwell HMI device for testing. Once verified, network settings were configured to connect the HMI to Haiwell Cloud, enabling remote monitoring and control through an internet connection. Wi-Fi connectivity was established to ensure seamless integration with Haiwell Cloud for real-time data access. The Haiwell Cloud application, installed on smartphones, provides remote access to the HMI device. Synchronization is facilitated by scanning the device's barcode, which connects the smartphone to the Haiwell Cloud app. This setup enables users to remotely monitor and control the system from any location with internet connectivity. This feature enhances system accessibility and operational

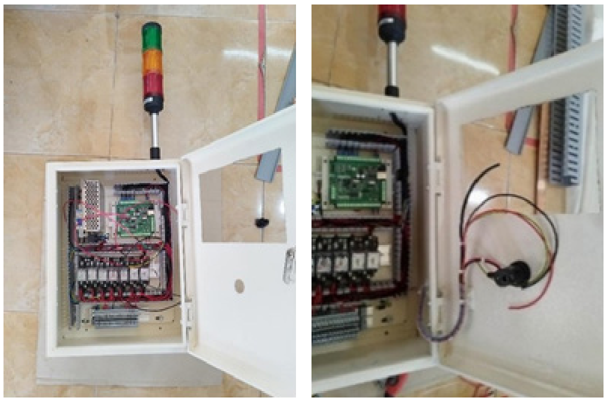

Fig. 6. Hardware of the electrical control panel.

Fig. 7. The oxygen flow installation.

efficiency. Sensor testing is essential to calibrate and verify the accuracy of the sensor in detecting the target object. The testing process involves comparing the sensor's output values with the actual reference values, ensuring that the difference is either zero or as close to zero as possible. Once the test data is obtained, the sensor measurement error is calculated using the Equation (1):

$$Error(\%) = \left(\frac{Sensor\ Value - Actual\ Value}{Actual\ Value}\right) \times 100\% \quad (1)$$

Tables 1, 2, and 3 present the results of sensor accuracy testing and error analysis for the system's core sensing components. Specifically, Tables 1 and 2 evaluate the pressure sensors installed on Oxygen Cylinder A and Cylinder B, respectively. In these tests, sensor readings (in bar) were compared against reference values obtained from a calibrated analog manometer gauge. The percentage error was then calculated to assess the precision and consistency of each pressure sensor under varying pressure levels. Table 3 displays the flow rate sensor testing, in which sensor outputs (in liters per minute) were validated using a manual flowmeter as the reference. Similar to the pressure tests, the percentage error between the sensor and the flowmeter readings was computed to evaluate accuracy. The combined results from all three tables serve to validate the reliability of the system's sensing components. Low error percentages across a range of operating conditions indicate that the sensors provide accurate and dependable readings, supporting their use in critical healthcare environments. This testing procedure is essential to ensure the system's suitability for real-time monitoring of oxygen supply and patient safety, especially in clinics or hospitals relying on automated control and alert systems.

Figure 8 shows the synchronized graphical user interface displayed on both the Human-Machine Interface (HMI) screen and a smartphone, demonstrating the system's remote accessibility via IoT. The interface displays real-time oxygen tank pressure levels (measured in psi), sensor statuses (green indicators for normal conditions), and flow direction to the patient. The charted areas reflect digital readings from the pressure sensors installed on both oxygen cylinders (Tabung A and Tabung B), with switching valve indicators (SV1 and SV2) positioned centrally to represent automatic control of oxygen flow. The matching displays confirm that

Table 1. Pressure sensor testing for Cylinder A.

Sr. No.	Manometer gauge (bar)	Pressure sensor (bar)	*Error (%)*
1	2	1.99	-0.5%
2	3	2.98	-0.66%
3	4	3.95	-1.25%
4	5	5	0%
5	6	6.07	1.16%
6	7	7.07	1%
7	8	8.10	1.25%
8	9	9.13	1.4%

Table 2. Pressure sensor testing for Cylinder B.

Sr. No.	Manometer gauge (bar)	Pressure sensor (bar)	*Error (%)*
1	2	1.99	-0.5%
2	3	2.98	-0.66%
3	4	3.93	-1.75%
4	5	4.99	-0.2%
5	6	6.04	0.66%
6	7	7.04	0.57%
7	8	8.13	1.62%
8	9	9.08	0.88%

Table 3. Flow sensor testing.

Sr. No.	Flowmeter manual (L/min)	*Flow sensor* (L/min)	*Error (%)*
1	2	2.0	0 %
2	4	4.0	0 %
3	6	6.1	1.6 %
4	8	8.1	1.25 %
5	10	10.0	0 %
6	12	12.2	1.6 %
7	14	14.1	0.71 %
8	16	16.3	1.87 %

Fig. 8. IoT-Based Monitoring Interface on HMI and Smartphone.

the data captured by the microcontroller is accurately transmitted via the internet to the smartphone interface. This ensures real-time monitoring and fault detection, such as alarm triggers in case of pressure drops or flow failures, thereby enhancing operational safety and enabling remote supervision.

4. CONCLUSIONS

The automatic control and monitoring system for medical oxygen supply demonstrated effective performance. It measures oxygen pressure up to 10 bar (10.19 kg/cm²) and processes sensor data using a PLC Outseal to control solenoid valves and read flow sensor data. Pressure sensors exhibited high accuracy, with average errors of 0.18% (Sensor A) and 0.079% (Sensor B), while the flow sensor achieved an average error of 0.89%. The system automatically switches cylinders when pressure drops below 4 bar, activating alarms and solenoid valves to ensure continuous supply. An emergency alarm is triggered if both cylinders fall below 4 bar. The Human Machine Interface (HMI) visualizes real-time oxygen pressure, flow volume, and system status. Remote monitoring via the IoT-enabled Haiwell Cloud app allows users to track oxygen availability anytime, anywhere. Future improvements include adding analog input modules, adopting higher-capacity pressure sensors, and enhancing measurement precision to 0.01 bar.

5. CONFLICT OF INTEREST

The authors declare no conflict of interest.

6. REFERENCES

1. J.E. Hall and M.E. Hall (Eds.). Guyton and Hall Textbook of Medical Physiology. 14th Edition. *Elsevier* (2020).
2. M. Mulyanto, E. Jaenuri, and G. Gunawan. Pressure monitoring device on medical gas cylinders with SMS (Short Message Service) notification. *Hospital Technology and Mechatronics* 1(1): 58-67 (2020).
3. Y. Yudhanto and A. Azis (Eds.). Introduction to Internet of Things (IoT) Technology. 1st Edition. *UNS Press* (2019).
4. M.S. Abdillah, G.A. Buntoro, R.I. Vidyastari, D. Desriyanti, J.S. Habiby, M. Mohsin, and D.F. Laistulloh. Smart Wheelchair from Lecture Chair with Automatic Security Code for Users. Patent of Computer Program No. 000651163. *Online Intellectual Property Data System*, *UMPO, Ponorogo, Indonesia* (2024).
5. E.K. Mekki, A. Kessar, and R. Mouaz. Design of a printed circuit board for real-time monitoring and control of pipeline's cathodic protection system via IoT and a cloud platform. *International Journal of Engineering, Transactions C: Aspects* 36(9): 1667-1676 (2023).
6. M.S. Abdillah, F. Masykur, and S. Sunardi. Design and construction of a smart wheelchair from a lecture chair using power window motors with smartphone control for disability. *International Journal of Engineering, Transactions C: Aspects* 38(6): 1397-1404 (2025).
7. A. Hendryani, V. Nurdinawati, and N. Dharma. Design of manifold with pressure controller for automatic exchange of oxygen gas cylinders in hospital. *TEKNIK* 42(1): 45-51 (2021).
8. H. Haryanto. Design and Construction of an IoT (Internet of Things) Based Medical Gas Pressure Monitoring System Using Arduino and MPX 5700 Sensor at DR. SOERADJI TIRTONEGORO KLATEN Hospital. Bachelor Thesis. *Universitas Widya Dharma Klaten*, *Klaten, Indonesia* (2021).
9. M.A. Nasrullah, D.H. Andayani, and E. Yulianto. Computer-Based Medical Oxygen Gas Usage Volume Monitoring Center. *Jurnal Teknokes* 12(2): 50-58 (2019).
10. R. Agustian, K. Erwansyah, and H. Jaya. Design and Manufacturing of IoT-Based Oxygen Cylinder Monitoring Device Using Node Mcu V3. *Jurnal Cyber Tech* 3(7): 1243-1251 (2020).
11. J.W. Hutagalung. Design and Construction of an IOT-Based Oxygen Cylinder Volume Monitoring Tool Using Telegram Chat. Undergraduate Thesis. *Universitas Sumatera Utara, Medan, Indonesia* (2023).
12. Y.S. Yoon, H. Zo, M. Choi, D. Lee, and H-w Lee. Exploring the dynamic knowledge structure of studies on the Internet of things: Keyword analysis. *ETRI Journal* 40(15): 745-758 (2018).
13. J. Dogani, M. Farahmand, and H. Daryanavard. A new method to detect attacks on the Internet of Things (IoT) using adaptive learning based on cellular learning automata. *ETRI Journal* 44(1): 155-167 (2021).
14. S. Surdianto. Outseal PLC Based Drinking Water Production Quality Control System. Bachelor Thesis. *Muhammadiyah University of Ponorogo, Ponorogo, Indonesia* (2023).
15. H. Setyawan, S. Sukardi, R. Risfendra, H. Effendi,

and S. Syahril. The Effectiveness of Outseal Programmable Logic Controllerbased Training Kit to Improve Vocational High School Students' Control System Skills. *Mimbar Ilmu Journal* 29(2): 218-227 (2024).

16. Y-J. Kim, S. Song, and D. Kim. HDF: Hybrid Debugging Framework for Distributed Network Environments. *ETRI Journal* 39(2): 222-233 (2017).
17. A. Supriyono. Implementation of Programmable Logic Control (PLC) Outseal on Android-Based Automatic Bottle Filling. Bachelor Thesis. *Semarang University, Semarang, Indonesia* (2021).
18. F.R.A. Bukit, K.A. Syahputra, and S. Suherman. Design of HMI (Human Machine Interface) as a Controller and Early Detection of Capacitor Bank Damage Based on PLC. *Journal of Energy and Electrical Engineering* 3(2): 101-109 (2022).
19. A.M. Prasetia, T. Hariyanto, A. Huda, L. Sartika, and F. Fitriani. Universal Motor Speed Monitoring and Control Using Human Machine Interface (HMI). *Elektrika Borneo* 9(1): 28-35 (2023).
20. J. Zamani, M.A. Samimi, F. Sardarzadeh, and M.H. Ghezelayagh. An Optical Measurement System to Measure Velocity and Provide Shock Wave Pressure Diagrams. *International Journal of Engineering, Transactions C: Aspects* 33(3): 505-512 (2020).
21. M. Miasih. Development of oxygen volume monitoring as a basis for determining tariffs with real time based on IoT. Bachelor Thesis. *Politeknik Kesehatan Kemenkes Surabaya, Surabaya, Indonesia* (2020).
22. M. Aghanezhad, R. Shafaghat, R. Alamian, S.M.A. Seyedi, and M.J.R. Asadabadi. Experimental Study on Performance Assessment of Hydraulic Power Take-off System in Centipede Wave Energy Converter Considering Caspian Sea Wave Characteristics. *International Journal of Engineering, Transactions B: Applications* 35(5): 883-899 (2022).
23. F. Firdaus, Z. Zulfadilla, and F. Caniago. Research Methodology: Types in the New Perspective. *MANAZHIM: Jurnal Manajemen dan Ilmu Pendidikan* 3(1): 1-16 (2021).
24. A.R. Yusuf and F.N. Muzakki. Introduction to Marketplace until Line Follower Robot: Thematic KKN Innovation in Gunungsari Hamlet, Mlarak Village, Ponorogo Regency. *Diteksi: Jurnal Pengabdian Kepada Masyarakat* 2(1): 35-42 (2024).
25. M.S. Abdillah. The work system of the HPDC (High Pressure Die Casting) machine. *ITEKS (Intuisi, Teknologi dan Seni)* 16: 9-13 (2024).
26. M.S. Abdillah, G.A. Buntoro, and R.I. Vidyastari. Smart Wheelchair Design from Lecture Chair. *Jurnal Informatika dan Teknik Elektro Terapan* 12(3S1): 3479-3486 (2024).
27. M.S. Abdillah, G.A. Buntoro, and R.I. Vidyastari. Designing a Smart Wheelchair from a Lecture Chair. *Journal Teknik Elektro dan Komputasi (ELKOM)* 6(2): 216-224 (2024).
28. V.V. Martynyuk, M.P. Voynarenko, J.M. Boiko, and O. Svistunov. Simulation of Photovoltaic System as a Tool of a State's Energy Security. *International Journal of Engineering, Transactions B: Applications* 34(2): 487-492 (2021).
29. J. Singh and P. Patel. Methods for Medical Device Design, Regulatory Compliance and Risk Management. *Journal of Engineering Research and Reports* 26(7): 373-389 (2024).
30. M.S. Abdillah. Design and Build of a Smart Wheelchair From a Lecture Chair. Bachelor Thesis. *Muhammadiyah University of Ponorogo, Ponorogo, Indonesia* (2024).
31. M.S. Abdillah. Design and Build of Automatic Hand Sanitizer Based on Microcontroller. *Indonesian Journal of Applied Informatics* 8(2): 142-150 (2024).
32. M. Munirah, R.I. Vidyastari, and A. Triyanto. Introducing Robot Education to Develop Creativity and Imagination of Early Childhood at Aisyah Kauman Kindergarten, Ponorogo District. *E-Dimas* 14(3): 477-481 (2023).
33. S.S. Sasmowiyono, A. Fadlil, and A.C. Subrata. Optimum solar energy harvesting system using artificial intelligence. *ETRI Journal* 45(6): 996-1006 (2023).

Proceedings of the Pakistan Academy of Sciences: A Physical and Computational Sciences 62(2): 107-121 (2025)

ISSN (Print): 2518-4245; ISSN (Online): 2518-4253
http://doi.org/10.53560/PPASA(62-2)687

Pakistan Academy of Sciences

Research Article

Lithofacies and Grain-size Analysis of the Oligocene Nari Formation, Benir Anticline, Southern Indus Basin, Pakistan: Evidence of a Marine-to-Continental Depositional Shift

Asghar A.A.D. Hakro[1], Aijaz Ali Halepoto[1*], Surriya Bibi Ahmedani[1,2], Abdul Samad Bhutto[3], and Abdul Shakoor Mastoi[1]

[1]Centre for Pure and Applied Geology, Faculty of Natural Sciences,
University of Sindh, Jamshoro, Pakistan
[2]Government Zubeda Girls College, Hyderabad, College Education Department,
Government of Sindh, Pakistan
[3]Pakistan Petroleum Limited, PIDC House, Dr. Ziauddin Ahmed Road,
Civil Lines, Karachi, Sindh, Pakistan

Abstract: In the Southern Indus Basin, Pakistan, the Nari Formation of Oligocene age represents an important stratigraphic unit that preserves a classical regressive depositional sequence, recording a significant transition from marine to continental environments. This study analyzes the lithofacies and grain-size parameters of the Nari Formation from the Benir anticline section, Southern Indus Basin, to interpret its depositional environments. A 65 m thick stratigraphic section was measured and divided into non-clastic and clastic lithofacies groups. Non-clastic lithofacies group observed in the lower part of the Nari Formation and consists of compacted limestone, coquinoidal limestone and arenaceous limestone lithofacies, indicating deeper outer-ramp to near-shore depositional environments. The clastic lithofacies group was identified in the upper part, which consists of calcareous sandstone, variegated and gypsiferous shale, lateritic sandstone and friable sandstone lithofacies, suggesting continental fluvial depositional conditions. Shale-bearing lithofacies were identified in the middle part of the Nari Formation, reflect evaporitic and oxidizing continental settings. Grain-size analysis of eleven samples from friable sandstone facies supports a river-dominated origin. The vertical transition from marine to continental facies in the Nari Formation reflects a significant depositional shift, documenting a regressive sequence from marine ramp to fluvial settings. This study contributes to the broader understanding of the stratigraphic evolution of the Southern Indus Basin in relation to Oligocene regional tectonic background.

Keywords: Lithofacies, Grain-size Analysis, Depositional Environment, Oligocene, Nari Formation.

1. INTRODUCTION

The analysis of lithofacies has long been an essential tool in deciphering sedimentary processes and depositional environments [1-4]. By examining sedimentary structures, texture, mineral composition and fossils content, lithofacies analysis enables the interpretation of various depositional systems such as fluvial, deltaic and shallow marine environments [4-6]. Lithofacies analysis is generally supplemented with grain-size analysis, petrography, geochemistry and advanced technologies, such as scanning electron microscope (SEM), X-ray diffraction (XRD) and X-Ray Computed Tomography [2, 6-9]. Among these, the grain-size analysis is widely used to determine sediment transport mechanisms, energy conditions and depositional settings [6, 10-12]. The Oligocene is a crucial epoch in the geological history of the Indus Basin, marked by significant tectonic and

---

Received: March 2025; Revised: May 2025; Accepted: June 2025
* Corresponding Author: Aijaz Ali Halepoto <aijaz.halepoto@usindh.edu.pk>

depositional changes [12-14]. These changes were driven by progressive continent-continent collision of the Indian and Eurasian Plates [13-17]. The Nari Formation is a key stratigraphic unit that preserved exceptional record of these tectonic and depositional changes. Therefore, understanding its lithofacies characters and depositional environment is vital for reconstructing the Oligocene geological history of the region. The Benir anticline, a doubly plunging, north-south trending structure located in the southeastern Kirthar Fold Belt, offers well-preserved exposures of the Nari Formation. Previously, Nari Formation was studied in terms of provenance [18, 19], depositional environment [10, 12, 20, 21] and diagenesis [22-24]. During previous studies, textural, mineralogical and geochemical attributes of the Nari Formation have been explored from different exposed sections in the Southern Indus Basin. However, a systematic lithofacies record capturing the full spectrum of depositional environments and their stratigraphic transitions within the Nari Formation is not yet clearly understood. The present study aims to bridge this research gap by conducting its comprehensive lithofacies and grain-size analysis from the Benir anticline section, Southern Indus Basin. The results of this study will not only enhance our understanding of the sequential changes in the depositional environment during the Oligocene in the study area, but also contribute to understanding the depositional environment shift from marine to continental settings in response to plate collision along the western margin of the Indus Basin, Pakistan.

2. GEOLOGICAL BACKGROUND

The Indus Basin is situated in the northwestern part of the Indian Plate [17, 25]. It is bordered by the Indian Shield in the east, the Himalayas in the north, the Suleiman and Kirthar ranges in the west and the Arabian Sea in the south [26-31]. The western part of the Indus Basin became the foreland basin in response to continent-continent collision between the Indian and Eurasian Plates during the Cenozoic [12, 16, 17, 29]. The Indus Basin is divided into upper and lower parts by the Precambrian Shield elements, exposed in the Sargodha High [25, 26]. The Lower Indus Basin is further divided into central and southern parts by the "Sukkur Rift Zone" [26, 30]. The Southern Indus Basin comprises four most dominant tectonic units, which are the Precambrian Indian Shield ("Nagarparkar Igneous Complex (NIC)", the Indus Platform, the Kirthar Foredeep and the Kirthar Fold Belt [17, 27, 31, 32]. The NIC is composed of an-orogenic (A-type), igneous (I-type) granite, low-grade metamorphic rocks, acidic and basic dikes and rhyolite plugs [33, 34]. The NIC is part of the basement of the Southern Indus Basin, which is overlain by Mesozoic and Cenozoic rocks [17, 25, 26].

The Indus Platform is a gently west-dipping platform that consists of Mesozoic sedimentary rocks cut by Late Cretaceous normal faults [17, 26, 35]. The Mesozoic rocks of the Indus Platform are unconformably overlain by generally undeformed Tertiary rocks [25, 36, 37]. The Kirthar Foredeep is a down-warped segment of the Southern Indus Basin due to lithospheric flexure in front of the growing Kirthar and Suleiman ranges [17, 26, 38]. It consists of thick post-Eocene sedimentary rocks, particularly the Neogene Molasses of the Manchar Formation. The western part of the Southern Indus Basin is structurally deformed due to its oblique collision with the Afghan Block along the Ornach-Nal Fault [39-41]. This deformed part is called the "Kirthar Fold Belt" [17, 26, 31]. The western part of the Kirthar Fold Belt consists of exposed Bela Ophiolites and Mesozoic sedimentary rocks, whereas Cenozoic rocks are predominantly exposed in its eastern part [28, 42, 43] (Table 1). The present study area is located in the southeastern part of the Kirthar Fold Belt (Figure 1).

3. MATERIALS AND METHODOLOGY

Detailed geological fieldwork of the Nari Formation was carried-out from the Benir anticline (Latitude 25°27'18.50" N, Longitude 67°36'51.12" E). The lower contact of the Nari Formation is not exposed in the study area; therefore, measurement was started from core of the Benir anticline (Figure 2(a)). Individual lithofacies were identified and their thickness in the stratigraphic section were measured with help of measuring tape. The total measured thickness of the Nari Formation in study area is 65 m (Figure 2(b)). All lithofacies were described based on their outcrop and lithological attributes, such as lithology, texture, fossils and sedimentary structure. During the measurement of the stratigraphic section, thirty-five lithological strata were identified and sampled, which included 16 limestone, 11 sandstone, 4 shale and 4 lateritic or oxidized sandstone. These strata were broadly classified into two lithofacies groups, i.e., non-clastic and clastic lithofacies groups. The non-clastic lithofacies group is further divided into three distinct lithofacies based on their lithology and relative abundance of fossils contents. The clastic lithofacies group is further classified into four lithofacies based on their lithological aspects. From the thirty-five samples, 11 loose and friable sandstone were selected for grain-size analysis (Figure 2(b)). Most of the loose and friable sandstone

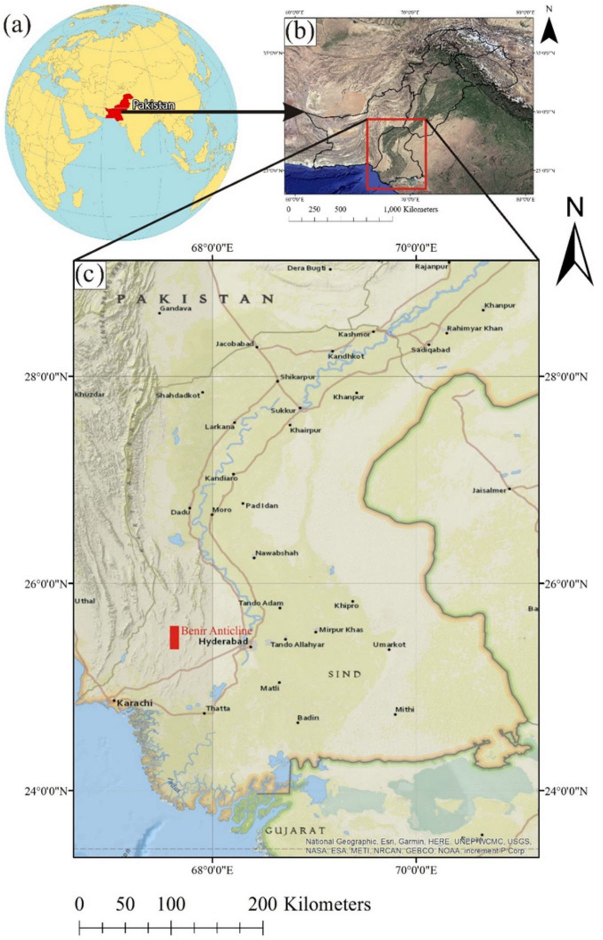

Fig. 1: Location map of the Benir anticline (Image Source-National Geo-graphic, Esri, Garmin, HERE, UNEPWCMC, USGS, NASA, ESA, METI, NRCAN, GEBCO, NOAA, increment P Corp. & gisgeography. com).

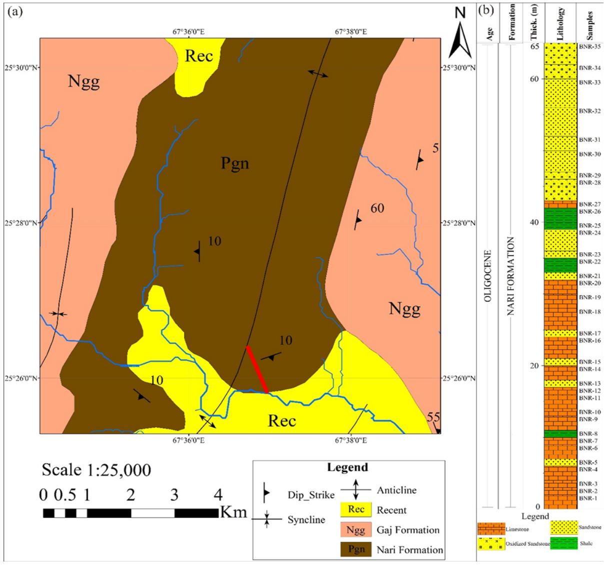

Fig. 2: (a) Geological map of the Benir anticline, showing the location of the measured section marked with a bold red line (after [17, 42]). (b) Lithological column of the measured section indicating formation thickness and sample numbers.

Table 1. Exposed stratigraphy of the Southern Indus Basin (after [28, 42]).

Age	Formation	Lithology
Pleistocene	Dada Conglomerate	Conglomerate, Boulders and Pebbles
Neogene	Manchar Formation	Sandstone, Shale and Conglomerate
Miocene	Gaj Formation	Sandstone, Shale, Limestone
Oligocene	Nari Formation	Limestone, Shale and Sandstone
Eocene	Kirthar Formation	Limestone
	Tiyon formation	Limestone, Shale, Marl
	Laki Formation	Limestone, Shale, and Sandstone
Paleocene	Lakhra Formation	Limestone, Shale and Sandstone
	Bara Formation	Sandstone, Claystone and Shale
	Khadro Formation	Sandstone, Shale and Limestone
	Khaskheli Basalt	Basalt
Cretaceous	Pab Sandstone	Sandstone
	Fort Munro Formation	Limestone and Marl

is observed in the upper part of the measured section, which lacked depositional features, such as bed geometry, sedimentary structures, or fossils contents. Therefore, their samples were analyzed in terms of their grain-size distribution. The standard sieving method was adopted to process, classify and analyze different groups of grain-sizes in the studied samples [10, 44-46]. The grain-sizes in millimeters, obtained through sieve analysis were converted to “phi (φ)” scale, which is a logarithmic scale to base 2 [6, 47]. Cumulative frequency curves for each analyzed sample were drawn from the weight percentage of each grain size in the sample. Different grain-size parameters, such as mean, median, standard deviation, skewness, kurtosis etc., of each sample were calculated from cumulative frequency curves. Different bivariate interpretation diagrams were prepared by plotting grain-size parameters against each other to understand the textural character, transportation mechanism and depositional environment of the loose and friable sandstone of the Nari Formation [6, 12, 45].

4. RESULTS

4.1. Lithofacies Analysis

The lower contact of the Nari Formation is not exposed in the Benir anticline section, whereas it has either a sharp upper contact with the Miocene Gaj Formation, or its upper contact is covered with the Holocene deposits. The Nari Formation exhibits diverse and distinct patterns of lithologies from base to top, which are broadly classified into non-clastic and clastic lithofacies groups (Figure 2).

4.1.1. Non-clastic Lithofacies Group

The lithofacies of this group were identified in the lower part of the Nari Formation in the study area. These lithofacies are dominantly composed of limestone and are further classified into three lithofacies types based on lithological features and the relative abundance of fossils contents.

(a) Compacted Limestone Facies

These lithofacies were identified in the lower part and consists of eight strata (BNR-1, 3, 6, 10, 11, 12, 14 and 27) with a cumulative thickness of 12 m. These are characterized by orange-yellow to creamy yellow, well compacted and jointed limestone, fossiliferous, but it contains rare larger benthic foraminifera (Figure 3(a)). These lithofacies are dominantly composed of fine-grained calcareous and bioclastic material along with mega-fossils of gastropods, echinoids and bivalves. These contains fibrous sparry calcite, which forms flower-shaped structures within limestone (Figures 3(b), 5(b)). The texture of these lithofacies resembles with the mudstone-wackstone, because they consist of higher fine-grained calcareous content than larger bioclasts. The dominancy of fine-grained calcareous material indicate deposition under low-energy marine environment, below storm weather wave-base [48, 49]. The gastropods, echinoids and bivalves are generally tend to live in shallow coastal areas to deep marine environments, around the world [50-52]. Therefore, these lithofacies of the Nari Formation are interpreted to be deposited in the open-marine, distal part of the outer-ramp, under low-energy depositional environment.

(b) Coquinoidal Limestone Facies

These lithofacies were also identified in the lower part of the Nari Formation in the studied section. These consists of four strata (BNR-2, 4, 7 and 9) with a cumulative thickness of 6 m. They are characterized by orange-yellow well compacted and in places, moderately compacted limestone. These lithofacies are dominantly composed of tests of larger benthic foraminifera, particularly *Discocyclina* and *Nummulites,* and broken shelly fragments. The abundance of foraminiferal tests gives the limestone a distinctive biogenic character. The bioclasts are generally poor to moderately sorted and aligned horizontally to the bedding planes (Figure 3(c-e)). The texture of thess lithofacies resembles with the wackstone packstone, because it consists of lower mud matrix content than bioclasts. *Discocyclina* is reported to occur in the outer-ramp, low-energy and under lower photic zone depositional settings [53-56] The abundance of *Discocyclina* with *Nummulites* has been reported from the middle to outer ramp of the Eocene carbonates [57-59]. Therefore, Coquinoidal limestone lithofacies of the Nari Formation are interpreted to have been deposited in the middle to outer ramp depositional environment. Alternation of coquinoidal and compacted limestone facies suggest middle to distal part of outer-ramp depositional environment during deposition of lower part of the Nari Formation in study area.

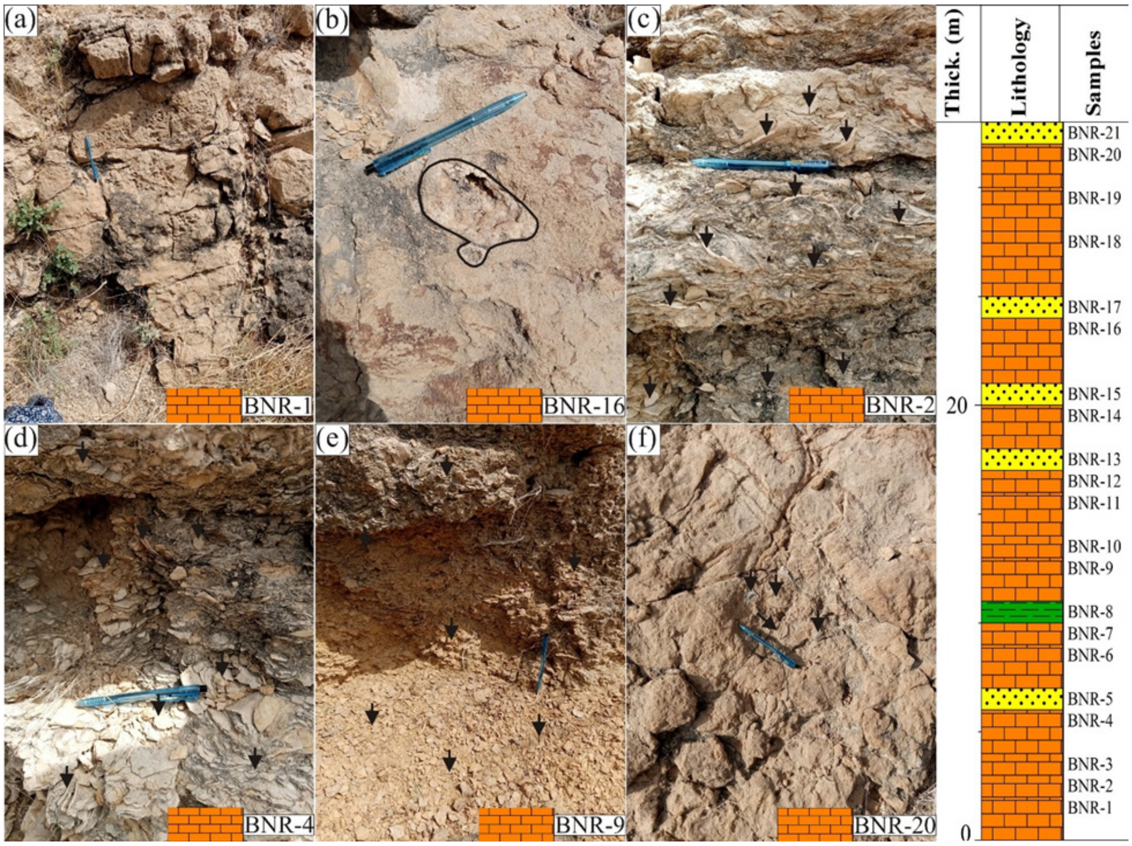

Fig. 3: Non-clastic lithofacies of the Nari Formation in the studied section and their respective positions in the lithological column. (a, b) Compacted limestone facies. The black polygon in (b) outlines sparry calcite. (c, d) Coquinoidal limestone facies dominantly composed of bioclasts of *Discocyclina*. (e) Coquinoidal limestone facies dominantly composed of *Discocyclina* and *Nummulites* tests. (f) Arenaceous limestone facies.

(c) Arenaceous Limestone Facies

These lithofacies were identified in the middle part of the Nari Formation in the study area. These consists of four strata (BNR-16 and 18-20) with a cumulative thickness of 10 m. These are reddish-gray, well-compacted limestone facies, which consist of a significant proportion of sand. These lithofacies contain worm-burrows, fossils of plecypods and bivalves (Figure 3(f)). The presence of a significant proportion of medium-grained sand in these lithofacies suggest enhanced sediment supply from the continent [58, 60]. The presence of worm-burrows associated with plecypods and bivalves is an indication of a coastal environment [51, 61]. Therefore, arenaceous limestone facies of the Nari Formation were deposited in the near-shore depositional environment. As these lithofacies overlie the middle to outer-ramp deposited-facies, hence indicate progressively decreasing sea-levels during the deposition of the Nari Formation in the study area.

4.1.2. Clastic Lithofacies Group

The lithofacies of this group were identified in the middle to upper part of the Nari Formation in the study area (Figure 4(a)). These lithofacies are dominantly composed of sandstone and shale. Lithofacies of this group are further classified into four lithofacies types based on differences in lithological features.

(a) Calcareous Sandstone Facies

These lithofacies were identified in the middle part of the Nari Formation and it overlies the arenaceous limestone facies. These consists of six strata (BNR-13, 15, 17, 21, 23 and 24) with a cumulative thickness of 8 m. These are light-yellow to grayish-yellow, moderately compacted to friable sandstone facies, which consist of calcareous material, possibly as cementing material. No primary sedimentary structures and fossils were identified in these strata (Figures 4(b, d, e)). The depositional environment of these lithofacies could not be precisely determined due to lack of primary sedimentary structures and fossil contents. Therefore, friable samples of these lithofacies were studied through grain-size analysis.

(b) Variegated and Gypsiferous Shale Facies

Four strata of shale were identified, one in the basal (BNR-8) and three in the middle part (BNR-22, 25 and 26) of the Nari Formation in the studied section. These lithofacies have a cumulative thickness of 6 m, and exhibit diverse color ranges (Figures 4(c, f)). BNR-22 and 25 are variegated and contain abundant gypsum veins (Figure 4(f)). BNR-26 is oxidized, dark red to reddish-brown and it does not contain any evaporitic mineral (Figure 5(a)). Shale deposits in low-energy depositional settings of floodplain, lake, lagoon or deep-marine environments, where fine sediments settle out of slow-moving or quite water [62-64]. Gypsum often forms in arid or semi-arid regions due to evaporation of sea-water [65, 66]. The oxidized nature of shale also suggests the continental oxidizing environment. This evidence suggests, these lithofacies of the Nari Formation were deposited in a continental shallow-water evaporative lagoon.

(c) Lateritic Sandstone Facies

These lithofacies were identified in the upper part of the Nari Formation in the studied section. These consists of four strata (BNR-28, 29, 34, and 35) with a cumulative thickness of 9 m. These are pinkish-brown, light pink and brownish-red, moderately compacted to friable, highly oxidized and jointed sandstone (Figures 5(c, d)). No primary sedimentary structures were identified in these strata, but their lithological character suggests oxidizing continental deposition or prolonged exposure of sediment surface to oxygen-rich environmental conditions. Its stratum BNR-28

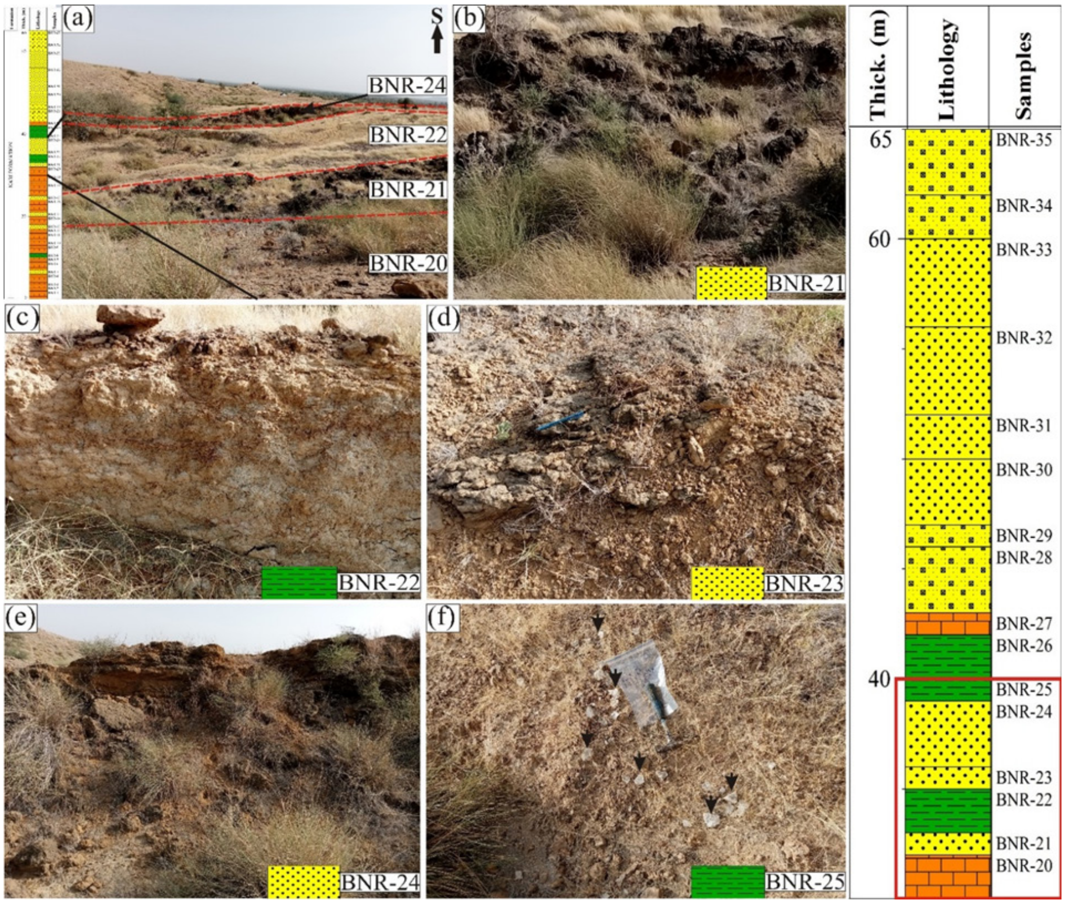

Fig. 4: Clastic lithofacies of the Nari Formation in the studied section and their respective positions in the lithological column shown within red rectangle. Field photograph (a) showing lithofacies stacking pattern. (b) Calcareous sandstone facies. (c) Gypsiferous shale facies. (d, e) Calcareous sandstone facies. (f) Variegated and gypsiferous shale facies.

overlies the compacted limestone facies stratum 27, indicating sharp transition from deeper distal outer-ramp environment to continental environmental conditions. Grain-size analysis of friable samples of these lithofacies has been carried out to support the lithofacies interpretation.

(d) Friable Sandstone Facies

These were identified in the upper part of the Nari Formation and consists of four strata (BNR-30-33) with a cumulative thickness of 13 m. These are light gray to reddish-gray, friable to loose and massive sandstone (Figures 5(e, f)). No primary sedimentary structures were identified in these facies; hence, their depositional environment could not be determined. Therefore, friable samples of these lithofacies were studied through grain-size analysis to understand their depositional environment.

4.2. Grain-size Analysis

Grain-size analysis of loose and friable sandstone involves the systematic measurement and statistical characterization of grain diameters to determine their textural properties. The grain-size distribution provides critical insights into depositional environment and transport mechanisms [6, 12]. Well-sorted sandstones with narrow grain-size distributions typically indicate uniform depositional conditions, such as Aeolian or mature beach systems, while poorly sorted samples suggest rapid deposition or limited transport distances. The presence of bimodal or polymodal distributions may indicate mixing of different sediment sources or multiple depositional episodes [12, 45]. Statistical parameters calculated from grain-size analysis of the Nari Formation during the present study are presented in Table 2.

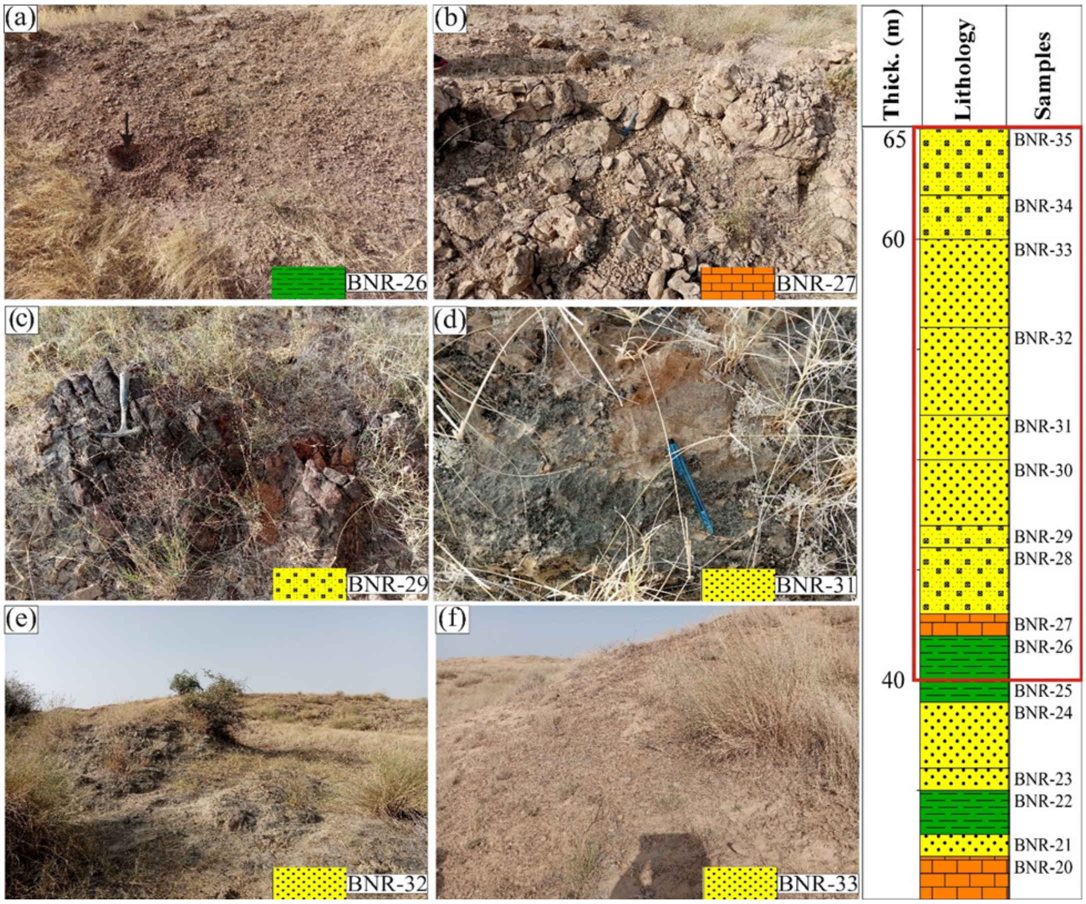

Fig. 5: Clastic lithofacies of the Nari Formation in the studied section and their respective positions in the lithological column shown within red rectangle. (a) Variegated and oxidized shale facies. (b) Compacted limestone facies. (c, d) Lateritic sandstone facies. (e, f) Friable sandstone facies.

Table 2. Grain-size parameters (“phi (φ)” unit) of the Nari Formation from Benir anticline.

S. No.	Sample	Mean	Median	Standard Deviation	Skewness	Kurtosis	C	M
1	BNR. 5	2.06	2.2	1.74	-0.21	1.33	846.75	217.64
2	BNR. 8	0.56	1	1.03	0.08	1.29	716.98	500.00
3	BNR.13	1.96	1.9	1.75	-0.13	0.53	812.25	267.94
4	BNR. 17	0.96	1.8	1.18	-0.15	1.49	687.77	287.17
5	BNR. 25	0.86	0.9	1.28	-0.05	0.65	737.13	535.89
6	BNR. 26	0.23	1.5	1.26	0.01	0.83	747.42	353.55
7	BNR. 28	1.93	1.8	1.68	-0.01	1.54	870.55	287.17
8	BNR. 30	1.7	1.6	1.32	0.08	1.36	933.03	329.88
9	BNR. 31	1.43	1.4	1.15	0.04	1.7	870.55	378.93
10	BNR. 33	1.7	1.6	1.3	1.23	1.48	972.65	329.88
11	BNR. 34	1.9	1.8	1.81	-0.08	2.28	768.44	287.17

4.2.1. Mean

The mean grain size values suggest the relative size of clasts, where a 0 value of phi (φ) indicates coarse sand and 3 indicates very fine sand. The studied samples show mean grain size in the range of 0.23-2.06 φ (coarse to fine), with an overall average of 1.39 φ (Table 2) (Figures 6(a-c)). The average mean size of the studied samples indicates the medium-grained sand. Mean grain size reflects the average energy conditions during deposition, with finer grains indicating lower energy environments. The variations in the mean grain-size value indicate fluctuations in the depositional energy level [6, 11, 63].

4.2.2. Median

It is the central grain size of a studied sample, for which half of the grains in that sample are larger than it, and half are smaller. The median grain-size value gives a good approximation of grain-size of studied strata. The studied samples show median size value in the range of 0.9-2.2 φ, with an average median size of 1.6 φ. This average median value indicates presence of medium-grained sand in the studied samples [6, 12, 45].

4.2.3. Standard Deviation (Sorting)

This statistical parameter determines level of sorting of the sediments [63]. The standard deviation value of 0 is taken as very well sorted sediments and any positive integer more than 2 is considered as very poorly sorted [63]. Sorting in turn is used to understand the hydrodynamic conditions or degree of reworking in the depositional system. Sorting is determined by transport processes, deposition and post-depositional processes such as winnowing or reworking [62, 63]. The standard deviation values of the Nari Formation in the Benir anticline section range between 1.03 to 1.81 φ, having an average of 1.40 φ. The standard deviation range of studied sediments indicate poor sorting (Figure 6(b)). This suggests that analyzed sediments were deposited in low-energy conditions and, therefore, didn’t experience significant reworking during their deposition.

4.2.4. Skewness

The skewness is another statistical grain-size parameter of sorting, which indicate symmetry of grain size distribution in the studied samples. Measured skewness values of the studied samples of the Nari Formation ranges from -0.21 to 1.23 φ, having average of 0.07 φ. The skewness range of the studied sediments shows coarse-skewed to near symmetrical, while average skewness represents near symmetrical nature of sandstone of the Nari Formation (Figures 6(a, d)). The coarse-skewed to symmetrical nature of the sediments suggest the presence of poorly-sorted clasts, which were deposited in medium to low-energy conditions [12, 67-70].

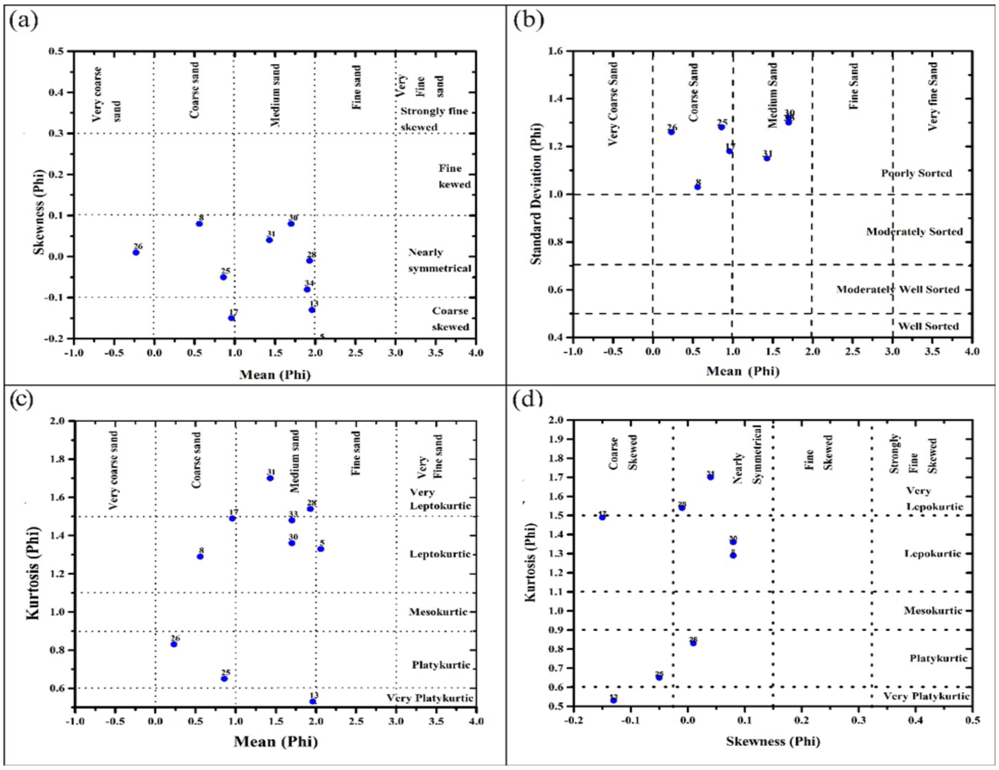

Fig. 6: Plots of grain-size parameters of the Nari Formation. (a) Mean versus skewness. (b) Mean versus standard deviation. (c) Mean versus kurtosis. (d) Skewness versus kurtosis.

4.2.5. Kurtosis

The kurtosis range of the Nari Formation in the studied section ranges from 0.53 to 1.50 φ with an average of 2.28 φ. Most samples of the Nari Formation show leptokurtic to very leptokurtic nature, while some samples indicate very platykurtic and platykurtic (Figures 6(c, d)). The kurtosis pattern indicates medium to low-energy depositional conditions during the deposition of the Nari Formation in the study area [12, 45].

4.2.6. Bivariate Statistical Diagrams

The bivariate statistical diagrams of grain-size distribution in the sedimentary rocks are valuable to diagnose the energy of the depositional medium as well as their depositional environment [44, 45, 67-70]. The median diameter plotted against standard deviation and mean diameter against skewness of analyzed sediments to distinguish between fluvial (river), shallow-marine (wave-dominated) and deep water (quiet water) deposition [12, 45, 67]. All analyzed samples of the Nari Formation from the Benir anticline fall in the "River" field of the "median versus standard deviation" diagram (Figure 7(a)). All analyzed samples also occupy the "River" field in the "mean versus skewness" diagram (Figure 7(b)). Therefore, these diagrams suggest that analyzed sediments of the Nari Formation were deposited in a fluvial (river-dominated) depositional environment.

4.2.7. Passega Diagram (CM Plot)

The CM plot (Passega diagram) was proposed by Passega [68] to identify sediment transport and depositional processes. These diagrams illustrate the correlation between 1% or one percentile (C) on the frequency curve of each sample and the median grain-size (M). Both these variables are first converted from φ (phi) in to µm and then M is plotted on the x-axis and C is plotted on the y-axis (Table 2). All the analyzed samples fall on 2 field between 1 and 3 fields on the CM plot diagram for transporting mechanism (Figure 7(c)). This indicates that analyzed sediments of the Nari Formation were transported through a rolling and suspension mechanism. All the studied samples fall between 4 and 5 fields on the CM plot diagram for depositional mechanism (Figure 7(d)), indicating deposition in fluvial conditions [6, 12, 45].

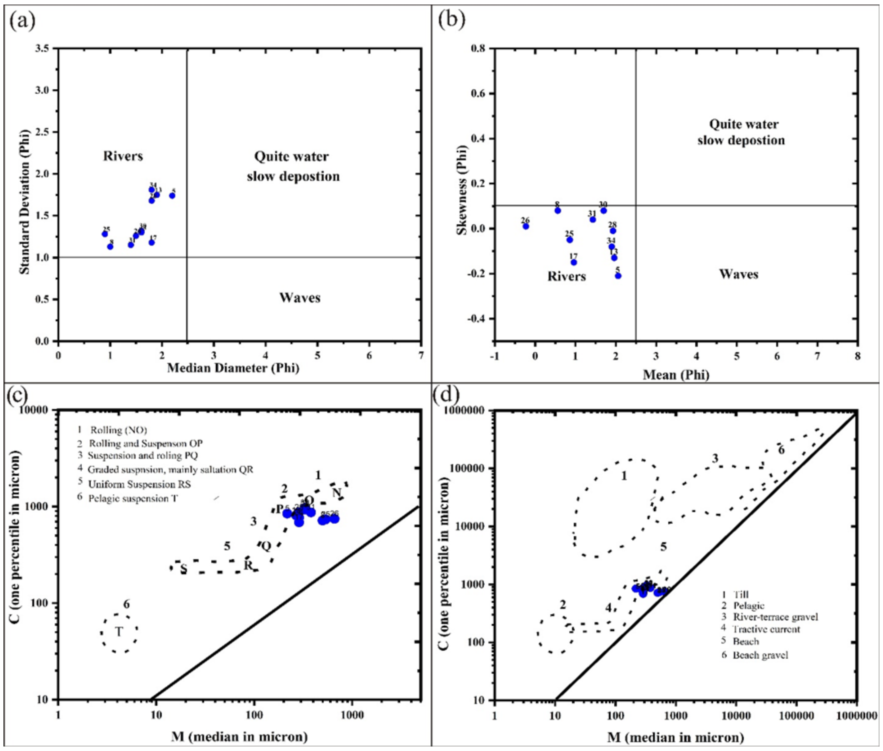

Fig. 7: (a) Median diameter versus standard deviation. (b) Mean diameter versus skewness. (c) Transportation mechanism. (d) Depositional mechanism of analyzed sediments of the Nari Formation, Benir anticline, Southern Indus Basin, Pakistan.

5. DISCUSSION

The lithofacies and grain-size analysis of the Nari Formation in the Benir anticline revealed a fascinating record of marine to continental depositional shift during the Oligocene in the Southern Indus Basin. The systematic vertical succession of lithofacies, which could be correlated with other prominent sections of the Nari Formation [21], demonstrates a clear regressive sequence that documents the progressive retreat of marine conditions and the establishment of continental depositional systems.

5.1. Marine Depositional Phase: Outer Ramp to Near Shore Settings

The lower part of the Nari Formation preserves evidence of initial marine deposition under outer-ramp settings. The compacted limestone facies, characterized by fine-grained calcareous material and mudstone-wackstone textures, indicate deposition in the distal outer-ramp environment below storm wave-base [48, 49]. This interpretation is also supported by the presence of marine fossils including gastropods, echinoids and bivalves, which collectively suggest low-energy, open-marine conditions [50-52]. The coquinoidal limestone facies, dominated by larger benthic foraminifera (*Discocyclina* and *Nummulites),* represents deposition in the middle to outer-ramp environment [53-56]. The abundance of these foraminifera, particularly *Discocyclina,* which thrives in outer-ramp, low-energy settings within the lower photic zone, confirms the marine origin of these sedimentary deposits [57-59]. The alternation between compacted limestone and coquinoidal limestone facies in the lower part provides crucial insights into the depositional dynamics of the marine ramp carbonate system and indicates frequent environmental changes from distal outer-ramp to middle to outer-ramp and vice versa. The transition to arenaceous limestone facies in the middle part of the Nari Formation marks a critical shift in the depositional system. The influx of significant proportions of sand, along with the presence of worm-burrows and shallow-marine fauna (plecypods and bivalves), indicates enhanced terrigenous input and shoaling conditions [21, 58, 60]. These facies represent deposition in the near-shore environment and provide the first clear evidence of marine regression and increasing continental influence. The marine depositional phase of the Nari Formation in the Benir anticline section resembles that of the Hundi anticline section of the Nari Formation [21].

5.2. Continental Depositional Phase: Fluvial and Evaporitic Settings

The upper part of the Nari Formation documents a dramatic shift to continental depositional conditions, as evidenced by the clastic lithofacies group. The calcareous sandstone facies, lacking primary sedimentary structures and fossils, required grain-size analysis for environmental interpretation. The grain-size parameters consistently pointed to fluvial deposition, with bivariate diagrams placing all analyzed samples within the "River" field, confirming a fluvial depositional environment. The variegated and gypsiferous shale facies suggest deposition in evaporitic continental settings. The presence of abundant gypsum veins indicate arid to semi-arid climatic conditions with high evaporation rates, typical of continental evaporative lagoons or playa lake environments [62-64]. The oxidized nature of these shales, particularly the dark red to reddish-brown coloration, further supports continental oxidizing conditions and suggests periodic exposure to atmospheric oxygen [65, 66]. The lateritic sandstone facies represent the culmination of continental conditions, with its highly oxidized, pinkish-brown to brownish-red coloration indicating prolonged exposure to oxygen-rich environments. The sharp bedding plane between these facies and the underlying compacted limestone facies (stratum BNR-28 overlying stratum 27) dramatically illustrates the abrupt transition from middle to outer-ramp conditions to the continental environments, suggesting rapid regression or tectonic uplift. The continental depositional phase of the Nari Formation in the Benir anticline section is different than the Hundi anticline section of the Nari Formation [21]. It indicates that the continental depositional environments are highly unstable and their characteristics vary from place to place.

5.3. Energy Conditions and Transport Mechanisms

The grain-size analysis provides quantitative support for the environmental interpretations derived from lithofacies analysis. The mean grain-size values (0.23-2.06 φ) indicate predominantly medium-grained sand, suggesting moderate energy conditions during deposition. The poor sorting (standard deviation 1.03 to 1.81 φ) indicates limited reworking and transport, consistent with rapid deposition in relatively low-energy fluvial systems [6, 12, 45]. The skewness values (-0.21 to 1.23 φ) range from coarse-skewed to near-symmetrical, with an average near-symmetrical distribution. This pattern, combined with the kurtosis values showing leptokurtic to very leptokurtic distributions, confirms medium to low-energy depositional conditions [12, 67-70]. The Passega diagram analysis reveals that sediments were transported through rolling and suspension mechanisms and deposited under fluvial conditions, providing definitive evidence for the continental nature of the upper Nari Formation.

5.4. Regional Sequence Stratigraphic Significance

The marine to continental depositional transition documented in the Nari Formation reflects broader regional changes in the Southern Indus Basin during the Oligocene. This regression likely resulted from a combination of eustatic sea-level changes, regional tectonic uplift and increased sediment supply from the growing Himalayan orogen. The timing of this transition is consistent with the global Oligocene regression and the intensification of Himalayan uplift [4, 13, 17, 21]. The vertical succession of lithofacies in the Nari Formation represents a classic regressive sequence, documenting the progressive shoaling and eventual emergence of the depositional system [21]. The sharp bedding planes between marine limestone and continental sandstone facies suggest a rapid regression, possibly related to tectonic uplift or a significant drop in relative sea-level. This sequence provides valuable insights into the timing and mechanisms of basin evolution in the Southern Indus Basin and contributes to our understanding of the regional response to Himalayan orogeny.

6. CONCLUSIONS

The lithofacies and grain-size analysis of the Oligocene Nari Formation in the Benir anticline section has been carried out in order to shed light on its depositional environments and their shift from marine to continental conditions. The lower part of the Nari Formation consists of limestone-dominated lithofacies, which were deposited in a deeper outer-ramp to near-shore depositional environment. Shale-dominated lithofacies were identified in the middle part of the Nari Formation, which are interpreted to have been deposited in the evaporitic and oxidizing settings. The upper part of the Nari Formation consists of sandstone-dominated lithofacies, which indicate deposition in continental conditions. Grain-size analysis of the sandstone facies suggest that these were deposited in fluvial or river-dominated depositional environments. Overall, the Nari Formation in the study area represents a well-preserved example of a regressive depositional sequence, documenting the progressive depositional regime shift from marine to continental conditions during the Oligocene. The marine to continental depositional shift was controlled by the Himalayan orogeny in the region.

7. ACKNOWLEDGMENTS

The authors are thankful to Prof. Dr. Rafique Ahmed Lashari, Director, Centre for Pure and Applied Geology, University of Sindh, Jamshoro, Pakistan, for providing transportation and other field-related facilities as well as permission of using sedimentological laboratories at the Centre for Pure and Applied Geology. We are thankful to the Wildlife Department, Government of Sindh for providing security and guiding personnel during the fieldwork. The authors are also thankful to Mr. Owais Khokhar, Aiza Preet Hakro and Muhammad Azeem for their assistance during fieldwork. We are thankful to Mr. Riaz Ali Shah, Field Driver, Centre for Pure and Applied Geology, University of Sindh, Jamshoro and Mr. Dad Muhammad Burfat for facilitating our fieldwork.

8. CONFLICT OF INTEREST

The authors declare no conflict of interest.

9. REFERENCES

1. S. Obaid, A.W. Qureshi, and I.A. Abbasi. Lithofacies, sand-bodies geometry and depositional setting of the Datta Formation in Surghar Range, North Pakistan. *SPE-PAPG Annual Technical Conference (28th - 29th November 2005)*, *Islamabad, Pakistan* (2005).
2. A.K. Srivastava and R.S. Mankar. Lithofacies architecture and depositional environment of Late Cretaceous Lameta Formation, Central India. *Arabian Journal of Geosciences* 8(1): 207-226 (2013).
3. A. Bilal, R. Yang, N. Lenhardt, Z. Han, and X. Luan. The Paleocene Hangu formation: A key to unlocking the mysteries of Paleo-Tethys tectonism. *Marine and Petroleum Geology* 157: 106508 (2023).
4. G. Métais, P.O. Antoine, S.R.H. Baqri, J.Y. Crochet, D. De Franceschi, L. Marivaux, and J.L. Welcomme. Lithofacies, depositional environments, regional biostratigraphy and age of the Chitarwata Formation in the Bugti Hills, Balochistan, Pakistan. *Journal of Asian Earth Sciences* 34(2): 154-167 (2009).
5. C. Wang, B. Zhang, Y. Lu, Z. Shu, Y. Lu, H. Bao, Z. Meng, and L. Chen. Lithofacies distribution characteristics and its controlling factors of shale in Wufeng Formation-Member 1 of Longmaxi Formation in the Jiaoshiba area. *Petroleum Research* 3(4): 306-319 (2018).
6. A.A.A.D. Hakro, A.A. Halepoto, M.S. Samtio, R.H. Rajper, A.S. Mastoi, R.A. Lashari, and M.A. Rahoo. The Comparative Depositional Heterogeneity of Manchhar Formation (Siwalik Group), Southern Indus Basin, Pakistan. *Journal of Mountain Area Research* 9: 1-15 (2024).
7. C. Klein and N.J. Beukes. Geochemistry and sedimentology of a facies transition from limestone to iron-formation deposition in the early Proterozoic Transvaal Supergroup, South Africa. *Economic Geology* 84(7): 1733-1774 (1989).
8. P. Wang, Z. Jiang, L. Yin, L. Chen, Z. Li, C. Zhang, T. Li, and P. Huang. Lithofacies classification and its effect on pore structure of the Cambrian marine shale in the Upper Yangtze Platform, South China: Evidence from FE-SEM and gas adsorption analysis. *Journal of Petroleum Science and Engineering* 156: 307-321 (2017).
9. J.E. Houghton, J. Behnsen, R.A. Duller, T.E. Nichols, and R.H. Worden. Particle size analysis: A comparison of laboratory-based techniques and their application to geoscience. *Sedimentary Geology* 464: 106607 (2024).
10. Q. Khokhar, A.A.A.D. Hakro, S.H. Solangi, I. Siddiqui, and S.A. Abbasi. Textural Evaluation of Nari Formation, Laki Range, Southern Indus Basin, Pakistan. *Sindh University Research Journal (Science Series)* 48(3): 633-638 (2016).
11. C. Baiyegunhi, K. Liu, and O. Gwavava. Grain size statistics and depositional pattern of the Ecca Group sandstones, Karoo Supergroup in the Eastern Cape Province, South Africa. *Open Geosciences* 9(1): 554-576 (2017).
12. A.A.A.D. Hakro, W. Xiao, A.S. Mastoi, Z. Yan, M.S. Samtio, and R.H. Rajper. Grain size analysis of the Oligocene Nari Formation sandstone in the Laki

Range, southern Indus Basin, Pakistan: Implications for depositional setting. *Geological Journal* 425: 5440-5451 (2021).

13. G. Zhuang, Y. Najman, S. Guillot, M. Roddaz, P.O. Antoine, G. Métais, A. Carter, L. Marivaux, and S.H. Solangi. Constraints on the collision and the pre-collision tectonic configuration between India and Asia from detrital geochronology , thermochronology , and geochemistry studies in the lower Indus basin , Pakistan. *Earth and Planetary Science Letters* 432: 363-373 (2015).
14. M. Qasim, O. Tayyab, L. Ding, J.I. Tanoli, Z.I. Bhatti, M. Umar, H. Khan, J. Ashraf, and I.A.K. Jadoon. Exhumation of the Higher Himalaya: Insights from Detrital Zircon U–Pb Ages of the Oligocene–Miocene Chitarwatta Formation, Sulaiman Fold–Thrust Belt, Pakistan. *Applied Sciences* 13(6): 3418 (2023).
15. L. Ding, M. Qasim, I.A.K. Jadoon, M.A. Khan, Q. Xu, F. Cai, H. Wang, U. Baral, and Y. Yue. The India-Asia collision in north Pakistan: Insight from the U–Pb detrital zircon provenance of Cenozoic foreland basin. *Earth and Planetary Science Letters* 455: 49-61 (2016).
16. A.A. Halepoto, M.H. Agheem, A.A.A.D. Hakro, S. Ahmed, and S.B. Ahmedani. Geometry and Kinematics of the Gentle to Open Fault-propagation Fold having Four-way Dip Enclosure: Outcrop and Lineament Analysis of the Rois Anticline, Southern Kirthar Fold Belt, Pakistan. *Journal of Himalayan Earth Sciences* 58(1): 88-106 (2025).
17. A.A. Halepoto, M.H. Agheem, A.A.A.D. Hakro, S. Ahmed, and S.B. Ahmedani. Lateral Strike-slip Deformation and Possible Transition of Extensional Faults to Strike-slip Faults in the Foreland Fold Belt: A Regional to Outcrop Tectonic Synthesis of the Southern Kirthar Fold Belt, NW Indian Plate, Pakistan. *Journal of Asian Earth Sciences* 291: 106678 (2025).
18. Z. Ahmed, A.S. Khan, and B. Ahmed. Sandstone Composition and Provenance of the Nari Formation, Central Kirthar Fold, Pakistan. *Pakistan Journal of Geology* 4(2): 90-96 (2020).
19. A.A.A.D. Hakro, M.S. Samtio, R.H. Rajper, and A.S. Mastoi. Major Elements of Nari Formation Sandstone from Jungshahi Area of Southern Indus Basin, Pakistan. *Pakistan Journal of Scientific and Industrial Research Series A: Physical Sciences* 65(3): 248-259 (2022).
20. M.S. Samtio, A.A.A.D. Hakro, R.A. Lashari, A.S. Mastoi, R.H. Rajper, and M.H. Agheem. Depositional Environment of Nari Formation from Lal Bagh Section of Sehwan Area, Sindh Pakistan. *Sindh University Research Journal (Science Series)* 53(1): 67-76 (2021).
21. S.B. Ahmedani, A.A.A.D. Hakro, A.S. Mastoi, A.A. Halepoto, A.G. Sahito, S. Akhtar, and R.A. Lashari. Clastic Source and Depositional Environment of Mixed Carbonate-Clastic Sequences in the Oligocene Nari Formation from the Hundi Anticline, Karachi Embayment, Indus Basin, Pakistan. *Earth Sciences Research Journal* 29(2): 149-167 (2025).
22. A.M. Shar, A.A. Mahesar, G.R. Abbasi, A.A. Narejo, and A.A.A.D. Hakro. Influence of diagenetic features on petrophysical properties of fine-grained rocks of Oligocene strata in the Lower Indus Basin, Pakistan. *Open Geosciences* 13: 517-531 (2021).
23. A.M. Shar, A.A. Mahesar, A.A. Narejo, and N. Fatima. Petrography and Geochemical Characteristics of Nari Sandstone in Lower Indus Basin, Sindh, Pakistan. *Mehran University Research Journal of Engineering and Technology* 40(1): 82-92 (2021).
24. S.B. Ahmedani, M.H. Agheem, A.A.A.D. Hakro, A.A. Halepoto, R.A. Lashari, and G.M. Thebo. Integrated Petrographical, Mineralogical, and Geochemical Investigation to Evaluate Diagenesis of Sandstone: A Case Study of the Oligocene Nari Formation from Southern Kirthar Range, Pakistan. *Journal of Himalayan Earth Sciences* 57(1): 1-22 (2024).
25. F.K. Bender and H.A. Raza (Eds.). Geology of Pakistan. *Gebruder Borntraeger, Berlin, Germany* (1995).
26. A. Bilal, R. Yang, Y. Li, J. Zhang, H.T. Janjuhah. Microfacies shift in the Late Paleocene–Early Eocene Patala Formation in the Upper Indus Basin (Pakistan): Implications for development of the Ceno-Tethys Ocean. *Marine and Petroleum Geology* 161: 106693 (2024).
27. A.H. Kazmi and M.Q. Jan (Eds.). Geology and Tectonics of Pakistan. *Graphic Publishers, Karachi, Pakistan* (1997).
28. S.M.I. Shah (Ed.). Stratigraphy of Pakistan, Memoir 22. *Geological Survey of Pakistan, Quetta, Pakistan* (2009).
29. D. Bannert, A. Cheema, A. Ahmed, and U. Schaffer. The Structural Development of the Western Fold Belt, Pakistan. *Geologisches Jahrbuch Reihe B* 80: 3-60 (1992).
30. R. Ahmed and J. Ahmed. Petroleum Geology and Prospects of Sukkur Rift Zone, Pakistan with Special Reference to Jaisalmer, Cambay and Bombay High Basins of India. *Pakistan Journal of Hydrocarbon*

Research 3(2): 33-41 (1991).

31. A.H. Kazmi and R.A. Rana. Tectonic Map of Pakistan. *Geological Survey of Pakistan Map Series, Quetta, Pakistan* (1982).
32. A.H. Kazmi and I.A. Abbasi. Stratigraphy and Historical Geology of Pakistan. *National Centre of Excellence in Geology, University of Peshawar, Pakistan* (2008).
33. A. Laghari, M.Q. Jan, M.A. Khan, M H. Agheem, A.G. Sahito, and S. Anjum. Petrography and major element chemistry of mafic dykes in the Nagar Parkar Igneous Complex, Tharparkar, Sindh. *Journal of Himalayan Earth Science* 46(1): 1-11 (2013).
34. M.Q. Jan, A. Laghari, M.A. Khan, M.H. Agheem, and T. Khan. Petrology of calc-alkaline/adakitic basement hosting A-type Neoproterozoic granites of the Malani igneous suite in Nagar Parkar, SE Sindh, Pakistan. *Arabian Journal of Geosciences* 11: 25 (2018).
35. S. Ahmed, S.H. Solangi, M.S.K. Jadoon, and A. Nazeer. Tectonic evolution of structures in Southern Sindh Monocline, Indus Basin, Pakistan formed in multi-extensional tectonic episodes of Indian Plate. *Geodesy and Geodynamics* 9(2): 358-366 (2018).
36. S.A. Abbasi, S.H. Solangi, and A. Ali. Seismic Data Interpretation: A Case Study from Southern Sindh Monocline, Lower Indus Basin, Pakistan. *Mehran University Research Journal of Engineering and Technology* 34(2): 107-115 (2015).
37. B. Wahid, S. ul Alam, A.S. Khan, A.A. Halepoto, and S. Jalal. Reservoir Characterization of Lower Goru Formation Using Seismic and Well Logs Data, Mubarak Gas Field, Lower Indus Basin, Pakistan. *Sindh University Research Journal (Science Series)* 55(2): 7-17 (2023).
38. M.A. Qureshi, S. Ghazi, M. Riaz, and S. Ahmad. Geo-seismic model for petroleum plays an assessment of the Zamzama area, Southern Indus Basin, Pakistan. *Journal of Petroleum Exploration and Production Technology* 11(1): 33-44 (2021).
39. R.D. Lawrence, R.S. Yeats, S.H. Khan, A. Farah, and K.A. DeJong. Thrust and strike slip fault interaction along the Chaman transform zone, Pakistan. *Geological Society, London, Special Publications* 9(1): 363-370 (1981).
40. A. Farah, G. Abbas, K.A. De Jong, and R.D. Lawrence. Evolution of the lithosphere in Pakistan. *Tectonophysics* 105(1-4): 207-227 (1984).
41. W.E. Crupa, S.D. Khan, J. Huang, A.S. Khan, and A. Kasi. Active tectonic deformation of the western Indian plate boundary: A case study from the Chaman Fault System. *Journal of Asian Earth Sciences* 147: 452-468 (2017).
42. Hunting Survey Corporation, Reconnaissance Geology of Part of West Pakistan. *A Colombo Plan Co-operative Project, Toronto, Canada* (1960).
43. A. Khan, M. Imran, M. Iqbal, and A. Nazeer. Structural Styles and Hydrocarbon Potential of Western Kirthar Fold Belt. *PAPG-SPE Annual Technical Conference(7th - 9th November 2011), Islamabad, Pakistan* (2011).
44. R.L. Folk and W.C. Ward. Brazos River Bar: A Study in the Significance of Grain Size Parameters. *Journal of Sedimentary Petrology* 27(1): 3-26 (1957).
45. A.A.A.D. Hakro, A.A. Halepoto, A.S. Mastoi, M.S. Samtio, R.H. Rajpar, and A. Noonari. Depositional Environment of Neogene Foreland Deposits (Manchar Formation) from the Bara Nai Section of the Southern Indus Basin, Pakistan. *Pakistan Journal of Scientific and Industrial Research, Series A: Physical Sciences* 68A(1): 96-105 (2025).
46. S.S. Jagirani, L. Bai, M.D. Jagirani, S.A. Panhwar, B. Neupane, K. Jagirani, W. Ghanghro, U. Baral, and Q.D. Khokhar. Sedimentological Study of Manchar Formation, Kari Buthi Section, Northern Laki Range, Southern Indus Basin, Pakistan. *International Research Journal of Earth Sciences* 8(2): 9-21 (2020).
47. W.C. Krumbein. Size frequency distributions of sediments. *Journal of Sedimentary Research* 4(2): 65-77 (1934).
48. M. Khan, M.A. Khan, B.A. Shami, and M. Awais. Microfacies analysis and diagenetic fabric of the Lockhart Limestone exposed near Taxila, Margalla Hill Range, Punjab, Pakistan. *Arabian Journal of Geosciences* 11(2): (2018).
49. M. Rizwan, M. Hanif, N. Ali, and M. Ur Rehman. Microfacies analysis and depositional environments of the Upper Cretaceous Fort Munro Formation in the Rakhi Nala Section, Sulaiman range, Pakistan. *Carbonates and Evaporites* 35(4): (2020).
50. M. del C. Esqueda, E. Ríos-Jara, J.E. Michel-Morfín, and V. Landa-Jaime. The vertical distribution and abundance of gastropods and bivalves from rocky beaches of Cuastecomate Bay, Jalisco. México. *Revista de Biología Tropical*, 48(4): 765-775 (2000).
51. P. Zell, S. Beckmann, W. Stinnesbeck, and M. Götte. Mollusks of the upper Jurassic (upper Oxfordian-lower Kimmeridgian) shallow marine Minas Viejas formation, northeastern Mexico. *Journal of South American Earth Sciences* 62: 92-108 (2015).
52. A. Mancosu and J.H. Nebelsick. Echinoid

assemblages from the early Miocene of Funtanazza (Sardinia): A tool for reconstructing depositional environments along a shelf gradient. *Palaeogeography, Palaeoclimatology, Palaeoecology* 454: 139-160 (2016).

53. E.K. Yordanova and J. Hohenegger. Taphonomy of larger foraminifera: relationships between living individuals and empty tests on flat reef slopes (Sesoko Island, Japan). *Facies* 46: 169-203 (2002).
54. S.J. Beavington-Penney and A. Racey. Ecology of extant nummulitids and other larger benthic foraminifera: Applications in palaeoenvironmental analysis. *Earth-Science Reviews* 67(3-4): 219-265 (2004).
55. E. Özcan, A.O. Yücel, L.S. Erkızan, M.N. Gültekin, S. Kayğılı, and S. Yurtsever. Atlas of the Tethyan orthophragmines. *Mediterranean Geoscience Reviews* 4(1): 3-213 (2022).
56. A. Bilal, R. Yang, H. T. Janjuhah, M.S. Mughal, Y. Li, G. Kontakiotis, and N. Lenhardt. Microfacies analysis of the Palaeocene Lockhart limestone on the eastern margin of the Upper Indus Basin (Pakistan): Implications for the depositional environment and reservoir characteristics. *Depositional Record* 9(1): 152-173 (2023).
57. R.F. Gilham and C.S. Bristow. Facies architecture and geometry of a prograding carbonate ramp during the early stages of foreland basin evolution: lower Eocene sequences, Sierra del Cadí, SE Pyrenees, Spain. *Geological Society, London, Special Publications* 149(1): 181-203 (1998).
58. A. Abdullah, M. Mohibullah, A.K. Kasi, S. Ul Alam, and E. Ul Haq. Microfacies and Depositional Settings of the Eocene Nisai Formation, Pishin Belt, Pakistan. *Journal of Himalayan Earth Sciences* 56(1): 11-32 (2023).
59. U. Sarwar, S. Ghazi, S.H. Ali, M. Mehmood, M.J. Khan, A. Zaheer, and S.J. Arif. Sedimentological and sequence stratigraphic analysis of Late Eocene Kirthar Formation, Central Indus Basin, Pakistan, Eastern Tethys. *Earth Sciences Research Journal* 28(1): 29-38 (2024).
60. A.A.A.D. Hakro, W. Xiao, Z. Yan, and A.S. Mastoi. Provenance and tectonic setting of Early Eocene Sohnari Member of Laki Formation from southern Indus Basin of Pakistan. *Geological Journal* 53: 1854-1870 (2018).
61. G. Nichols (Ed.). Sedimentology and Stratigraphy. *Wiley-Blackwell, USA* (2009).
62. R.C. Selley (Ed.). Applied sedimentology. *Academic Press, London, UK* (2000).
63. S. Boggs (Ed.). Petrology of Sedimentary rocks. *Cambridge University Press, London, UK* (2009).
64. M. Lawal and M.H.A. Hassan. Sedimentary and stratigraphic characteristics of the Maastrichtian Dukamaje formation of southern Iullemmeden Basin: Implications for the paleogeography of the Upper Cretaceous trans-Saharan seaway. *Journal of African Earth Sciences* 200: 104878 (2023).
65. J.L. Melvin (Ed.) Evaporites, Petroleum and Mineral Resources. *Elsevier* (1991).
66. S.F. Könitzer, S.J. Davies, M.H. Stephenson, and M.J. Leng. Depositional controls on mudstone lithofacies in a basinal setting: implications for the delivery of sedimentary organic matter. *Journal of Sedimentary Research* 84(3): 198-214 (2014).
67. H.B. Stewart. Sedimentary Reflections of Depositional Environment in San Miguel Lagoon, Baja California, Mexico. *Bulletin of the American Association of Petroleum Geologists* 42(1): 2587-2618 (1958).
68. R. Passega. Grain size representation by CM patterns as a geologic tool. *Journal of Sedimentary Research* 34(4): 830-847 (1964).
69. B.K. Sahu. Depositional Mechanisms from the Size Analysis of Clastic Sediments. *Journal of Sedimentary Research* 34(1): 73-83 (1964).
70. S.K. Ghosh and B.K. Chatterjee. Depositional mechanisms as revealed from grain-size measures of the palaeoproterozoic kolhan siliciclastics, Keonjhar District, Orissa, India. *Sedimentary Geology* 89(3-4): 181-196 (1994).

Proceedings of the Pakistan Academy of Sciences: A Physical and Computational Sciences 62(2): 123-130 (2025)

ISSN (Print): 2518-4245; ISSN (Online): 2518-4253
http://doi.org/10.53560/PPASA(62-2)684

Pakistan Academy of Sciences

Research Article

Evaluation of Potential Sites for Solar Powered Irrigation System in Gilgit-Baltistan for Sustainable Agriculture

Arshad Ashraf*, Muhammad Bilal Iqbal, and Imran Ahmad

Climate, Energy and Water Research Institute, National Agricultural Research Center,
Islamabad, Pakistan

Abstract: The depletion of glaciers and frequent occurrence of glacial floods and landslide hazards typically affect the irrigation channels, resulting in disruption of water supplies for irrigation and domestic use in the Upper Indus Basin (UIB). The cultivated and arable land requires sustainable and alternative irrigation sources, such as using river/stream water through solar-powered irrigation system (SPIS), to ensure food security in the region. An effort has been made to assess the potential of SPIS in Gilgit-Baltistan (GB) province, lying in the UIB of Pakistan, based on the climate and topographic indexing approach. The SPIS potential was found to be high over 2153 km² and moderate over 3786 km² (collectively over 5939 km²) of the GB based on the slope-aspect (SLA) suitability. The high and moderate SLA suitability areas for SPIS were observed collectively over 22.9% of the Diamer, 16.9% of the Gilgit, and 8.8% of the Astore District. The SLA suitability was observed high over 11.2% and moderate over 19.2% area of the cropping zone below 3500 m elevation in the GB. The SPIS system may be adopted through coupling with some storage facility (water tanks, ponds, or reservoirs) and high efficient irrigation system (drip, sprinkler, and bubbler) for raising high value crops and multipurpose plant species, while reducing water consumption, fuel and labor cost. Integrated water resources management strategies need to be developed and implemented to cultivate unused lands in the valleys to ensure food security and economic development in the region in future.

Keywords: Climate Change, Drip Irrigation, Glacial Retreat, Indus Basin, Solar Radiation.

1. INTRODUCTION

Water demand is increasing rapidly in wake of growing urbanization, agriculture land use, change in social worth and climate change [1]. Moreover, adequate and economical availability of energy sources is crucial for meeting energy demand for agricultural water management. Climate change is causing serious glacial retreat/surging, avalanche, landslide and glacial lakes outburst flood (GLOF) hazards impacting the social and physical infrastructure in the Upper Indus Basin (UIB) [2]. As a result of increased warming, i.e., more than the world average temperature, most of the glaciers exhibit varying degree of retreat in the Himalayan region [3-5], except the Karakoram where most of the glaciers indicate stable behavior likely because of conducive environment [6-9]. The changing behavior of cryosphere would ultimately affect stream flow, irrigation potential and food production system. Water is crucial in bringing new area under cultivation in this region. The meltwater flows nurturing vast cryosphere-fed irrigation network are frequently disrupted by glacier retreat and lowering of the glacial surface in the region [10, 11]. The irrigation channels were also damaged many times owing to severe GLOF/flash flood and landslide events, consequently affecting crop farming and agricultural livelihoods [12-15]. Solar energy has become a highly valuable resource owing to intense global interest in climate change mitigation [16]. Pakistan is facing an unprecedented energy crisis owing to the increasing cost of diesel and electricity and frequent shutdowns of electricity. The growing population in GB, i.e., 0.56 million in 1981 to over 1.7 million in 2022, needs efficient energy sources for sustainable agriculture and livelihood improvement. Solar energy is available for over 300 days a year in Pakistan [17] and over 95% of the country's area receives solar radiation incident

---

Received: November 2024; Revised: May 2025; Accepted: June 2025
* Corresponding Author: Arshad Ashraf <mashr22@yahoo.com>

within a range of 5-7 kWh/m²/day with a persistence factor of over 85% [18]. Photovoltaic (PV)-based water pumping systems have become increasingly important because they use the clean, renewable energy of the sun, which accounts for the high cost of diesel and the limited supply of electricity. In a solar-powered water pump system, a bore/surface pump is driven by an electric motor that is powered by electricity produced by one or more solar panels. The pumped water is generally stored in a tank to make possible gravity-fed irrigation. The National Water Policy 2018 of Pakistan emphasized promoting measures for the long-term sustainability of the irrigation system to support food security in the country. Solar-powered irrigation system (SPIS) can be adopted to utilize the river/stream water for sustaining agriculture and livelihoods in the region [19, 20]. When compared to traditional fuel-based pumping systems, the versatile SPIS system has a longer operational life and lower maintenance cost. SPIS offers a promising substitute to diesel pumps, which contribute to carbon emissions and climate change.

The majority of arable land alongside the rivers, such as the Indus, Gilgit, Hunza, Shigar, Shyok, and Astore, and the perennial streams, remain fallow because of limited access to water supplies. There is a need to adopt irrigation system that could ensure water and food security and improve the livelihoods of a number of communities residing along the riverbanks under changing climate and cryosphere. It is hypothesized that considerable potential exists for establishing the SPIS to sustain agriculture and livelihoods in this region. This paper is aimed at assessing the potential of SPIS in the valley areas of Gilgit-Baltistan (GB), Pakistan, based on the climate and topographic indexing approach.

2. MATERIALS AND METHODS

2.1. Geographical Setup

The study area of GB (about 72,971 km^2) lies within elevation range from < 1000 m to > 8000 m in the northern Pakistan (Figure 1). Climate is predominantly warm continental/mediterranean continental to humid sub-tropical and arctic/ cold desert with mean minimum temperature about 7 °C and maximum about 21 °C per annum. Annual rainfall ranges between 125 and 600 mm, which generally occurs from the westerly during winters and the monsoon during summers, besides a small amount from the local thunderstorms [10]. Majority of the households in the GB are engaged in subsistence agriculture. On an average, the land holding for cultivation is 0.2 hectare per household in the region. In the lower arid valleys below 1900 m, crops are grown in both summer and winter seasons (typically wheat is grown during winters and maize during summers). In the highlands, only single crop is cultivated during summers, and between 1900 and 2300 m, marginal single crop cultivation is practiced which can be transformed into double cropping using early maturing barley and wheat types [10]. Water supply is mainly managed through channels fed by springs, snow/glacier melt and river/stream water, which occasionally become disrupt due to climate induced disasters like floods, landslides and snow avalanches occurred during mid-summers.

The highlands are characterized by rugged and difficult mountainous terrain consisting of gravelly fans and terraces. The land use/land cover includes rangeland (grazing areas) over 33%, bare ground over 39%, snow cover and glaciers over 25%, and, agricultural land over < 2% area, besides other classes (Figure 1). Agriculture is generally practiced in the valleys and some sloppy areas in the region. The main crops grown include wheat, barley, maize, potatoes, buckwheat, millet, vegetables and fruits [21]. The major vegetables consist of tomatoes, potatoes, peas, onions, beans, carrots, turnips, spinach, while fresh and dry fruits include apples, apricots, cherries, pears, mulberries, grapes, plums, almonds and walnuts. The sowing season generally starts in early February and continues till second week of April in the highlands. The

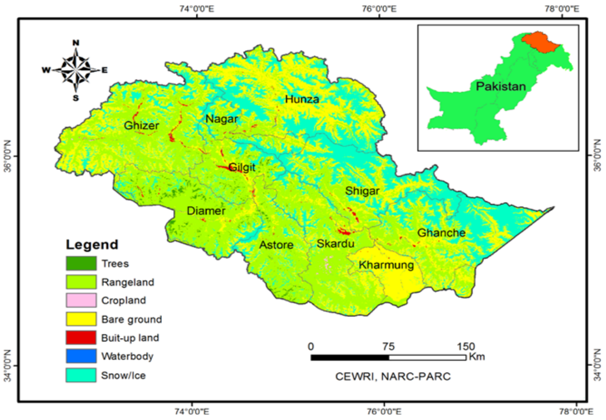

Fig. 1. Location of Gilgit-Baltistan study area in northern Pakistan.

harvesting season begins in mid-July in the lower regions and continues till the end of October in the upper reaches of the region.

2.2. Data Source

Thematic data of topography, land forms, land use, hydrology (drainage network, river discharges) and climate were acquired from source departments like Survey of Pakistan, Soil Survey Water and Power Development Authority, and Pakistan Meteorological Department (PMD). The monthly climate data (i.e., temperature and rainfall) of the selected meteorological stations, i.e., Gilgit, Gupis, Bunji, Astore, and Skardu (1990-2019 period), were acquired from PMD for variability and spatial trend analysis. The Sentinel-2 based global land use/land cover map (2022) available at ESRI site (https://livingatlas.arcgis.com) was used for land use/land cover analyze of the study area. The Shuttle Radar Topography Mission SRTM-DEM data of 90 m resolution was downloaded from the National Aeronautics and Space Administration (NASA) site (www.jpl.nasa.gov/) for developing elevation, slope and aspect maps of the study area. Field surveys were carried out to gather information of landforms, land use, agriculture, water resources and socioeconomics from various locations of the study region.

2.3. Determination of SPIS Potential

SPIS potential was explored in the region through adopting a climate and topographic (slope, aspect, altitude) indexing approach [22]. The efficiency of the PV cell that transforms sunlight into useful energy is defined by the ratio of maximum power output to the power received by the cell [23]. The efficiency of panel increases as the temperature declines, while it falls as the voltage between the cells falls at high temperatures [24, 25]. Solar panels can operate most efficiently between 15 and 40°C; temperatures above this range will reduce solar cell efficiency [24]. Since solar radiation and sunshine length are crucial factors in evaluating the effectiveness of renewable energy systems, the effects of slope and aspect on solar energy are especially important in mountainous terrain [26]. According to Kereush and Perovych [25], sites above 1500 m elevation are also suitable for setting up the solar-powered systems, so it is presumed that all altitudes in this region are equally effective at gathering solar energy. A slope map was generated using the DEM and reclassified into two classes, i.e., < 35° and > 35°. The slope < 35° was considered suitable and assigned value 1 as allowing more perpendicular light and receiving higher solar radiations than other slope class feasible for the system's operation [27, 28].

The length of sunshine hours and the amount of solar energy available have been represented in this study by the aspect factor. Aspect classes, i.e., south, southeast, and east, were deemed appropriate for SPIS installation because they received more solar energy and retained more sunshine duration than other aspect classes, whereas shadow areas in mountainous terrain received the least amount of solar energy to harness [22]. The south aspect was given the maximum weight of 2 due to its higher aptness for receiving solar energy than other aspects in this area. The East-Southeast (E-SE) aspects were assigned weight 1 since they were deemed to be medium suitable for receiving solar radiation, whereas other aspect classes were allocated weight zero as inappropriate for harnessing solar radiation. A slope-aspect (SLA) index was developed to define three land suitability classes for establishing SPIS, i.e., High (< 35° slope at S aspect), Moderate (< 35° slope at E-SE aspects) and Low (>35° slope at all aspects excluding S, E and SE). A final SLA suitability map was prepared for the GB area based on the weighted overlay analysis, and spatial analysis was performed at district level in the ArcGIS software for planning and decision-making.

3. RESULTS AND DISCUSSION

3.1. Assessment of SPIS Potential

Mean maximum temperature indicated a decreasing trend towards the northeast in this region (Figure 2). The temperature range 10 - 20 °C appears dominant in most of the northwestern, central, and southeastern parts, while > 20 °C temperature seems prominent in the southern parts of the area. A mean minimum temperature range of 0 - 10 °C appears dominant in the NW-SE belt, while > 10 °C prevails in the southern valleys of the region. The temperature range below zero appears concentrated in the high mountainous region towards the northeast (Figure 2). Overall, the majority of the valleys and depressions have mean annual temperatures above 15 °C. Summers have high solar radiation, whereas winters have low solar radiation in this region [29]. The region contains an extensive network of perennial streams and rivers fed by rainwater, permanent snow, and numerous small and large glaciers residing at higher reaches (Figure 2). The stream/river flows are large during May to August, while the irrigation requirements are large from April to June. The slope class < 35° derived from the DEM was identified over 90% of the study area (Figure 3). Most of this slope class lies in the Ghizer, Hunza, Ghanche, and Skardu districts (Table 1). Over 13% of the area was found under the southern aspect class, the majority of

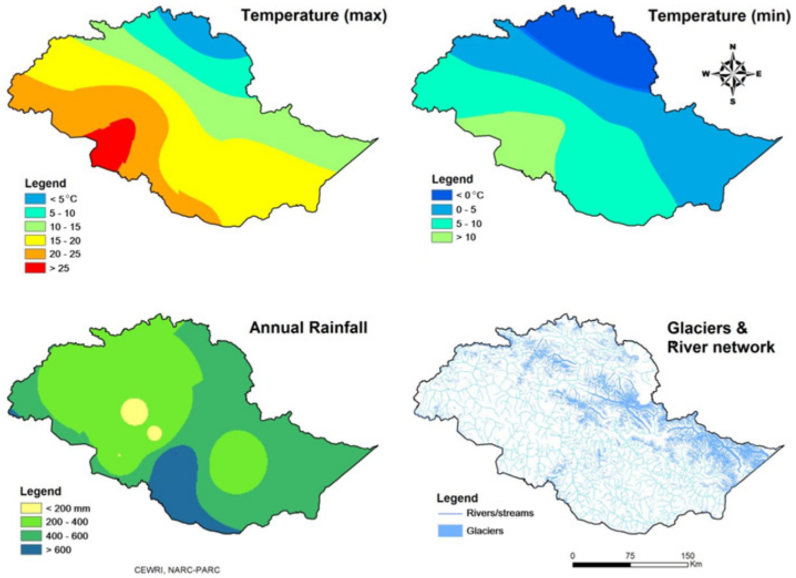

Fig. 2. Spatial analysis of hydro-climate in the GB area.

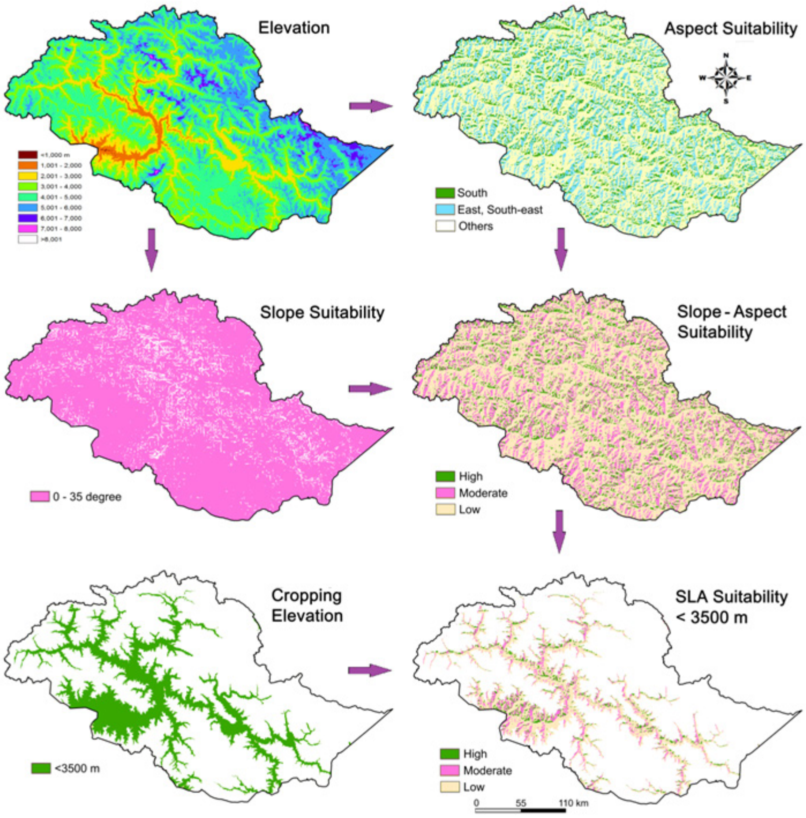

Fig. 3. Assessment of slope-aspect (SLA) suitability for establishing SPIS in the GB area.

Table 1. The slope and aspect suitability areas (in km^2) for SPIS in different districts of the study area.

District	Slope < 35°	South	E-SE
Ghizer	11404	1556	3134
Gilgit	3763	555	1089
Nagar	1958	291	575
Hunza	11134	1763	2931
Shigar	7455	1228	2009
Ghanche	8520	1311	2401
Kharmung	2566	314	595
Skardu	7710	969	2149
Diamer	6863	860	1778
Astore	4959	619	1280
Total	66331	9465	17940

which lies in the Hunza, Ghizer, Ghanche, and Shigar districts. This aspect was observed over a < 700 km² area in the Nagar, Kharmung, Gilgit, and Astore districts. The E-SE class covers about 24.6% of the area, predominantly in the Ghizer, Hunza, Ghanche, and Skardu districts (Table 1). The coverage of this class was observed within 500-600 km² in the Nagar and Kharmung districts. The SLA suitability was found to be high over 2153 km^2 and moderate over 3786 km^2 of the study area (Figure 3). Among various districts, the suitability was observed high over 532 km^2 area of the Diamer, 357 km^2 of the Ghizer, 252 km^2 of the Gilgit and 215 km^2 of the Hunza District (Figure 4). Similarly, the moderate suitability was found over 1128 km^2 area of the Diamer, 573 km^2 of the Ghizer, 483 km^2 of the Gilgit and 359 km^2 of the Skardu District. Collectively, high and moderate SLA suitability for SPIS was observed over 22.9% area of the Diamer, 16.9% of the Gilgit and 8.8% area of the Astore District (Figure 5).

3.2. SPIS Potential Below 3500 m Elevation

Agriculture is typically practiced in the valleys and some sloppy areas below 3500 m elevation. The climatic condition below 3500 m elevation is generally suitable for crop farming and livelihoods in the region [10]. About 22% of the GB area (i.e., 15975 km^2) lies below 3500 m elevation, in which major area lies in the Diamer, Ghizer and Gilgit districts (Table 2). The slope class < 35° covers about 14325 km^2 area, majority of which lies in the Diamer (3973 km^2), Ghizer (2176 km^2), Gilgit (1711 km^2), Astore (1333 km^2), Skardu (1307 km^2) and Hunza districts (1041 km^2). The least area of this class exists in the Nagar (445 km^2), Kharmung (594 km^2), Ghanche (856 km^2) and Shigar districts (889 km^2). The southern aspect stretches over 1979 km^2 and E-SE aspects over 3511 km^2 area, majority of which lie in the Diamer, Ghizer and Gilgit districts. The SLA suitability below 3500 m elevation was found to be high over 11.2% (1792 km^2) and moderate over 19.8% (3167 km^2) of the area. Diamer has the maximum of about 4216 km^2 area under 3500 m elevation, in which SLA suitability was found high over 11.7% and moderate over 24.6% area of the district (Table 2). According to a study by Ali *et al.* [29], Chilas in the Diamer District has a good solar profile with a maximum irradiance of about 7.981 kWh/m²/day in July, while Khaplu in the Ghanche District has the least irradiance of about 1.783 kWh/m²/day in December. The SLA suitability was identified high over 8 to 11% area in the five districts, i.e., Gilgit, Nagar, Kharmung, Skardu and Astore, and > 12% area in the Hunza and Shigar districts. The suitability was found to be moderate over 16 to 18% area in the Ghizer, Nagar, Hunza, Shigar and Ghanche districts. Overall, the SLA suitability for

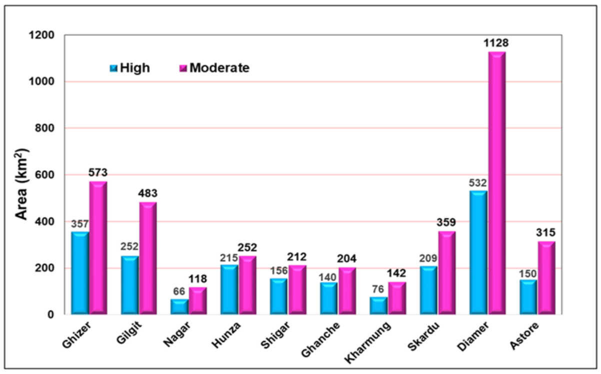

Fig. 4. The slope-aspect suitability for SPIS in different districts of the study area.

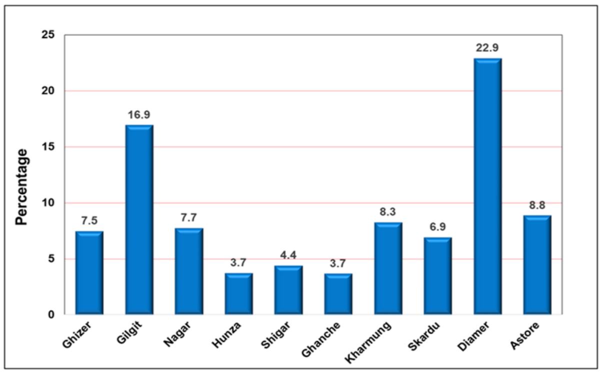

Fig. 5. Percentage coverage of collective high and moderate SLA suitability in different districts.

establishing SPIS was observed high over 11.2%, moderate over 19.2%, and low over 69% of the area below 3500 m elevation in the GB (Table 2 and Figure 3). The latter low suitability area of the SLA points toward the existence of > 35° slopes at other than S, E and SE aspects, assuming a non-promising area for establishing SPIS.

3.3. Adoption of SPIS for Sustainable Agriculture

SPIS can benefit farmlands in a number of ways, including less reliance on fossil fuels and electricity, lower operating costs, and less environmental impact [30]. Several researchers have thoroughly documented the potential impacts of various elements in the SPIS, including the design of the PV pumping system, water source characteristics, irrigation technique and local climate to achieve maximum efficiency [31, 32]. The system consists of equipment such as pumping units, pump controllers, and photovoltaic modules. The SPIS is generally implemented and promoted, especially in areas with little access to conventional irrigation supplies. It can be adopted for converting cultivable land into productive land in the valleys and to uplift meltwater from a lower water input point at a depleted glacier to an irrigation channel at an elevated area to sustain water supply in the channel. The solar-powered water pumps have the benefit of significantly lower labor and maintenance costs [33, 34], which is supportive for areas facing labor shortages owing to outmigration. When combined with efficient irrigation methods, the water-lifting mechanism can be used to grow high-value crops like fruits and vegetables in unused land alongside the perennial streams and rivers. The drip irrigation linked with solar-powered system has advantages for water conservation, fewer chances of soil erosion, and reduction in pest attacks/disease. Compared to other irrigation techniques, this method increases irrigation efficiency by up to 90%, making it the most appreciated innovation for water security. Pakistan Agricultural Research Council (PARC) and several other institutions have adopted the SPIS for growing high-value crops (vegetables and fruits) in various parts of the region.

Table 2. Percentage coverage of SLA suitability for SPIS below 3500 m elevation in different districts.

District	Area below 3500 m (km^2)	High (%)	Moderate (%)	Low (%)
Ghizer	2493	11.4	17.5	71.1
Gilgit	1971	10.6	19.5	69.9
Nagar	514	10.9	17.2	71.9
Hunza	1188	14.1	17.2	68.7
Shigar	1018	12.5	17.2	70.3
Ghanche	987	11.6	16.7	71.7
Kharmung	637	9.1	19.1	71.8
Skardu	1522	10.8	19.3	69.9
Diamer	4216	11.7	24.6	63.7
Astore	1429	8.1	18.4	73.5
Total	15975	11.2	19.8	69.0

Although solar pumps are initially more costly compared to diesel pumps, they require fewer operation and maintenance costs over time [35]. To help offset the high upfront costs, the local communities may be encouraged to adopt SPIS through the provision of subsidies and adequate financial incentives. In cases where the system may face power outages during prolonged cloud cover (due to a shortage of sunlight), integrated water resources management plans may be developed and implemented to sustain crop farming activities. Ali *et al.* [29] recommended appropriate hybrid systems to meet the energy demand at selected locations of the GB. Capacity building of the communities and institutions is necessary to address the SPIS challenges such as water delivery, storage, and system maintenance in the region. The male and female farmers need to be trained in water conservation, kitchen gardening, and raising fruit nurseries and orchards using SPIS-coupled efficient irrigation system to improve their livelihoods.

4. CONCLUSIONS

In this study, potential of SPIS has been assessed in the valley areas of GB, Pakistan, using the indexing approach. The SPIS potential was found to be high over 2153 km^2 and moderate over 3786 km^2 (collective over 5939 km^2) of the study area based on the slope and aspect suitability. It was observed high over 532 km^2 of the Diamer, 357 km^2 of the Ghizer, 252 km^2 of the Gilgit and 215 km^2 area of the Hunza District. The SLA suitability for SPIS was observed high over 11.2% and moderate over 19.2% area of the cropping zone below 3500 m elevation. Diamer has the maximum area under 3500 m elevation, where SLA suitability was determined to be high over 11.7% and moderate over 24.6% of the district. The suitability of SLA was found to be high across 8 to 11% areas of the Gilgit, Nagar, Kharmung, Skardu, and Astore districts, while it was > 12% in the Shigar and Hunza districts. The moderate suitability of SLA was observed over 16 to 18% areas of the Ghizer, Nagar, Hunza, Shigar, and Ghanche districts. The SPIS can be adopted through coupling with some storage facility and drip irrigation system for raising high value crops (vegetables and fruits) and multipurpose tree species in the arable land along major rivers and streams. Integrated water resources management plans may be developed and implemented in arable and unused lands to ensure food security, ecosystem health, and economic development in the region in future.

5. CONFLICT OF INTEREST

The authors declare no conflict of interest.

6. REFERENCES

1. IPCC. Summary for Policymakers. In: Intergovernmental Panel on Climate Change Special Report on the Ocean and Cryosphere in a Changing Climate. H.-O. Pörtner, D.C. Roberts, V. Masson-Delmotte, P. Zhai, M. Tignor, E. Poloczanska, K. Mintenbeck, A. Alegría, M. Nicolai, A. Okem, J. Petzold, B. Rama, and N.M. Weyer (Eds.). *Cambridge University Press, Cambridge, UK and New York, NY, USA* pp. 3-35 (2019). https://www.ipcc.ch/site/assets/uploads/sites/3/2022/03/01_SROCC_SPM_FINAL.pdf.
2. S.R. Bajracharya, S.B. Maharjan, and F. Shrestha. The glaciers of the Hindu Kush Himalayas: Current status and observed changes from the 1980s to 2010. *International Journal of Water Resources Development* 31: 1-13 (2015).
3. G. Rasul, Q.Z. Chaudhry, and A. Mahmood. Glaciers and glacial lakes under changing climate in Pakistan. *Pakistan Journal of Meteorology* 8(15): 1-8 (2011).
4. F. Brun, E. Berthier, P. Wagnon, A. Kääb A, and D. Treichler. A spatially resolved estimate of High Mountain Asia glacier mass balances, 2000–2016. *Nature Geoscience* 10(9): 668-673 (2017).
5. R.A. Mir and Z. Majeed. Frontal recession of Parkachik Glacier between 1971-2015, Zanskar Himalaya using remote sensing and field data. *Geocarto International* 33(2): 163-177 (2018).
6. K. Hewitt. The Karoram anomaly? Glaciers expanding and the elevation effect Karakoram Himalaya. *Mountain Research and Development* 25(4): 332-340 (2005).
7. J. Gardelle, E. Berthier, and Y. Arnaud. Slight mass gain of Karakoram glaciers in the early twenty-first century. *Nature Geoscience* 5: 322-325 (2012).
8. F. Brun, E. Berthier, P. Wagnon, A. Kääb, and D. Treichler. A spatially resolved estimate of High Mountain Asia glacier mass balances from 2000 to 2016. *Nature Geoscience* 10: 668-673 (2017).
9. D. Farinotti, W.W. Immerzeel, R.J. de Kok, D.J. Quincey, and A. Dehecq. Manifestations and mechanisms of the Karakoram glacier anomaly. *Nature Geoscience* 13: 8-16 (2020).
10. A. Ashraf and I. Ahmad. Prospects of cryosphere-fed Kuhl irrigation system nurturing high mountain agriculture under changing climate in the Upper Indus Basin. *Science of the Total Environment* 788: 147752 (2021).
11. S. Parveen, M. Winiger, S. Schmidt, and M. Nüsser. Irrigation in upper Hunza: Evolution of socio-hydrological interactions in the Karakoram, northern Pakistan. *Erdkunde* 69 (1): 69-85 (2015).
12. A. Ashraf and G. Akbar. Addressing climate change risks influencing cryosphere-fed Kuhl irrigation system in the Upper Indus Basin of Pakistan. *International Journal of Environment* 9(2): 184-203 (2020).
13. S. Muhammad, J. Li, F.S. Jakob, F. Shrestha, G.M. Shah, E. Berthier, L. Guo, L. Wu, and L. Tian. A holistic view of Shisper Glacier surge and outburst floods: from physical processes to downstream impacts. *Geomatics, Natural Hazards and Risk* 12(1): 2755-2775 (2021).
14. F. Shrestha, J.F. Steiner, R. Shrestha, Y. Dhungel, S.P. Joshi, S. Inglis, A. Ashraf, S. Wali, K.M. Walizada, and T. Zhang. A comprehensive and version-controlled database of glacial lake outburst floods in High Mountain Asia. *Earth System Science Data* 15: 3941-3961 (2023).
15. A. Rahman, A.N. Khan, A.E. Collins, and F. Qazi. Causes and extent of environmental impacts of landslide hazard in the Himalayan region: a case study of Murree, Pakistan. *Natural Hazards* 57(2): 413-434 (2011).
16. C.L. Crago and I. Chernyakhovskiy. Are policy incentives for solar power effective? Evidence from residential installations in the Northeast. *Journal of Environmental Economics Management* 81: 132-151 (2017). https://www.unicef.org/pakistan/media/3166/file/MICS%202016-17%20GB%20Key%20Findings%20Report.pdf.
17. H.N. Khalil and S.J.H Zaidi. Energy crisis and

potential of solar energy in Pakistan. *Renewable and Sustainable Energy Reviews* 31: 194-201 (2014).

18. M.K. Farooq and S. Kumar. An assessment of renewable energy potential for electricity generation in Pakistan. *Renewable and Sustainable Energy Reviews* 20: 240-254 (2013).
19. A. Ashraf and A. Batool. Evaluation of glacial resource potential for sustaining kuhl irrigation system under changing climate in the Himalayan region. *Journal of Mountain Science* 16 (5): 1150-1159 (2019).
20. M.P. Dhakal, A. Amjad, M.Z. Khan, N. Wagle, G.M. Shah, M.M. Maqsood, and A. Ali. Agricultural water management challenges in the Hunza River Basin: Is a solar water pump an alternative option?. *Irrigation and Drainage* 70 (4): 644-658 (2021).
21. A. Hussain, S. Khan, S. Liaqat, and Shafiullah, Developing evidence based policy and programmes in mountainous specific agriculture in Gilgit-Baltistan and Chitral regions of Pakistan. *Pakistan Journal of Agricultural Research* 35(1): 181-196 (2022).
22. A. Ashraf and K. Jamil. Solar-powered irrigation system as a nature-based solution for sustaining agricultural water management in the Upper Indus Basin. *Nature-Based Solutions* 2: 100026 (2022).
23. A.S. Al-Ezzi and M.N.M. Ansari. Photovoltaic Solar Cells: A Review. *Applied System Innovation* 5 (4): 67 (2022).
24. S.S.M. Shaban. The solar cell parameters as a function of its temperature in relation to its diurnal efficiency. *Optics and Photonics Journal* 10: 1-12 (2020).
25. D. Kereush and I. Perovych. Determining criteria for optimal site selection for solar power plants. *Geomatics, Land Management and Landscape* 4: 39-54 (2017).
26. M.S. Gadiwala, A. Usman, M. Akhtar, and K. Jamil. Empirical models for the estimation of Global solar radiation with sunshine hours on horizontal surface in various cities of Pakistan. *Pakistan Journal of Meteorology* 9(18): 43-49 (2013).
27. J. Brewer, D.P. Ames, D. Solan, R. Lee, and J. Carlisle. Using GIS analytics and social preference data to evaluate utility-scale solar power site suitability. *Renewable Energy* 81: 825-836 (2015).
28. M. Tahri, M. Hakdaoui, and M. Maanan. The evaluation of solar farm locations applying Geographic Information System and Multi-Criteria Decision-Making methods: Case study in southern Morocco. *Renewable and Sustainable Energy Reviews* 51: 1354-1362 (2015).
29. M. Ali, R. Wazir, K. Imran, and K. Ullah. Techno-economic and environmental analysis of renewable energy integration in irrigation systems: A comparative study of standalone and grid-connected PV/diesel generator systems in Khyber Pakhtunkhwa. *Energy Reports* 7: 2546-2562 (2021).
30. B. Eker. Solar powered water pumping systems. *Trakia Journal of Sciences* 3(7): 7-11 (2005).
31. S. Mekhilef, S.Z. Faramarzi, R. Saidur, and S. Zainal. The application of solar technologies for sustainable development of agricultural sector. *Renewable and Sustainable Energy Reviews* 18: 583-594 (2013).
32. C.S. Guno and C.B. Agaton. Socio-economic and environmental analyses of solar irrigation systems for sustainable agricultural production. *Sustainability* 14(11): 6834 (2022).
33. L.R. Valer, T.A. Melendez, M.C. Fedrizzi, R. Zilles, and A.M. de Moraes. Variable-speed drives in photovoltaic pumping systems for irrigation in Brazil. *Sustainable Energy Technologies and Assessments* 15: 20-26 (2016).
34. C. Protoger and S. Pearce. Laboratory evaluation and system sizing charts for a second generation direct PV-powered, low cost submersible solar pump. *Solar Energy* 68(5): 453-74 (2000).
35. A.P. Rizi, A. Ashrafzadeh, and A. Ramezani. A financial comparative study of solar and regular irrigation pumps: Case studies in eastern and southern Iran. *Renewable Energy* 138: 1096-1103 (2019).

Proceedings of the Pakistan Academy of Sciences: A Physical and Computational Sciences 62(2): 131-136 (2025)

ISSN (Print): 2518-4245; ISSN (Online): 2518-4253
http://doi.org/10.53560/PPASA(62-2)860

Pakistan Academy of Sciences

Research Article

Coefficient Bounds for Certain Classes of Analytic Functions of Complex Order γ Associated with Cardioid Domain

Aijaz Ahmed Bhatti[1*], Abdul Wasim Shaikh[1], and Shujaat Ali Shah[2]

[1]Institute of Mathematics and Computer Science, University of Sindh, Jamshoro, Pakistan,
[2]Department of Mathematics and Statistics, Quaid-e-Awam University of Engineering, Science and Technology, Nawabshah, Pakistan

Abstract: In this paper, new Ma–Minda type subclasses of analytic functions of complex order γ, associated with the cardioid domain in the open unit disk $\mathbb{E}$, are introduced. The objective of this work is to investigate the first three sharp coefficient bounds and to examine the sharp estimates of the Fekete-Szegö problem for these subclasses.

Keywords: Analytic Functions, Starlike and Convex Functions, Cardioid Domain, Subordination, Coefficient Bounds, Fekete-Szegö Problem.

1. INTRODUCTION

In Geometric Function Theory, the classes $\mathcal{S}^*$ and $\mathcal{C}$, consisting of starlike and convex univalent functions respectively, are considered as the most extensively investigated subclasses of the class $\mathcal{S}$ of univalent functions in the open unit disk $\mathbb{E} = \{z \in \mathbb{C}: |z| < 1\}$, and have been of major interest. We refer the reader to [1-5] for the basic theory of univalent functions, and to Duren [6] for a detailed review of starlike and convex functions. A central focus in this area is the investigation of coefficient problems and the Fekete-Szegö inequality, which provide deep insights into the behavior of such functions. For detailed discussions on the coefficient problem and the Fekete–Szegö inequality with related problems, see [7-9] and [10-12], respectively. To unify and extend the study of these and related subclasses, Ma–Minda form of analytic functions are used, which offers a unified approach to several subclasses of analytics functions through subordination techniques.

In this work, we introduce new Ma–Minda type subclasses of starlike and convex analytic functions connected with a cardioid domain and examine their geometric properties, including sharp coefficient bounds and the Fekete-Szegö problem. To proceed, we recall and review the following fundamental definitions, which will serve as the basis for our present study.

Let $\mathcal{A}$ be the class of analytic functions f, defined on $\mathbb{E} = \{z \in \mathbb{C}: |z| < 1\}$, satisfying $f(0) = 0$, $f'(0) = 1$, and having the following form:

$$f(z) = z + \sum_{n=2}^{\infty} a_n z^n \tag{1}$$

Let $\mathcal{S}$ be the subclass of $\mathcal{A}$ consisting of univalent functions f. Consider a subclass $\mathcal{P} \subset \mathcal{A}$, which includes functions with positive real part and admits the following power series expansion:

$$p(z) = 1 + \sum_{n=1}^{\infty} c_n z^n\,; \quad (z \in \mathbb{E}) \tag{2}$$

Let f and g be analytic in the open unit disk. we say that f is subordinate to g, written as $f \prec g$, if there exists a function u, analytic in $\mathbb{E}$, satisying $u(0) = 1$ and $|u(z)| < 1$ such that $f(z) = g(u(z))$. Moreover, if the function g is univalent in $\mathbb{E}$, then, $f \prec g \Leftrightarrow f(0) = g(0)$ and $f(\mathbb{E}) \subset g(\mathbb{E})$.

Received: May 2024; Revised: May 2025; Accepted: June 2025
* Corresponding Author: Aijaz Ahmed Bhatti <Aijaz.Bhatti@usindh.edu.pk>

In 1992, Ma and Minda [13] using the concept of subordination, introduced the following suclasses of starlike and convex functions respectively.

$$S^*(\varphi) = \left\{ f \in \mathcal{A}: \frac{zf'(z)}{f(z)} \prec \varphi(z) \right\} \tag{3}$$

and

$$C(\varphi) = \left\{ f \in \mathcal{A}: 1 + \frac{zf''(z)}{f'(z)} \prec \varphi(z) \right\} \tag{4}$$

Where the function $\varphi(z)$ satisfying $Re(\varphi(z)) > 0$, the image $\varphi(\mathbb{E})$ is symmetric with respect to the real axis, starlike with respect to the point $\varphi(0) = 1$ and $\varphi'(0) > 0$. It is worth noting that these classes encompass and unify many important subclasses of $\mathcal{A}$. For example, setting $\varphi(z) = \frac{1+A_1 z}{1+A_2 z}$ with $-1 \leq A_2 < A_1 \leq 1$, in (3) and (4), we obtained the renowned classes of Janowski starlike and convex functions, represented by $S^*[A_1, A_2]$ and $C[A_1, A_2]$, respectively, studied by Janowski [14]. In addition, if we take $A_1 = 1 - 2 \propto$ and $A_2 = -1$ with $0 \leq \propto < 1$, then $S^*(\varphi)$ and $C(\varphi)$ becomes $S^*(\propto)$ and $C(\propto)$, which are the classes of starlike and convex functions of order $\propto$ respectively, defined by Robertson [15]. The classes $S^*_{sin} = S^*(1 + sin\, z)$ and $S^*_{exp} = S^*(e^z)$ were studied by Cho *et al.* [16] and Aouf *et al.* [17], respectively. By choosing $\left(\frac{1+z}{1-z}\right)$ and $\sqrt{1+z}$ as specific forms of $\varphi(z)$, the class $S^*(\varphi)$ reduces to the classical starlike class $S^*$and the class S^*_L defined by Sokoł and Stankiewicz [18], respectively.

For $\varphi(z) = 1 + ze^z$, Kumar and Kamaljeet [19] introduced the subclass $\mathfrak{S}^*_{\wp}$ of of starlike functions defined by:

$$\mathfrak{S}^*_{\wp} = \left\{ f \in \mathcal{A}: \frac{zf'(z)}{f(z)} \prec 1 + ze^z =: \varphi(z) \right\} \tag{5}$$

where the image of the unit disk under φ is a cardioid domain.

For $\varphi(z) = 1 + \frac{4z}{3} + \frac{2z^2}{3}$, the class reduces to S^*_c, investigated by Sharma *et al.* [20], containing functions $f \in \mathcal{A}$ such that $\frac{zf'(z)}{f(z)}$ mapped into the region enclosed by the cardioid described by the following Equation.

$$16(9x^2 + 9y^2 - 6x + 1) - (9x^2 + 9y^2 - 18x + 5)^2 = 0 \tag{6}$$

An extension of (3) and (4) respectively, was given by Ravichandran *et al.* [21] as follows:

$$S^*(\gamma, \varphi) = \left\{ f \in \mathcal{A}: 1 + \frac{1}{\gamma}\left(\frac{zf'(z)}{f(z)} - 1 \right) \prec \varphi(z) \right\} \tag{7}$$

$$C(\gamma, \varphi) = \left\{ f \in \mathcal{A}: 1 + \frac{1}{\gamma}\left(\frac{zf''(z)}{f'(z)} \right) \prec \varphi(z) \right\} \tag{8}$$

where, $\gamma \in \mathbb{C} \setminus \{0\}$.

These particular forms of functions are known as Ma–Minda type analytic functions of order γ, $(\gamma \in \mathbb{C} \setminus \{0\})$.

Recently, Al-Shaikh *et al.* [22] introduced the class $\mathcal{R}(l, m, \propto, \gamma)$, where $0 \leq \propto \leq 1$ and $\gamma \in \mathbb{C} \setminus \{0\}$, consisting of analytic functions $f \in \mathcal{A}$ of complex order γ, satisfying the subordination condition:

$$1 + \frac{1}{\gamma}\left(\frac{zf'(z) + \propto z^2 f''(z)}{(1-\propto)f(z) + \propto zf'(z)} - 1 \right) \prec \varphi_{Car}(l, m; z)$$

where, $\varphi_{Car}(l, m; z)$ defines a cardioid domain given by:

$$\varphi_{Car}(l, m; z) = \frac{2l\tau^2 z^2 + (l-1)\tau z + 2}{2m\tau^2 z^2 + (m-1)\tau z + 2}$$

with $-1 < m < l \leq 1$, $\tau = \frac{1-\sqrt{5}}{2}$, and $z \in \mathbb{E}$. For more details, see [9].

2. PROPOSED WORK

Inspired by the concept of cardioid region studied by Kumar and Kamaljeet [19] and Al-Shaikh *et al.* [22], we consider the class $\mathcal{A}(w)$ consists of analytic functions of the form:

$$f(z) = (z - w) + \sum_{n=2}^{\infty} a_n (z - w)^n \tag{9}$$

normalized by the conditions $f(w) = 0$, $f'(w) = 1$, where w is a fixed point, investigated by Kanas and Ronning [23]. Based on these ideas, we now introduce the following new subclass of analytic functions of complex order γ.

Definition 1. A function $f(z) \in \mathcal{A}(w)$ of the form (9) is said to be in the class $\mathfrak{R}_{Car}(\gamma, \propto, w; z)$ of analytic functions of complex order γ provided that the following conditions hold:

$$1 + \frac{1}{\gamma}\left\{ \frac{(z-w)f'(z) + \propto (z-w)^2 f''(z)}{(1-\propto)f(z) + \propto (z-w)f'(z)} - 1 \right\} \prec \varphi_c(z),$$

where, $0 \leq \propto \leq 1$ and $\gamma \in \mathbb{C}\setminus\{0\}$ and $\varphi_c(z)$ is given by:

$$\varphi_c(z) = 1 + (z - w)e^{(z-w)};\ (z \in \mathbb{E}) \tag{10}$$

By selecting particular values for the parameters $\gamma, \propto$ and w in Definition 1, we obtain a known subclass and some new subclasses as special cases.

(i) $\Re_{Car}(\gamma, 0, w; z) \equiv \mathcal{S}^*_{Car}(\gamma, w; z)$: A new subclass of starlike functions characterized by a complex parameter γ, involving the cardioid domain.

(ii) $\Re_{Car}(1{,}0{,}0; z) \equiv \mathfrak{S}^*_{\wp}$: Subclass of starlike functions connected with cardiod domain, introduced by Kumar and Kamaljeet [19].

(iii) $\Re_{Car}(\gamma, 1, w; z) \equiv \mathcal{C}_{Car}(\gamma, w; z)$: A new subclass of convex functions of complex γ associated with cardioid domain

(iv) $\Re_{Car}(1{,}1, w; z) \equiv \mathcal{C}_{Car}(w; z)$: A new subclass of w −convex functions connected to the cardioid domain.

3. SET OF LEMMAS

We make use of the lemmas stated below to derive our main results:

Lemma 1. If $p \in \mathcal{P}$ and it has the form (2), then

$$|c_n| \leq 2\, for\ n \geq 1, \tag{11}$$

Furthermore, for any $v \in \mathbb{C}$,

$$\left|c_2 - vc_1^2\right| \leq 2\, max\{1,\ |2v - 1|\} \tag{12}$$

For the inequality in (11), see [4], while the inequality in (12) was reported by Keogh and Merkes [24].

For the purpose of obtaining our primary results, it is necessary to prove the following lemma:

Lemma 2. Let $p(z) = 1 + c_1(z - w) + c_2(z - w)^2 + \cdots$, and $p(z) \prec \varphi_c(z)$, where φ_c is given by (10), then

$$|p_1| \leq 1,\ \ |p_2| \leq 1\ and\ |p_3| \leq \frac{1}{2}$$

Results are sharp.

Proof. If $p(z) \prec \varphi_c(z)$, then there exists an analytic function $u(z)$ such that $|u(z)| \leq |z|$ in $\mathbb{E}$ and $p(z) = \varphi_c(u(z))$. Therefore, the function:

$$h(z) = \frac{1 + u(z)}{1 - u(z)}$$

$$= 1 + c_1(z - w) + c_2(z - w)^2 + c_3(z - w)^3 + \cdots,$$

is in the class $\mathcal{P}(0)$. It follows that

$$u(z) = \frac{c_1(z - w)}{2} + \left(c_2 - \frac{c_1^2}{2}\right)\frac{(z - w)^2}{2}$$
$$+\left(c_3 - c_1c_2 + \frac{c_1^3}{4}\right)\frac{(z - w)^3}{2} + \cdots,$$

therefore,

$$\varphi_c\big(u(z)\big) = 1 + u(z)e^{u(z)}.$$

Based on the series expansion of $u(z)$ and elementary computations, we have

$$\varphi_c\big(u(z)\big) = 1 + \frac{c_1}{2}(z - w) + \frac{c_2}{2}(z - w)^2$$
$$+\left(-\frac{c_1^3}{16} + \frac{c_3}{2}\right)(z - w)^3 + \left(\frac{c_1^4}{24} - \frac{3c_1^2c_2}{16} + \frac{c_4}{2}\right)$$
$$(z - w)^4 + \cdots$$
$$= 1 + p_1(z - w) + p_2(z - w)^2 + p_3(z - w)^3$$
$$+p_4(z - w)^4 \ldots$$

Equating coefficients, we get:

$$p_1 = \frac{c_1}{2} \tag{13}$$

$$p_2 = \frac{c_2}{2} \tag{14}$$

and

$$p_3 = \left(-\frac{c_1^3}{16} + \frac{c_3}{2}\right) \tag{15}$$

The desired results can be obtained by applying Lemma $1(11)$ to equations $(13) - (15)$.

4. MAIN RESULTS

In this section, we determine the best possible bounds for the initial three coefficients and provide sharp estimates of the Fekete-Szegö inequality for the functions $f \in \Re_{Car}(\gamma, \propto, w; z)$. Moreover, to emphasize the connection between prior research and the new contributions, the well-known class is also highlighted.

Theorem 1. Let $f \in \Re_{Car}(\gamma, \propto, w; z)$, and be given by (9). Then,

$$|a_2| \le \frac{\gamma}{(1+\propto)}, \qquad |a_3| \le \frac{\gamma(1+\gamma)}{2(1+2\propto)}$$

$$and \quad |a_4| \le \frac{\gamma(\gamma^2+3\gamma+1)}{6(1+\propto)}.$$

These findings are sharp.

Proof. For given $f \in \Re_{Car}(\gamma, \propto, w; z)$, define

$$p(z) = 1 + p_1(z-w) + p_2(z-w)^2 + p_3(z-w)^3 + \cdots,$$

by

$$1 + \frac{1}{\gamma}\left\{\frac{(z-w)f'(z) + \propto (z-w)^2 f''(z)}{(1-\propto)f(z) + \propto (z-w)f'(z)} - 1\right\} = p(z),$$

where $p(z) \prec \varphi_c(z)$ in $\mathbb{E}$, and is given by (10). Hence,

$$1 + \frac{1}{\gamma}\left\{\frac{(z-w)f'(z) + \propto (z-w)^2 f''(z)}{(1-\propto)f(z) + \propto (z-w)f'(z)} - 1\right\}$$

$$= 1 + \frac{(1+\propto)a_2}{\gamma}(z-w)$$

$$+ \frac{(2(1+2\propto)a_3 - (1+\propto)^2 a_2^2)}{\gamma}(z-w)^2$$

$$+ \frac{(3(1+\propto)a_4 - 3(1+\propto)(1+2\propto)a_2a_3 + (1+\propto)^3 a_2^3)}{\gamma}(z-w)^3 + \cdots$$

$$= 1 + p_1(z-w) + p_2(z-w)^2 + p_3(z-w)^3 + \cdots.$$

Equating coefficients of $(z-w)$, $(z-w)^2$, and $(z-w)^3$ we get:

$$a_2 = \frac{\gamma}{(1+\propto)} p_1 \tag{16}$$

$$a_3 = \frac{\gamma}{2(1+2\propto)} p_2 + \frac{\gamma^2}{2(1+2\propto)} p_1^2 \tag{17}$$

and

$$a_4 = \frac{\gamma}{3(1+\propto)} p_3 + \frac{\gamma^2}{2(1+\propto)} p_1 p_2 + \frac{\gamma^3}{6(1+\propto)} p_1^3 \tag{18}$$

By employing Lemma 2 on Equations (16) – (18), the required results are obtained. The function:

$$\mathfrak{H}_1(z) = z\, exp(e^z - 1) \tag{19}$$

plays the role of an extremal function when $\gamma = 1$ and $w = \propto = 0$, for which the equality holds.

Remark 1. For $w = 0, \gamma = 1$ and $\propto = 0$ in Theorem 1, we get the following known result, investigated by Kumar and Kamaljeet [19].

Theorem 2. If $f \in \mathfrak{S}_p^*$ and has the form $f(z) = z + \sum_{k=2}^{\infty} a_k z^k$, then

$$|a_2| \le 1, \qquad |a_3| \le 1 \; and \; |a_4| \le \frac{5}{6}$$

These bounds are sharp.

Remark 2. For $\propto = 0$ in Theorem 1, we obtain the following new result for the subclass $\mathcal{S}^*_{Car}(\gamma, w; z)$.

Theorem 3. Let $f \in \mathcal{S}^*_{Car}(\gamma, w; z)$, where f is given by (9), then

$$|a_3| \le \frac{\gamma(1+\gamma)}{2},$$

$$|a_4| \le \frac{\gamma(\gamma^2+3\gamma+1)}{6}.$$

Remark 3. When $\propto = 1$, Theorem 1 reduces to the following new result for the subclass $\mathcal{C}_{Car}(\gamma, w; z)$.

Theorem 4. If $f \in \mathcal{C}_{Car}(\gamma, w; z)$ and is of the form (9), then

$$|a_2| \le \frac{\gamma}{2},$$

$$|a_3| \le \frac{\gamma(1+\gamma)}{6},$$

and

$$|a_4| \le \frac{\gamma(\gamma^2+3\gamma+1)}{12}.$$

Remark 4. When $\gamma = 1$ and $\propto = 1$, Theorem 1 leads to the following new result for the subclass $\mathcal{C}_{Car}(w; z)$, as follows.

Theorem 5. Let $f \in \mathcal{C}_{Car}(w; z)$, where f is given by (9), then

$$|a_2| \le \frac{1}{2}, \; |a_3| \le \frac{1}{3}, \; and \; |a_4| \le \frac{5}{12}.$$

Next, we turn our attention to the Fekete-Szegö problem for the subclass $\Re_{Car}(\gamma, \propto, w; z)$.

Theorem 6. If a function f of the form (9) belongs to $\mathfrak{R}_{Car}(\gamma,\propto,w;z)$, then

$$|a_3-\lambda a_2^2| \leq$$

$$\frac{|\gamma|}{2(1+\propto)}\, max\left\{1, \left|\frac{2\gamma\lambda(1+2\propto)-(\gamma+1)(1+\propto)^2}{(1+\propto)^2}\right|\right\}$$

This result is sharp.

Proof. If $f \in \mathfrak{R}_{Car}(\gamma,\propto,w;z)$, then from (13) and (16), we get

$$a_2 = \frac{\gamma c_1}{2(1+\propto)}\,.$$

Also, from $(13)-(14)$ and (17), we have

$$a_3 = \frac{\gamma c_2}{4(1+2\propto)} + \frac{\gamma^2 c_1^2}{8(1+2\propto)}.$$

This implies that

$$a_3-\lambda a_2^2 =$$

$$\frac{\gamma}{4(1+2\propto)}\left\{c_2 - c_1^2\left(\frac{2\gamma\lambda(1+2\propto)-\gamma(1+\propto)^2}{2(1+\propto)^2}\right)\right\}$$

Let,

$$v = \left(\frac{2\gamma\lambda(1+2\propto)-\gamma(1+\propto)^2}{2(1+\propto)^2}\right)$$

This leads to:

$$|a_3-\lambda a_2^2| = \frac{|\gamma|}{4(1+2\propto)}|c_2 - v c_1^2|$$

Applying lemma 1(12) for v, We obtained the required result. For $\gamma = 1$ and $w = \propto = 0$, equality cases hold for the function given by (1) when $\lambda \in \left[\frac{1}{2},\frac{2}{3}\right]$, and for $\mathfrak{H}_2(z) = z\, exp\left(\frac{e^z-1}{2}\right)$ when $\lambda \leq \frac{1}{2}$ or $\lambda \geq \frac{2}{3}$. These are special cases of the general function $\mathfrak{H}_n(z) = z\, exp\left(\frac{e^{z^n}-1}{n}\right)$.

Remark 5. For $\gamma = 1$ and $\propto = w = 0$ in Theorem 6, we obtain the known result for the subclass $\mathfrak{S}_{\mathcal{P}}^*$, investigated by Kumar and Kamaljeet [19].

Theorem 7. If a function f of the form (1) belongs to $\mathfrak{S}_{\mathcal{P}}^*$, then

$$|a_3-\lambda a_2^2| = \frac{1}{4}\left|c_2-\left(\lambda-\frac{1}{2}\right)c_1^2\right| \leq \frac{1}{2} max(1,2|\lambda-1|).$$

The function for which equality holds is given by (19). In particular, for $\lambda = 1$, we have:

$$|a_3-a_2^2| \leq \frac{1}{2}.$$

Remark 6. For $\propto = 0$ in Theorem 6, we obtain the following new result for the subclass $\mathcal{S}_{Car}^*(\gamma,w;z)$.

Theorem 8. If a function f of the form (9) belongs to $\mathcal{S}_{Car}^*(\gamma,w;z)$, then

$$|a_3-\lambda a_2^2| \leq \frac{|\gamma|}{2}\, max\{1, |\gamma(2\lambda-1)-1|\}$$

This result is sharp.

Remark 7. The following new result for the subclass $\mathcal{C}_{Car}(\gamma,w;z)$ is obtained by taking $\propto = 1$ in Theorem 6.

Theorem 9. Let $f \in \mathcal{C}_{Car}(\gamma,w;z)$ and be of the form (9). Then

$$|a_3-\lambda a_2^2| \leq \frac{|\gamma|}{6}\, max\left\{1, \left|\frac{\gamma(3\lambda-4)-4}{4}\right|\right\}$$

Remark 8. The new result for the subclass $\mathcal{C}_{Car}(w;z)$ is obtained by setting $\gamma = 1$ and $\propto = 1$ in Theorem 6, as follows:

Theorem 10. Let $f \in \mathcal{C}_{Car}(w;z)$ be given (9). Then,

$$|a_3-\lambda a_2^2| \leq \frac{1}{6}\, max\left\{1, \left|\frac{3\lambda-4}{2}\right|\right\}$$

5. CONCLUSIONS

In the present work, we introduce a new Ma–Minda type subclass $\mathfrak{R}_{Car}(\gamma,\propto,w;z)$ of univalent functions. Furthermore, by assigning specific values to the parameters γ, $\propto$ and w, we define three additional subclasses: $\mathcal{S}_{Car}^*(\gamma,w;z)$ and $\mathcal{C}_{Car}(\gamma,w;z)$, $\mathcal{C}_{Car}(w)$, corresponding to starlike and convex functions, respectively. These subclasses are introduced in connection with the concepts of subordination and the cardioid domain. The fundamental geometric properties of these subclasses were investigated, including sharp bounds for the first three coefficients and sharp estimates for the Fekete–Szegö problem. Moreover, a well-known class and its associated results have been identified to demonstrate the connection between earlier work and the present investigation.

6. CONFLICT OF INTEREST

The authors declare that they have no conflict of interest.

7. REFERENCES

1. C. Tom (Ed.). Univalent Functions: The Basics (Chapter 8). In: Geometric Function Theory. *Springer, Cham, Switzerland* pp. 203-225 (2024).
2. A.W. Goodman (Ed.). Univalent functions. Vol. I. *Mariner Publishing Company* (1983).
3. A.W. Goodman (Ed.). Univalent functions. Vol. II. *Mariner Publishing Company* (1983).
4. C. Pommerenke (Ed.). Univalent Functions. *Vandenhoeck and Ruprecht, Göttingen* (1975).
5. D.K. Thomas, N. Tuneski, and A. Vasudevarao (Eds.). Univalent functions. Part of: De Gruyter Studies in Mathematics. *De Gruyter, Berlin* (2018).
6. P.L. Duren (Ed.). Univalent functions. Part of the book series: Grundlehren der mathematischen Wissenschaften (Volume 259). *Springer-Verlag, New York* (1983).
7. N.E. Cho, V. Kumar, and V. Ravichandran. A survey on coefficient estimates for Caratheodory functions. *Applied Mathematics E-Notes* 19: 370-396 (2019).
8. V. Kumar, N.E. Cho, V. Ravichandran, and H.M. Srivastava. Sharp coefficient bounds for starlike functions associated with the Bell numbers. *Mathematica Slovaca* 69(5): 1053-1064 (2019).
9. Y.J. Sun, M. Arif, L. Shi, and M.I. Faisal. Some further coefficient bounds on a new subclass of analytic functions. *Mathematics* 11(12): 2784 (2023).
10. M. Fekete and G. Szegö. Eine Bemerkung uber ungerade schlichte Funktionen. *Journal of the London Mathematical Society* 8: 85-89 (1933).
11. S. Kanas and H.E. Darwish. Fekete-Szegö problem for starlike and convex functions of complex order. *Applied Mathematics Letters* 23: 777-782 (2010).
12. A. Ahmed, A.W. Shaikh, and S.A. Shah. Fekete-Szegö Problem for Certain Analytic Functions of Complex Order Associated with Cardioid Domain. *International Journal of Analysis and Applications* 23: 109-109 (2025).
13. W. Ma and D. Minda. A unified treatment of some special classes of functions. In: Proceedings of the Conference on Complex Analysis. *Nankai Institute of Mathematics, Nankai University, Tianjin, China* pp. 157-169 (1992).
14. W. Janowski. Some extremal problems for certain families of analytic functions I. *Annales Polonici Mathematici* 28(3): 297-326 (1973).
15. M.S. Robertson. On the theory of univalent functions. *Annals of Mathematics* 37(2): 374-408 (1936).
16. N.E. Cho, V. Kumar, S.S. Kumar, and V. Ravichandran. Radius problems for starlike functions associated with the sine function. *Bulletin of the Iranian Mathematical Society* 45: 213-232 (2019).
17. M.K. Aouf, J. Dziok, and J. Sokol. On a subclass of strongly starlike functions. *Applied Mathematics Letters* 24(1): 27-32 (2011).
18. J. Sokoł and J. Stankiewicz. Radius of convexity of some subclasses of strongly starlike functions. *Zeszyty Naukowe Politechniki Rzeszowskiej Matematyka* 19: 101-105 (1996).
19. S.S. Kumar and G. Kamaljeet. A cardioid domain and starlike functions. *Analysis and Mathematical Physics* 11(2): 34 (2021).
20. K. Sharma, N.K. Jain, and V. Ravichandran. Starlike functions associated with a cardioid. *Afrika Matematika* 27: 923-939 (2016).
21. V. Ravichandran, P. Yasar, B. Metin, and S. Arzu. Certain subclasses of starlike and convex functions of complex order. *Hacettepe Journal of Mathematics and Statistics* 34: 9-15 (2005).
22. S.B. Al-Shaikh, K. Matarneh, A.A. Abubaker, and M.F. Khan. Sharp Coefficient Bounds for a New Subclass of Starlike Functions of Complex Order γ Associated with Cardioid Domain. *Mathematics* 11(9): 2017 (2023).
23. S. Kanas and F. Ronning. Uniformly starlike and convex functions and other related classes of univalent functions. *Annales Universitatis Mariae Curie-Skłodowska. Sectio A* 53: 95-105 (1999).
24. F.R. Keogh and E.P. Merkes. A coefficient inequality for certain classes of analytic functions. *Proceedings of the American Mathematical Society* 20: 8-12 (1969).

Proceedings of the Pakistan Academy of Sciences: A
Physical and Computational Sciences 62(2): 137-148 (2025)

ISSN (Print): 2518-4245; ISSN (Online): 2518-4253
http://doi.org/10.53560/PPASA(62-2)694

Pakistan Academy of Sciences

Research Article

Transformer Based Essay Generation and Automatic Evaluation Framework

Israr Hanif[1], Zoha Latif[1], Fareeha Shafique[1], Humaira Afzal[1],
and Muhammad Rafiq Mufti[2*]

[1]Department of Computer Science, Bahauddin Zakariya University, Multan, Pakistan
[2] Department of Computer Science, COMSATS University Islamabad,
Vehari Campus, Vehari, Pakistan

Abstract: The purpose of Automated Essay Grading (AEG) systems is to evaluate and assign grades to essays efficiently, thereby reducing manual effort, time, and cost. The traditional AEG system mainly focuses its efforts on extractive evaluation rather than abstractive evaluation. The objective of this research is to explore the differences in the grading system of traditional and grammar schools. This research develops a transformer-based system that combines extractive and abstractive essay generation and evaluation. We utilize the Bidirectional Encoder Representations from Transformers (BERT) model for extractive essay generation and Quillbot for abstractive paraphrasing, and design a framework that evaluates both types of essays. To achieve this objective, we created the Long Essay Poets (LEP) dataset and evaluated this across four modes using four models. We compare the performance of four models: Random Forest, Convolutional Neural Network (CNN), Long Short-Term Memory (LSTM), and a combined approach of CNN and LSTM. After performing the experiment, it is concluded that 46% of grades declined in Mode 3 and 44% of grades improved in Mode 4, and in the context of essay evaluation, the Random Forest model performs better in extractive and merging scenarios, and the Long Short-Term Memory (LSTM) Model outperforms in abstractive essay evaluation.

Keywords: Transformer, Essay Generation, BERT Model, Natural Language Processing, Automatic Essay Grading.

1. INTRODUCTION

Automated Essay Grading (AEG) systems are designed to evaluate the quality of written text. The term Essay is defined as well-organized text written about a specific topic. The study in this domain started in 1966 and is still an active research domain. The first AEG system known as the Project Essay Grader (PEG) system is designed to assign grades based on different features including sentence structure, dictation, and grammatical mistakes [1]. The advancement in Natural Language Processing (NLP) made a greater contribution toward the generation and assessment of these essays using text-based features. Continuous effort has been made to design a fair and reliable evaluation systems which help in reducing manual labor, save time and lessen bias. These AEG systems are comprised of numerous domains that involve Education, NLP, and Linguistics and are used to assign grades based on certain features. The advent of transformers had a significant impact on the generation and evaluation of text. The self-attention mechanism utilized by the transformer model addresses complex challenges such as machine translation, short-answer questioning and sentimental analysis. Transformers are renowned for handling long-term dependency in a text comprising of two parts: 1) encoder, and 2) decoder. The encoder utilized a self-attention mechanism that gives weight to each word. The decoder also implements this mechanism to generate an output token and assures the relevancy of the output sequence. Parallel computation, capturing the context of text, and maintaining the connection of sentences to generate meaningful

---

Received: April 2025; Revised: May 2025; Accepted: June 2025
* Corresponding Author: Muhammad Rafiq Mufti <rafiq_mufti@ciitvehari.edu.pk>

output made transformers more powerful and useful in the domain of NLP [2]. Transformer models are trained on huge corpus and are capable of solving complex problems. These models include Generative Pre-Trained Transformer (GPT), Bidirectional and Auto-Regressive Transformers (BART) and Bidirectional Encoder Representations from Transformers (BERT). BERT was introduced by Google AI and is trained on internet raw text as well as Wikipedia text and different versions of GPTs are presented by Open AI and it has 175 billion parameters that generate text creatively [3]. BART, on the other hand, mostly used for summarization tasks [4]. These models generate text but the nature of the generated text varies between the two types. One is abstractive and the other is extractive. In abstractive generation, the model generates the text from input text but it generates the text in their own-word keeping the context of the original text. It majorly focuses on important aspects of the entire text. On the other hand, extractive generation is used to extract text as it is without any modifications. These models worked in an extractive manner [5]. Mostly GPT is used for abstractive and the BERT model is used for extractive essay generation. The BERT model is known for Essay generation tasks and its bidirectional features help in understanding the context of sentences. The BERT model is notable for retaining the correlation of words in a sentence and having different sizes, parameters and layers [6]. The generated text is evaluated by two different ways. The first is exact, whereas the second is approximate. Exact evaluation means the written text is exactly matched with the referenced text or not. On the other hand, approximate evaluation is done when certain phrases and important words are matched with original text and it also uses own wording keeping the context of the referenced text in mind. This study aims to design a framework that evaluates both types of Essays. It also focuses on assessing the differences in the essay grading system of traditional and grammar school systems. For this, the Long Essay Poets (LEP) dataset is created. This dataset consists of both types of Essays having 100 instances and 8 features. To check the similarity of the referenced text with the generated text, we use different similarity measures that include Cosine similarity, Jaccard similarity, Longest-common sequence, and N-grams. The Essays are taken from Wikipedia, which is an open-source database that consists of articles. The essay is generated in response to the prompt. The majority of the research emphasizes a single type of Essay, which can be either abstractive or extractive. There is a scarcity of automatic evaluation systems that handle both types of Essays. For evaluation and assigning grades to Essays, different machine and deep learning algorithms will be implemented.

The first transformer model was introduced as a 'Fast weight controller' in the Early's 1990. Even though it captures association among words in a sentence, this model has some drawbacks and is not accepted worldwide [7]. Then Lu *et al.* [2] presented its model and named it transformer**,** defining the elements on which it depends. Its self-attention mechanism handled the biggest challenge in NLP by providing weightage to each word in a sentence and understanding its importance. This model helped in solving complex problems. One of the models known as BERT was introduced by Devlin *et al.* [6]. It is a pre-trained model based on Masked Language Model (MLM) and Next Sentence Prediction (NSP) making it a powerful model. The objective of MLM and NSP is to predict missing words in a sentence based on context. Apart from capturing sequence and connection in a sentence, BERT also captures contextual meanings in long sequence problem handling. Its vast application includes fine-tuning pre-trained models and parameter adjustment for text generation tasks. It also solves the challenges of text summarization, machine translation, and question answering [8]. Many researchers performed different experiments and generated Essays through the transformer BERT model. Qu *et al.* [9] used the BERT model and GPT-2 for text generation and automatic question-answering generation. This research presents a comparative study of these two models implemented on two large datasets named LLK and BaiduBaike having sizes of 848M and 5.3G. Analysis is performed to see the performance of these pre-trained models and it concludes that GTP-2 generates creative, novel and long sentences, whereas BERT model performs better in an extractive generation like in the case of question-answer generation. Another new approach presented by Chen *et al.* [10], is known as Conditional Masked Language Modeling (C-MLM) which fine-tunes the BERT model to generate more coherent text. This study provides a new dimension of the BERT model which is not only used for language understanding but also for generation task. IWSLT German-English and English-Vietnamese MT datasets are used in the experiment and this new approach outperforms generation tasks like machine translation and text summarization. The result shows that this approach generates a coherent and high quality that gives meaning properly. In another study of Essay generation, a new model was proposed by Lin *et al*. [11] called as PC-SAN model, which represents a Pretraining-Based Contextual Self- Attention Network. Topic Essay Generation used the PC-SAN model and generated high-quality essays that were informative and relevant to the topic. In the encoder layer, the BERT model is used to create Essays. It helps in maintaining the contextual and semantic meaning of sentences. Two Chinese corpus named ESSAY and ZhiHu are used to train the model. ZhiHu contains 50k training and 5k testing records and ESSAY comprises 300k training and 5k testing dataset. As an outcome, the PC-SAN model generates improved quality content and maintains topic consistency with the help of the BERT model. Another study conducted by Chan and Fan [12] for question generation was employed for a pre-trained BERT model. Two models were made by reconstructing the BERT model, in addition to utilizing the original BERT model. The BERT architecture consists of a multi-layer and bi-directional transformer. The three models developed were BERT-QG, BERT-SQG, and BERT-HLSQG. The SQuAD dataset is used for the training of the model. The BERT-HLSQG model performs well in question-generation tasks. Another goal of this study is to identify the difference between the original questions and the questions generated by the model which achieved higher performance on paragraph and sentence-level input. One of the language models is created known as AraGPT2 by Antoun *et al*. [13] for Arabic language. This study highlights the role of transformers in NLP and text generation, and also develops the N-grams language model (LM) which can handle a large corpus of text on the internet and 1.46b parameters of news and articles. A machine learning detector was also developed giving 98% accuracy. However, this model has some limitations as it can comprehended between human and machine written text.

On the other hand, evaluation is also an important and challenging task. The research started in 1960 and to date is an active and hot topic due to the presence of massive online courses, and many assignments are subjective based. So, one of the studies presents AES based on individual fairness which means 'similar people should get similar treatment' [14]. The dataset used for the AES system for individual fairness is the Automated Student Assessment Prize (ASAP). A total of 1569 responses from grade 7 students were collected each with 187 words. Sentence-BERT and LASER are used in this study instead of BOW and TF-IDF. The paraphrased Essay was analyzed for how well it maintains a similarity ranking. In terms of text representation, BERT and LASER are better and for scoring, gradient boosting is best according to this study. Another study presents short answer grading, a text-mining model proposed by Suzen *et al*. [15]. The distance between student response model sentences determines the completeness of the Essay. The important role is played by model vocabulary for both grading and feedback. A correlation of 0.81 is obtained from both responses. For the evaluation of automatic short answer scoring, the Kaggle short answer scoring dataset of approximately 10.000 is used [16]. This model is pre-trained on Word2Vec, Google news corpus, and Wikipedia dataset. Weightage is applied to each word in the first part and then word count, unique word, and average length are computed with statistical models. Quadratic Weighted Kappa (QWK) score of 0.78 is obtained from the random forest model and this model has application in diverse English and Science topics. An automated assessment system for the objective system can be easily developed to assess student-acquired knowledge but for the subjective system. It has limitations as it cannot compare correct answers semantically for automatic assessment and giving grades. To measure semantic similarity, an AG system was built by Hameed and Sadiq [17] in which input features like structural knowledge, and syntactical and sentence semantics were used in the Support Vector Machine (SVM) model to check similarity. This method's performance surpassed the previous methods having root means square error of 0.83 and Pearson's correlation coefficient of 0.63. Essay evaluation is not an easy task as it is time-consuming and several factors affect its accuracy. So, a new evaluation system was proposed by Ramamurthy, M. In this study, student written and reference text similarity is measured by the CS method and to generate document vector space, various methods are utilized. The dimensionality reduction technique is also used on document vector space along with new proposed synset-based word similarity model. The MSR paraphrase corpus and Li's benchmark datasets were used in this experiment. Kaggle short-answering dataset model performance is also evaluated [18].

For essay scoring, the merger of LSTM with transformer also presented by Johnsi and Kumar [32]. This study utilizes the sequential ability of the LSTM model with a transformer for an essay grading system. The ASAP-AES dataset is used in an experiment that contains 12k essays on eight different topics. To understand the context of long-generated essays and their relationships among words across sentences, the Bi-directional LSTM model is used with an attention pooling layer for generating vectors for each word. It uses a sigmoid function for classification and makes a comparison with other classification models. The evaluation metrics used in this study are the Mean Squared Error, which is used for checking regression quality, and QK for comparing scoring between humans and models. The combined approach yields a QWK of 0.86, and the model explicitly shows coherence and structure. Neural network approaches are also used in scoring Essays. Xia *et al.* [19] designed an automatic Essay scoring system. To get semantic and contextual meaning, the Bidirectional Long Short-term Memory (BLSTM) model is implemented on the ASAP dataset. The performance of different word embeddings was evaluated, and it was found out that Google Word2Vec was far better than standard Word2Vec method. It obtained a QWK score of 0.87, thus saving costs and minimizing the manual effort. The researcher emphasizes evaluating the answer to free-text questions. In order to address this, an intelligent auto-grading system has been designed. The BLSTM model is used to catch semantic meanings and create an attention layer to Essay to capture information correctly. The model is trained on the ASAP dataset available on Kaggle and focuses on critical words, avoiding unnecessary words, maintaining the logical semantics of sentences, and predicting grades. Skip-gram model is used as a word embedding and the Softmax function as an activation function to give weightage to each word and achieve a QWK score of 0.83 [20]. In another study, neural network architecture by using CNN and Long Short-Term Memory (LSTM) layer with word embedding as input, is designed by Riordan *et al.* [21] for evaluation of short answer scoring (SAS). A certain size of window features is extracted by the LSTM model and transferred to the aggregate layer, which chooses only accurate and crucial word windows. These models are applied to three different datasets named ASAP-SAS, Power-grading, and SRA dataset. The highest accuracy resulted in a QWK of 90%. Another unique concept of memory-augmented neural network is proposed for Essay evaluation. It comprises four layers. In these layers, the Essay is represented in vector form, assigned weights to words, and scored as output in the last output layer. Different models are implemented on the automated student assessment prize dataset and the best result is given by the LSTM+CNN model with an accuracy of 76% which is higher than previous studies [22]. Attention-based Essay scoring system is designed by Dong *et al.* [23] by using a combination of CNN+LSTM and the results showed that sentence level document model leads to be more effective in the case of long Essays. More importance is provided to the attention-based model by evaluating Essays. The output of layers is a sentence vector which assigns weights to each sentence and after the CNN layer, the attention layer of LSTM is attached to give scoring to each essay. The obtained results show that the model has an average QWK score of 0.764.

The contributions of this research work are as follows. A novel LEP dataset is formulated due to the absence of potential features and long Essays. Essay generation is done through transformer-based mode. A framework is designed that evaluates and assigns grades to both extractive and abstractive Essays. The aim is to explore the difference in grading system of the traditional and grammar school.

2. PROPOSED FRAMEWORK

The proposed framework is illustrated in Figure 1. This is the step-by-step approach for extractive and abstractive essay generation, and it applies different similarity metrics and implement different models for essay evaluation.

2.1. LEP Dataset

In the first stage of our study, we created a new dataset for solving the existing problems. Current datasets often have limitations, such as:

Short Texts: Unfortunately, most available datasets are made up of smaller text samples that are not

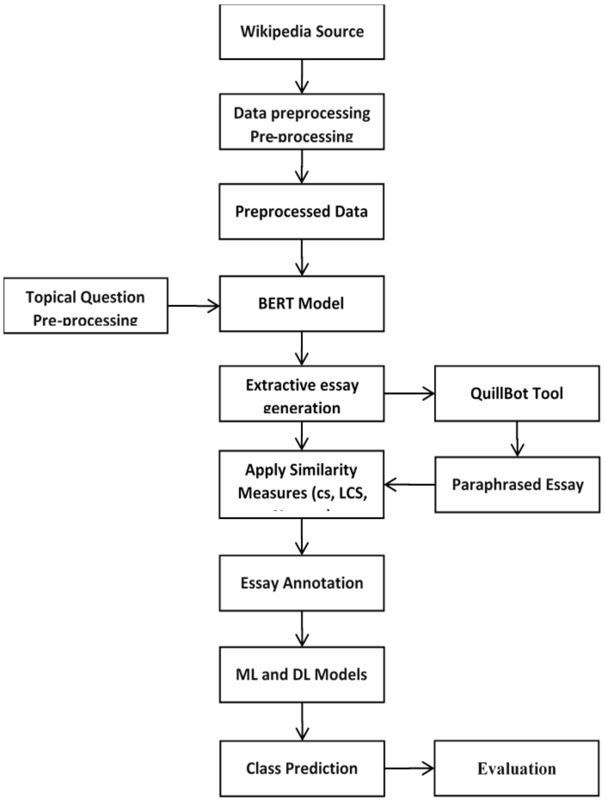

Fig. 1. Schematic presentation of proposed framework.

adequate for our purposes.

Language Barriers: Some datasets are collected in native languages and are not translated into English at all.

Feature Limitations: Many existing datasets are missing important features and do not contain both extractive and abstractive essays in one dataset.

In order to address these challenges and achieve the goals of the present research, we created a new dataset called the Long Essay Poets (LEP) Dataset. The source of the dataset is Wikipedia. As an open-source platform, Wikipedia provides a huge collection of articles of various domain and in various languages. It follows some structural guidelines and is written without discrimination of gender, religion, biasness, and religion. Wikipedia articles are reliable as one can check their validity by looking at the references and one can read talk links and discussion in case of wrong information was provided. The LEP dataset given in Table 1 has 8 features including id, Essay, question, answer, LCS, CS, N-Gram, and grade. Essays on Muslim

Table 1. Preview of LEP dataset.

ID	Essay	Question	Answer	LCS	CS	N gram	Grade
1	Syed Muhammad ibn Yousuf al-Hussaini (7 August 1321,10 November 1422), commonly known as Khwaja Banda Nawaz Gesudaraz, was a Hanafi Maturidi scholar and Sufi saint from India of the Chishti Order.Gaisu….	Write about Muhammad ibn Yousuf al-Hussaini?	In 10 November 1422, commonly known as khwaja banda nawaz gesudaraz, was a hanafi maturidi scholar and sufi saint…….	0.82	0.98	0.83	A
2	Ibrahim Qutb Shah Wali (1518 – 5 June 1580), also known by his Telugu names Malki BhaRama and Ibharama Cakravarti, was the fourth monarch of the kingdom of Golconda in southern India…….	Tell us about Ibrahim Qutb Shah Wali?	Raya. ibrahim is known for patronizing telugu extensively because he was moved by a genuine love for the language……	0.30	0.92	0.87	B
3	Khanzada Mirza Khan Abdul Rahim (17 December 1556 – 1 October 1627), popularly known as simply Rahim and titled Khan-i-Khanan, was a poet who lived in India during the rule of Mughal emperor Akbar……	Detail about Khan-i-Khanan?	Rahim was known for his hindustani dohe (couplets) and his books on astrology. abdul rahim was born in delhi, the son of bairam khan, akbars….	0.33	0.92	0.88	B+

poets are taken and we cover their background, education, their interests in poetry and details about written books. We named this feature of the dataset as ‘Essay’. In our data preprocessing steps, we removed citations by using the Chrome extension ‘Remove citation’. We also removed hyperlinks, and single and double quotes and eliminated other language words from the ‘Essay’ columns. The third column is about the question. Open-ended questions are raised against essays. Open-ended questions are those questions which are not specific but are generalized, and the answers are in detail-oriented manners. The next feature is answer which is either generated through the BERT model or paraphrased by using the paraphrasing tool. Different similarity metrics are utilized such as Cosine Similarity, Longest Common Subsequence, and N-Gram to calculate the similarity score and the last column is the ‘grade’ column. Grades are assigned based on predefined criteria set by our traditional and grammar school systems.

2.2. Extractive and Abstractive Essay Generation

For extractive essay generation, we used BERT, a transformer model that is currently one of the most sophisticated stances. The favourite feature of BERT is the understanding of context and the use of long-time dependencies in the sentence. To this end, we employed the BERT-base uncased model since it has relatively better performance and less computational overhead. In extractive essay generation, BERT understands the question, finds the coherent context of the answer within the referred Essay and returns the answers without any modification. For the abstractive Essay, we again used this generated Essay and rephrased it by using Quillbot. It changes the sentence structure from active to passive, gives synonyms, and rephrases the sentence while preserving the original meaning. We did this to see how the grading system of traditional and grammar schools is affected when we made certain changes in the answer. The Figure 2 depicts how BERT model works in extractive manner.

2.3. Similarity Metrics

Similarity metrics are used to measure the similarity between two sentences, paragraphs, and documents. In NLP, the most commonly used metrics are Cosine similarity, LCS, and N-Gram. Other forms of similarity matching algorithms are available but they cannot be used when matching short texts with long text. This is because our referenced answer is longer and the generated answer is not always equal in length to the referenced answer. So as a result, those metrics give too much lower scoring. Among the similarity metrics, we have Cosine similarity which is used to determine the angle of cosine between two vectors in the multi-dimensional space placing the text into the vector form before calculating the angle of similarity [24]. We have a higher score of similarity near to 1 when the angle of cosine is smaller. We also calculate the similarity score of the referenced essay with the generated essay using the longest common subsequence. It is used for the purpose of finding the longest segment between two sentences, based on sentence formation. The LCS is calculated by the total length of LCS to the geometric means of length of two sequences. The values closest to 1 are more similar and closest to 0 are less similar. The similarity score can be calculated by using N-gram feature. Thus N-gram contains n numbers of words in the sequence [25]. Using only one similarity metric is not suitable for all cases, therefore we combine Cosine, LCS, and N-Gram similarity into an average similarity score, and then have grades given depending upon the similarity score.

2.4. Traditional Grammar and School Grading System

The research work aims to identify the differences in the grading system of traditional and grammar schools. Our traditional school grading criteria are extractive in nature as higher similarity score would mean higher grade. On the other hand, grammar school obliged abstractive essays also. It also assigned higher grades if answer is relevant and is

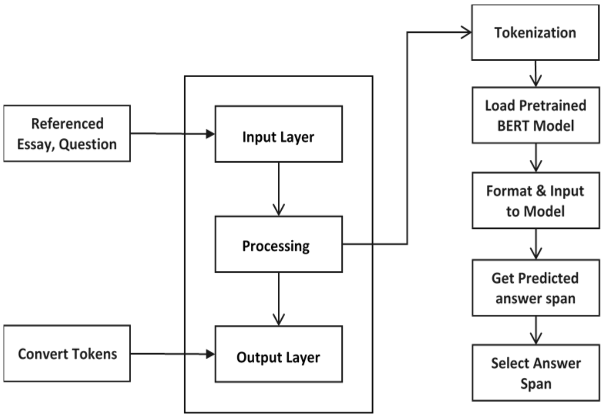

Fig. 2. Layout of the Essay generation through BERT.

from the given context although it is not exactly from the referenced essay. So, in our LEP dataset, the first 50 instances are generated from the BERT model in extractive manners and assigned grades based on predefined criteria set by the Punjab Board grading system and that is implemented in traditional schools. The last 50 rows are paraphrased by using Quillbot and thus assigned based on grammar school criteria given in Figure 3.

2.5. ML and DL Models for AGS

When output variable is categorical, the problem is said to be a classification problem. In the LEP dataset, labels or grades are already assigned. We implemented different models on the LEP dataset including random forest, CNN, LSTM and combined approach of CNN+LSTM.

2.5.1. Random forest model (RFM)

The RFM model is used to solve both classification and regression problems efficiently. During the training of the dataset, it makes multiple decision trees. By using the method of sampling with replacement, it makes a subset of the original dataset and hence solves the problem of overfitting. After making a subset and selecting important features, RFM model applies the ensemble technique of voting and gives predictions [26]. The experimental setup, including TfidfVectorizer() for word vectors and a train/test split, is 80/20 ratio. When RFM is implemented on LEP dataset, the following steps are followed:

- Data Preparation
- Feature Extraction (TF-IDF)
- Model Training
- Model Evaluation

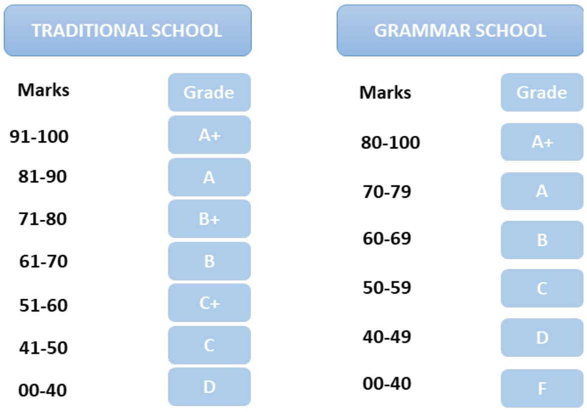

TRADITIONAL SCHOOL

Marks	Grade
91-100	A+
81-90	A
71-80	B+
61-70	B
51-60	C+
41-50	C
00-40	D

GRAMMAR SCHOOL

Marks	Grade
80-100	A+
70-79	A
60-69	B
50-59	C
40-49	D
00-40	F

Fig. 3. Schematic presentation of essay grading criteria.

2.5.2. Convolutional neural network (CNN) model

The CNN model outperforms in many NLP applications. It is useful in identifying patterns and making predictions. This model consists of layers including convolutional layer, max pooling along a fully connected layer. Different activation functions such as Relu and Softmax along layers are used to determine objects, sentimental analysis, and text classification [27].When CNN is implemented on LEP dataset , several steps are followed as:

Input data → Feature extraction → CNN processing
Numeric feature processing → Prediction

The experimental setup includes a dropout rate of 0.5 with ADAM optimizer, batch size 16 and 20 epochs with cross entropy loss function, having 20% testing and 80% training data.

2.5.3. Long short-term memory model (LSTM)

An advanced version of the recurrent neural network is LSTM which handles long-term association in a sentence and retain time series data in memory. The LSTM model eliminates the issue of overfitting and vanishing gradient that comes in the RNN model. There are three gates in the LSTM model. First is the input gate used to input text then the forget gate which is used to keep relevant and important information and discard irrelevant information and last one is the output gate which presents output. Through these gates, we can keep and erase information. The most used activation functions in the LSTM model are sigmoid and Tanh which help in resolving the issue of long-term dependency [28]. The LSTM model is implemented with two layers, each containing 128 units, and a dropout rate of 0.5. The model is trained using the ADAM optimizer with a learning rate of 0.0001, over 20 epochs and a batch size of 32.

2.6. Evaluation Metrics

The performance of ML and DL models is measured using evaluation metrics. These metrics show how well a model performs on the given datasets, allowing us to choose the best model through comparative analysis.

2.6.1. Accuracy

Total correctly predicted instances out of total instances is termed as accuracy. It counts overall correct prediction, regardless of any class. It also evaluates the effectiveness of the classification model [29].

$$Accuracy = \frac{TCP}{TI}$$

where, TCP denotes total correct predictions and TI is total instances.

2.6.2. Precision

Precision measures how many predictions that model predicts positive are actually positive. It focuses on the accuracy of positive predictions [29]. It is calculated as:

$$Precision = \frac{TP}{TP + FP}$$

where, TP represents true positive and FP denotes false positive.

2.6.3. Recall

Recall also known as sensitivity is calculated by identifying correctly positive instances out of the total instances of that class [29].

$$Recall = \frac{TP}{TP + FN}$$

where, FN represents false negative.

2.6.4. F1-score

F1-score is a balanced metric for both precision and recall. It is a harmonic mean of both metrics and is useful for uneven class distribution [29]. It is calculated as:

$$F1 - score = \frac{2}{1/precision \ + 1/recall}$$

3. RESULTS AND DISCUSSION

Four different models are implemented on the LEP dataset across four different modes. The analysis is divided into two parts: 1) Mode Setup, 2) Model-wise mode setup.

The LEP dataset is analyzed in four modes: 1) Evaluation of original instances in the context of Traditional School represented as Mode 1, 2) Evaluation of Paraphrased Instances in the context of Grammar School represented as Mode 2, 3) Merged instances in the context of the Traditional School represented as Mode 3, 4) Merged instances in the context of the Grammar School represented as Mode 4. The purpose of modes is to evaluate how the grades of abstractive and extractive essays are affected when grading criteria change. It also reflects the mindset of the examiner. In Mode 1, there are a total of 50 records. In these records, an answer column is generated from the BERT model, and grades are assigned based on traditional school criteria as given in Figure 3. There are also 50 records in Mode 2 in which the answer column is now rephrased by using Quillbot and assigned grades based on grammar school criteria. In Mode 3, there are a total of 100 records. In this mode, 50 records from the original and 50 records from paraphrased are combined and all these records are again evaluated on traditional school criteria. Similar to Mode 3, there are in 100 records in Mode 4 which are evaluated on grammar school criteria. As a result, 46% grades declined in Mode 3, and 44% grades improved in Mode 4. In all these modes, we calculate similarity scoring by using similarity metrics that are CS, LCS, and N-Gram. The values of similarity metric of Mode 1 are represented in Figure 4.

3.1. Model Wise Mode Evaluation

The Random Forest, CNN, LSTM and CNN + LSTM algorithms are applied on four different modes of LEP dataset.

3.1.1. RFM Evaluation

RFM Model is implemented by using four different modes and their performance is illustrated in Figure 5. Precision is higher as compared to accuracy F1-score and recall, which indicates good ability of the model to exclude almost all false positives. It means that our model carefully selected the features that are relevant to the context and thus improved precision. However, the recall is about 0.7, which suggests that some instances are not identified while accuracy and F1-score gives us a fair balanced performance [30]. With Mode 2, performance achieves much lower results in all metrics in comparison with Mode 1. According to the results measured by accuracy and precision, it is 0.4 and 0.15 respectively which shows a very poor performance and high imbalance toward

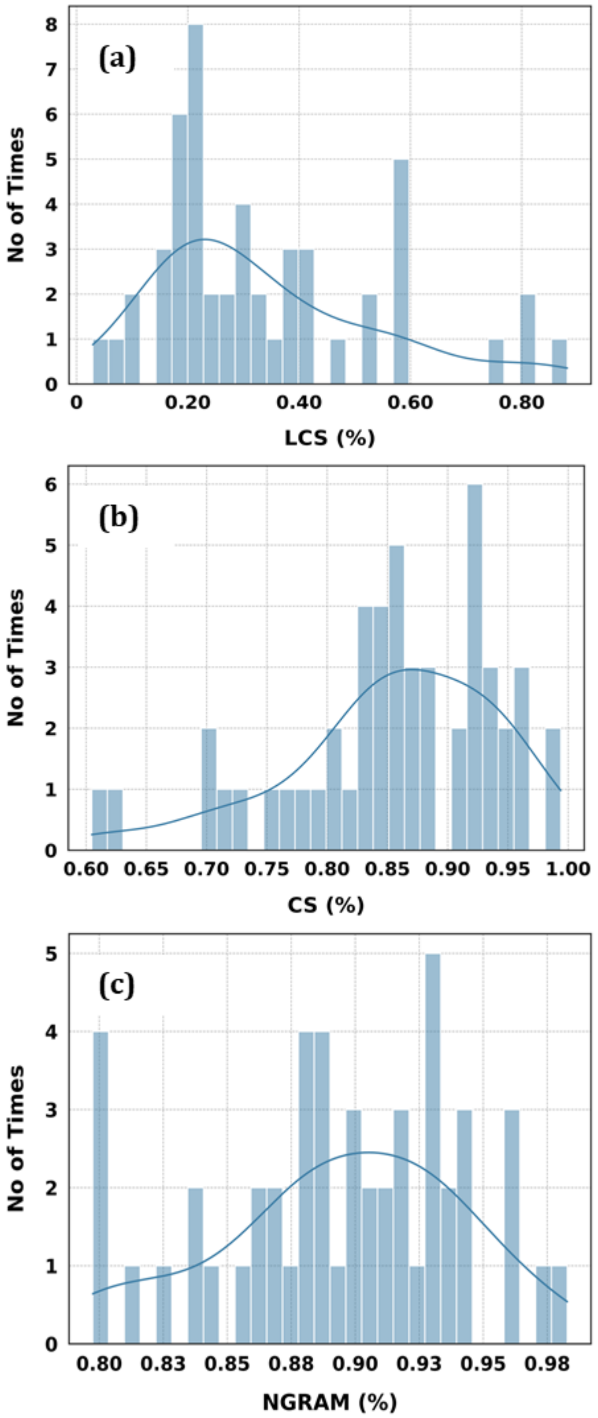

Fig. 4. Numeric features distribution: (a) LCS vs Number of Times, (b) CS vs Number of Times, and (c) Ngram vs Number of Times.

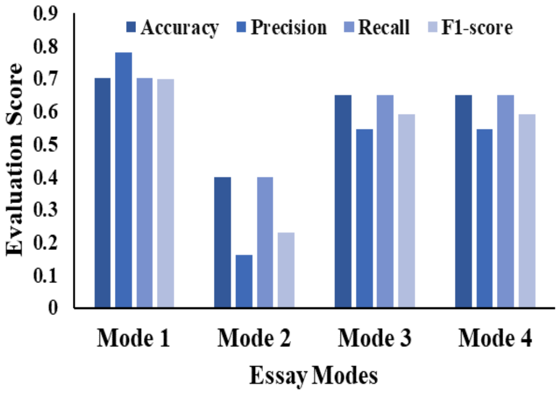

Fig. 5. RFM implementation by modes.

negative class. Recall is close to 0.4, which means moderate possibilities of identifying true positives only. As compared with Mode 2, performance increases significantly in Mode 3 and Mode 4. The accuracy gets to 0.65 which is the second best of all the modes. Precision and recall are 0.55 and 0.6, respectively, providing a better ratio of false positives per false negatives. We can therefore say that F1-score agrees with these values and thus it establishes balanced performance. From the results, it is evident that RFM performs well in Mode 1. It produces the best precision and moderate high accuracy as well as recall.

3.1.2. CNN Implementation

Table 2 show the performance of the convolutional neural network (CNN) in different modes. As for mode 1, CNN model demonstrates the highest specific accuracy and F1-score, which is the balanced measure of diversity that reflects both precision and recall. However, the moderate precision suggests the requirement to further decrease the number of false positives for increased accuracy. Unlike Mode 2, it was identified that the accuracy, precision, and F1-score were relatively lowest, implying the model had many false positive cases. Mode 3 and Mode 4 have very similar metrics, which are moderate accuracy and F1-

Table 2. Evaluation score through CNN.

S. No.	Mode	Accuracy	Precision	Recall	F1-score
1	Mode1	0.7	0.4899	0.7	0.5764
2	Mode2	0.4	0.16	0.4	0.2285
3	Mode3	0.5	0.25	0.5	0.3333
4	Mode4	0.5	0.25	0.5	0.3333

score, however, less precision indicates problem with reliability of predictions. From the results, it can be noted that the CNN model outperforms in Mode 1 it is because CNN is proficient in capturing local contextual patterns.

3.1.3. LSTM Outcome

The performance of a LSTM model is shown on all modes of the LEP dataset in Figure 6. According to Mode 1, the accuracy and the recall are greater than 0.4, this shows that its performance of correctly identifying positive cases is reasonably well. However, the less precision and F1-score indicating that the model has a tendency to generate a large number of false positives. On the other hand, Mode 2 exhibits the poorest performance, particularly in terms of precision and accuracy, due to its high misclassification rate and inability to efficiently capture positive cases. Mode 3 and Mode 4 have approximately the same accuracy and recall rates, even though the precision and F1 scores are somewhat lower; this means that there might be a small trade-off to the overall accuracy of the model regarding the management of the positive cases. Among them, Mode 3 is likely to be more balanced in such trade-offs and potentially more suitable for generalizing tasks.

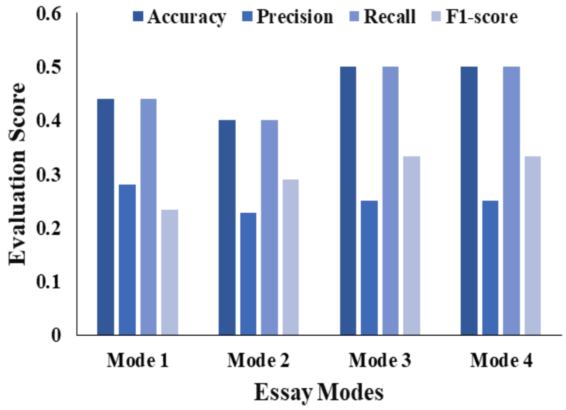

Fig. 6. LSTM outcome by Modes.

3.1.4. CNN + LSTM Implementation

The integration of CNN and LSTM architectures was proved to be efficient and provided very high performance in Mode 1. This is because the CNN model performs better in selecting the right contextual window span, while the LSTM model captures dependencies between sentences, which helps achieve higher accuracy compared to other models [31]. Table 3 shows a comprehensive picture of the model's performance across key evaluation parameters.

The final finding of our research is:

- By Performing mode analysis, it has been seen that 46% of grades are declined in Mode 3, and 44% of grades are improved in Mode 4.
- Among all models, the RFM model demonstrates better results on the LEP dataset.
- In the case of extractive essay evaluation and merging scenario, the RFM model gives higher accuracy, precision, and F1-score.
- The LSTM model outperformed other models in abstractive essay grading and achieved better results.
- Our proposed framework achieved higher accuracy in extractive essay grading as compared to abstractive.

4. CONCLUSIONS

The research work aims to design a framework that assigns grades on both types of essays and evaluate the difference in the grading system of traditional and grammar schools. To achieve the research objective, we designed the LEP dataset to generate essays through the BERT model and assigned grades based on predefined criteria. The performance of paraphrased essays is evaluated in traditional mode to measure how it affects the grade. The dataset is analyzed by four models across four modes and as a result RFM model achieved a higher accuracy of 70% in extractive essay and 65% in merging modes and the LSTM model achieved 40% in abstractive essay grading. In future work, we can enhance the

Table 3. Evaluation Score through CNN + LSTM.

S. No.	Mode	Accuracy	Precision	Recall	F1-score
1	Mode1	0.7	0.4899	0.7	0.5764
2	Mode2	0.4	0.16	0.4	0.2285
3	Mode3	0.5	0.25	0.5	0.3333
4	Mode4	0.5	0.25	0.5	0.3333

paraphrased part of the LEP dataset to achieve better performance in abstractive essay grading. We can also expand the scope of the LEP dataset by incorporating it into various domains.

5. CONFLICT OF INTEREST

The authors declare no conflict of interest.

6. REFERENCES

1. H.M. Alawadh, T. Meraj, L. Aldosari, and H.T. Rauf. An efficient text-mining framework of automatic essay grading using discourse macrostructural and statistical lexical features. *SAGE Open* 14(4): 1-14 (2024).
2. B.R. Lu, N. Haduong, C.Y. Lin, H. Cheng, N.A. Smith, and M. Ostendorf. Efficient encoder-decoder transformer decoding for decomposable tasks. *arXiv* 2403: 13112 (2024).
3. G. Yenduri, M. Ramalingam, G.C. Selvi, Y. Supriya, G. Srivastava, P.K. Maddikunta, G.D. Raj, R.H. Jhaveri, B. Prabadevi, W. Wang, and A.V. Vasilakos. GPT (generative pre-trained transformer) - a comprehensive review on enabling technologies, potential applications, emerging challenges, and future directions. *IEEE Access* 12: 54608-54649 (2024).
4. N. Delpisheh and Y. Chali. Improving faithfulness in abstractive text summarization with EDUs using BART (student abstract). *Proceedings of the AAAI Conference on Artificial Intelligence, (20th - 27th February, 2024), Vancouver, British Columbia, Canada* (2024).
5. W. Sun, C. Fang, Y. Chen, Q. Zhang, G. Tao, Y. You, T. Han, Y. Ge, Y. Hu, B. Luo, and Z. Chen. An extractive-and-abstractive framework for source code summarization. *ACM Transactions on Software Engineering and Methodology* 33(3): 75 (2024).
6. J. Devlin, M.W. Chang, K. Lee, and K. Toutanova. BERT: Pre-training of deep bidirectional transformers for language understanding. *Conference of the North American Chapter of the Association for Computational Linguistics: Human Language Technologies*, *(3rd - 5th June 2019), Minneapolis, Minnesota, USA* (2019).
7. I. Schlag, K. Irie, and J. Schmidhuber. Linear transformers are secretly fast weight programmers. *International Conference on Machine Learning, (18th - 24th July 2021), Vienna, Austria* (2021).
8. M.V. Koroteev. BERT: A review of applications in natural language processing and understanding. *arXiv* 2103: 11943 (2021).
9. Y. Qu, P. Liu, W. Song, L. Liu, and M. Cheng. A text generation and prediction system: pre-training on new corpora using BERT and GPT-2. *10th IEEE International Conference on Electronics Information and Emergency Communication, (17th-19th July 2020), Beijing, China* (2020).
10. Y.C. Chen, Z. Gan, Y. Cheng, J. Liu, and J. Liu. Distilling knowledge learned in BERT for text generation. *Proceedings of the 58th Annual Meeting of the Association for Computational Linguistics, (5th - 10th July 2020), Washington, USA* (2020).
11. F. Lin, X. Ma, Y. Chen, J. Zhou, and B. Liu. PC-SAN: Pretraining-based contextual self-attention model for topic essay generation. *KSII Transactions on Internet and Information Systems* 14(8): 3168-3186 (2020).
12. Y.H. Chan and Y.C. Fan. A recurrent BERT-based model for question generation. *Proceedings of the 2nd Workshop on Machine Reading for Question Answering, (4th November 2019), Hong Kong, China* (2019).
13. W. Antoun, F. Baly, and H. Hajj. AraGPT2: Pre-trained transformer for Arabic language generation. *6th Arabic Natural Language Processing Workshop, (19th April 2021), Kyiv, Ukraine* (2021).
14. A. Doewes, A. Saxena, Y. Pei, and M. Pechenizkiy. Individual fairness evaluation for automated essay scoring system. *15th International Conference on Educational Data Mining, (24th - 27th July 2022), Durham, United Kingdom* (2022).
15. N. Süzen, A.N. Gorban, J. Levesley, and E.M. Mirkes. Automatic short answer grading and feedback using text mining methods. *Procedia Computer Science* 169: 726-743 (2020).
16. A. Kumar, M. Sharma, and R. Singh. Automatic question-answer pair generation using deep learning. *3rd IEEE International Conference on Inventive Research in Computing Applications, (11th - 13th July 2021), Coimbatore, India* (2021).
17. N.H. Hameed and A.T. Sadiq. Automatic short answer grading system based on semantic networks and support vector machine. *Iraqi Journal of Science* 64(11): 6025-6040 (2023).
18. M. Ramamurthy and I. Krishnamurthi. Design and development of a framework for an automatic answer evaluation system based on similarity measures. *Journal of Intelligent Systems* 26(2): 243-262 (2017).
19. L. Xia, J. Liu, and Z. Zhang. Automatic essay scoring model based on two-layer bi-directional long-short term memory network. *3rd International Conference*

on Computer Science and Artificial Intelligence, (6th-8th December 2019), Beijing, China (2019).

20. Z. Wang, J. Liu, and R. Dong. Intelligent auto-grading system. *5th IEEE International Conference on Cloud Computing and Intelligence Systems, (23rd - 25th November 2018), Nanjing, China* (2018).
21. B. Riordan, A. Horbach, A. Cahill, T. Zesch, and C. Lee. Investigating neural architectures for short answer scoring. *12th Workshop on Innovative Use of NLP for Building Educational Applications, (8th September 2017), Copenhagen, Denmark* (2017).
22. S. Zhao, Y. Zhang, X. Xiong, A. Botelho, and N. Heffernan. A memory-augmented neural model for automated grading. *4th ACM Conference, L@S 2017, (20th - 21st April 2017), Cambridge, MA, USA* (2017).
23. F. Dong, Y. Zhang, and J. Yang. Attention-based recurrent convolutional neural network for automatic essay scoring. *21st Conference on Computational Natural Language Learning, (3rd - 4th August 2017), Vancouver, Canada* (2017).
24. S. Sheng, J. Jing, Z. Wang, and H. Zhang. Cosine similarity knowledge distillation for surface anomaly detection. *Scientific Reports* 14(1): 8150 (2024).
25. D. Jurafsky and J.H. Martin (Eds.). Speech and Language Processing: An Introduction to Natural Language Processing, Computational Linguistics, and Speech Recognition. 2nd Edition. *Prentice Hall*, *Pearson Education, India* (2000).
26. N. Jain and P.K. Jana. LRF: A logically randomized forest algorithm for classification and regression problems. *Expert Systems with Applications* 213(18): 119225 (2023).
27. M. Krichen. Convolutional neural networks: A survey. *Computers* 12(8): 151 (2023).
28. H. Alizadegan, B. Rashidi, A. Radmehr, H. Karimi, and M.A. Ilani. Comparative study of long short-term memory (LSTM), bidirectional LSTM, and traditional machine learning approaches for energy consumption prediction. *Energy Exploration & Exploitation* 43(1): 281-301 (2025).
29. A. Sbei, K. ElBedoui, and W. Barhoumi. Assessing the efficiency of transformer models with varying sizes for text classification: A study of rule-based annotation with DistilBERT and other transformers. *Vietnam Journal of Computer Science* 2024: 1-28 (2024).
30. H. Wang, Q. Liang, J.T. Hancock, and T.M. Khoshgoftaar. Feature selection strategies: a comparative analysis of SHAP-value and importance-based methods. *Journal of Big Data* 11: 44 (2024).
31. R. Nallapati, B. Zhou, C.N. dos Santos, Ç. Gülçehre, and B. Xiang. Abstractive text summarization using sequence-to-sequence RNNs and beyond. *arXiv:1602.06023* (2016).
32. R. Johnsi and G.B. Kumar. Enhancing automated essay scoring by leveraging LSTM networks with hyper-parameter tuned word embeddings and fine-tuned LLMs. *Engineering Research Express* 7(2): 025272 (2025).

Proceedings of the Pakistan Academy of Sciences: A
Physical and Computational Sciences 62(2): 149-164 (2025)

ISSN (Print): 2518-4245; ISSN (Online): 2518-4253
http://doi.org/10.53560/PPASA(62-2)879

Pakistan Academy of Sciences

Research Article

Granulometry based Extrapolation of Depositional Environment of Orangi Sandstone, Nari Formation Exposed around Hub Dam, Pakistan

Erum Bashir[1*], Sadia Khaleeq[2], Shahid Naseem[1], Maria Kaleem[1], Muhammad Shumail[2], and Wajih Ahmed[3]

[1]Department of Geology, University of Karachi, Karachi, Pakistan
[2]Department of Geology, Federal Urdu University of Arts, Science and Technology, Karachi, Pakistan
[3]Department of Geology, D.J. Sindh Govt. Science College, Karachi, Pakistan

Abstract: To infer the depositional environment, thirty-eight samples of the Orangi Sandstone-the uppermost unit of the Upper Oligocene Nari Formation, exposed at Hub Dam were collected. Granulometric data acquired from standard sieving techniques. The computed graphic mean's average value, was 1.38. Of the 38 samples, 24 were categorized as medium-grained, and the remaining 14 as coarse-grained. According to the sorting values, 36.84% of the samples were categorized as moderately sorted to moderately well-sorted, whereas 63.15% of the samples were poorly sorted. Skewness values showed a wide range from -2.17 to 2.65 suggesting a mixed population of coarse and fine skewed sediments. Kurtosis ranged from -2.46 to 2.97, showed situation of both leptokurtic and platykurtic. Bivariate plots created employing various textural parameters suggested predominantly fluvial origin with very few deviations. This interpretation is further supported by linear discriminant function analysis, which indicates a fluvial to shallow marine depositional setting for most samples. The study represents an initial attempt to appraise the vertical and lateral variability of the Orangi Sandstone using cement composition and textural parameters; skewness and kurtosis. The studied samples significantly reflect the impact of Upper Oligocene Period's tectonics, climate shift, and sea level fluctuations, and sediment transport dynamics. A model is constructed to describe the preponderant fluvial environment outlining the role of beach and tidal processes along with fluvial channels in the deposition of the sandstone.

Keywords: Granulometry, Depositional Model, Orangi Sandstone, Nari Formation, Hub Dam, Oligocene Age.

1. INTRODUCTION

Sandstones are formed by the lithification and cementation of sand-size particles [1]. Sandstones make up 10-20% of all rocks on the Earth and are extensively spread due to their tenacious character. Sandstones are significant from a variety of perspectives; they aid in comprehending the relief, topography, architecture, minerals, and chemical composition of any area; it is also beneficial for demonstrating the provenance and depositional patterns of a region [2-4]. In addition to being employed in construction and other industries [5], they host varieties of minerals [6], reservoirs of oil and gas [7] and are also serves as good aquifers too [8]. Inimitable genetic information and histories of depositional environments are naturally preserved in sandstones. Prime features that make up the texture of sandstone; particle size, sorting, and roundness are used to comprehend the conditions and processes that led to the deposition of the sediments [9]. To obtained textural parameters, granulometry is done by standard sieve analysis [2, 5]. The present study's region lies around Hub Dam, close to the Karachi trough. The Nari Formation (Oligocene to Early Miocene), which overlies the

---

Received: February 2025; Revised: May 2025; Accepted: June 2025
* Corresponding Author: Erum Bashir <ebahmed@yahoo.com>

Middle Eocene Kirthar Formation, is the oldest exposed formation [10]. The Nari Formation was formed in consequence of Himalayan orogeny, under tectonically unstable settings and underwent many periods of eustatic sea level changes. Five lithostratigraphic units are distinguished in the Nari Formation namely Orangi Sandstone is the youngest unit, followed by Pir Mangho, Halkani, Ghora Lakhi, and oldest Tobo unit respectively [8]. The Nari Formation's upper contact with the Gaj Formation is transitional and conformable [11].

Orangi Sandstone is the primary focus of the present study. This unit exhibits noticeable vertical and lateral facies variations, reflecting the dynamic interplay of tectonic activity, sediment supply, and marine transgressions during its deposition. The specific aims and objectives of this study are:

- To analyze the textural parameters (grain size, sorting, skewness, and kurtosis) of the Orangi Sandstone using statistical grain size analysis.
- To assess vertical and lateral facies variations in the study area and their relation to energy conditions and paleogeographic trends.
- To provide an interpretation of the depositional system, emphasizing the influence of hydrodynamic processes and tectonic settings during sedimentation.

By integrating grain size analysis with field observations of sedimentary structures like cross bedding, gradded bedding, ripple marks etc. and lithological variations, this research aims to enhance understanding of the paleodepositional settings and genetic evolution of the Orangi Sandstone within the broader framework of the Nari Formation. It may help to develop facies models in sedimentary basin analysis. This study may also assist for the reservoir quality prediction in hydrocarbons.

2. METHODOLOGY

2.1. Sample Collection

For the present study, 38 representative sandstone samples in a sequence from older to younger were collected from seven different sites. Considering the regional trend of the rocks, sampling was done from the outcrops of Orangi Sandstone exposed around and at the left bank of Hub Dam (Figure 1). Samples were collected in polyethylene bags to prevent loss of finer fractions, and then wrapped in towel to avoid physical damage during transportation to lab [12].

2.2. Sample Preparation

For size analysis, weakly cemented and friable sandstone samples were soaked in water, whereas the consolidated samples after crushing were soaked in 10% HCl solution for 24 hrs to remove cement from them [5]. Afterward, Whatman qualitative filter paper #1 was used to filter the sample. Using litmus paper, wash the sediment grains soaked in HCl many times until all the acid has been removed. First, the grains are adequately covered and dried at room temperature then in an electric oven. The samples were reduced in quantity and homogenized by applying coning and quartering method to obtain a representative sample [13].

2.3. Sample Analysis

Using a mechanical shaker (Model IL-60656 USA) and following the procedure described by [14], a 100-gram moisture-free sample was screened in an assembly of sieves (-1, 0, 1, 2, 3, 4 ϕ), pan and shaker. After shaking, each fraction was collected separately, weighed, and noted for further granulometry [15].

3. STUDY AREA

The research area is situated along the political border between Sindh and Balochistan provinces in the southwest of the Sindh Province. Its approximate boundaries are 25° 09′ to 25° 15′ N and 67° 02′ to 67° 12′ E (Figure 1); it's situated in the northwest of Karachi [16]. Tertiary rocks, particularly those from the Oligocene (Nari Formation) and Miocene (Gaj Formation) are exposed in the research area. These rocks were deposited over the Kirthar Formation due to the uplifting of the basin, after the Himalayan Orogeny [11].

The Nari Formation is deposited in two separate entities; the northern Nari Formation, which is exposed in the north of the study region from Dureji to Khuzdar, and the southern Nari Formation, which represents the Karachi Trough is exposed in the Lower Indus Basin [17]. Less thickness may be observed at the eastern and western edges of the Karachi Trough, whereas the northernmost portion has more thickness. The five

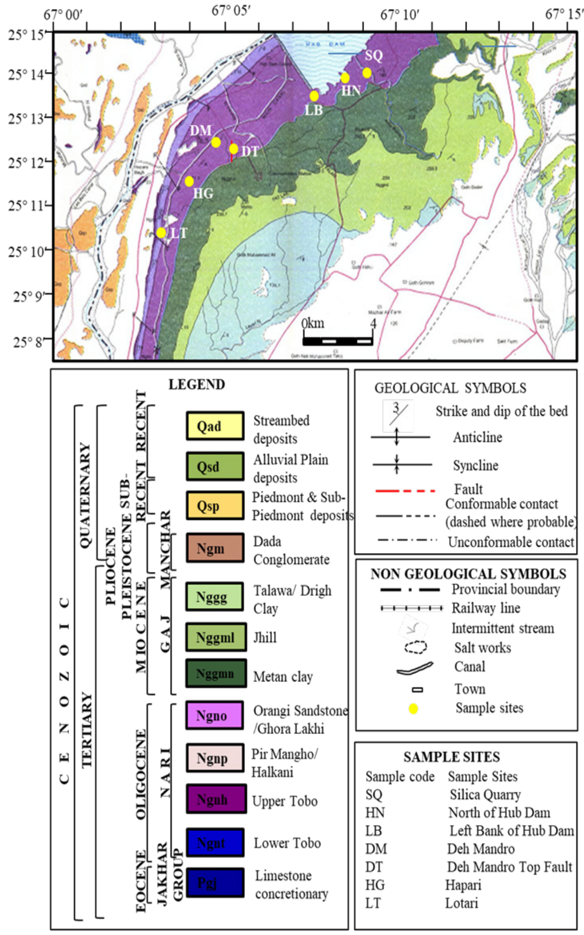

Fig. 1. Geological map of the study area showing sample sites, around Hub Dam after [16].

units of the Nari Formation include Tobo (oldest), Pir Mangho, Halkani, Ghora Lakhi, and youngest Orangi Sandstone [9, 16].

Orangi Sandstone is referred to as a variegated sequence due to the presence of yellow, brown, orange, violet, and red colours of cement; revealing the prevalence of varying levels of iron oxidation in the depositional system (Figure 2(a)). The siliceous cement is witnessed in the upper portion; it is often iron-free. Coarse-grained, even gritty layers are found at the top, whereas the bottom half is composed of fine-grained sandstone reflecting differences in the energy conditions of the depositional environment. Certain locations are extremely coarse grained and indicate channel depositional conditions. It has honeycomb structures, cross bedding, flute marks; grooves and ripple marks [18]. The Orangi Sandstone is devoid of fossils. There are also many neptunian dikes in some areas (Figure 2(b)).

Fig. 2. Field photographs showing: (a) colour variation in sandstone due to diversity of cement content, and (b) neptunian dyke in Orangi sandstone.

4. RESULTS

Table 1 displays the cumulative percentages of various fractions obtained from sieve analysis of studied samples. The weight percentages of the three main fractions (gravel, sand, and mud) of the samples are presented in Figure 3. Figure 4(a) displays general trends and location-wise sample cumulative curves of studied samples (Figure 4(b-h)). Most samples seem to be graded with varying degrees of gradation when compared to standard patterns. Table 2 and 3 exhibit calculated values, formulae, and categories of studied samples for the textural parameters. The graphic mean for the samples has an average value of 1.38 and a range of -0.02 to 2.72; while average value of standard deviation is 1.09 as mentioned in Table 2. Graphic skewness ranges between -2.17 to 2.65, with an average value of 0.10. Six of the Orangi Sandstone samples display strongly fine skewness, two show fine skewness, seven exhibits near symmetry, eight reveal coarse skewness, nine exhibit strongly coarse skewness, one sample has a value < -1.0, which appears as very strongly coarse skewed, and five samples have values > 1.0 and are classified as being very strongly fine skewed. The samples have a kurtosis range of -2.46 to 2.97, with a corresponding mean of 0.55. Table 3 displays 21 frequencies are extremely platykurtic, 4 platykurtic, 5 mesokurtic, 4 leptokurtic, and 4 very leptokurtic.

5. DISCUSSION

5.1. Granulometry

Granulometry is a popular method that is used to ascertain the depositional environment, origin, distribution, and transit of the rock [21, 22]. In addition, it offers crucial indications regarding the

Table 1. Sieve analysis data of studied samples and percentages of relatively coarse, medium and fine grain fractions.

	Cumulative Percentages after grain size analysis							Percentage of Fractions		
Sample Number	**-1**	**0**	**1**	**2**	**3**	**4**	**Finer**	**Gravel**	**Sand**	**Mud**
SQ4	5.02	10.09	15.46	20.80	53.30	77.08	100.00	5.02	72.06	22.92
SQ3	0.00	0.04	0.26	1.20	64.08	99.64	100.00	0.00	99.64	0.36
SQ2	0.00	0.00	0.50	2.76	67.64	99.20	100.00	0.00	99.20	0.80
SQ1	0.00	0.08	0.86	4.99	72.92	99.22	100.00	0.00	99.22	0.78
HN5	14.96	26.67	32.51	41.12	83.25	92.96	100.00	14.96	78.00	7.04
HN4	29.87	44.99	53.47	59.62	77.99	91.41	100.00	29.87	61.54	8.59
HN3	28.46	38.05	41.79	51.75	84.23	92.89	100.00	28.46	64.43	7.11
HN2	16.19	33.44	45.90	53.29	86.73	94.12	100.00	16.19	77.93	5.88
HN1	29.76	40.29	49.36	50.41	88.87	96.20	100.00	29.76	66.44	3.80
LB7	9.72	24.13	32.63	43.72	89.91	92.13	100.00	9.72	82.41	7.87
LB6	14.19	19.59	35.81	49.32	88.18	93.58	100.00	14.19	79.39	6.42
LB5	12.41	25.86	32.07	47.93	85.17	93.10	100.00	12.41	80.69	6.90
LB4	12.95	15.18	24.55	38.39	81.25	91.96	100.00	12.95	79.02	8.04
LB3	18.16	25.38	44.64	66.64	88.31	98.28	100.00	18.16	80.12	1.72
LB2	19.37	30.68	62.06	85.04	92.70	96.35	100.00	19.37	76.98	3.65
LB1	39.91	50.00	68.86	82.89	90.79	97.81	100.00	39.91	57.89	2.19
DM8	0.04	0.81	2.67	5.87	29.90	96.41	100.00	0.04	96.37	3.59
DM7	1.21	2.55	6.15	22.63	84.34	97.30	100.00	1.21	96.08	2.70
DM6	0.25	1.28	2.22	4.28	55.00	98.15	100.00	0.25	97.90	1.85
DM5	6.90	7.73	9.63	16.69	85.26	98.41	100.00	6.90	91.52	1.59
DM4	12.22	14.19	19.03	28.96	73.05	97.46	100.00	12.22	85.23	2.54
DM3	1.60	2.40	11.33	34.31	77.50	97.24	100.00	1.60	95.64	2.76
DM2	21.29	33.40	77.31	93.46	98.92	99.20	100.00	21.29	77.91	0.80
DM1	32.04	37.27	45.94	50.13	68.19	95.65	100.00	32.04	63.61	4.35
DT4	0.28	0.32	1.85	7.78	74.53	98.32	100.00	0.28	98.03	1.68
DT3	13.04	16.47	35.74	61.79	89.19	98.44	100.00	13.04	85.40	1.56
DT2	20.55	27.80	37.78	55.44	78.32	99.06	100.00	20.55	78.52	0.94
DT1	36.72	43.66	57.32	63.84	82.89	97.41	100.00	36.72	60.68	2.59
HG5	15.00	16.76	18.87	22.73	63.83	87.87	100.00	15.00	72.87	12.13
HG4	62.71	73.36	90.60	93.03	95.42	96.47	100.00	62.71	33.76	3.53
HG3	60.25	62.70	65.54	67.04	83.00	92.98	100.00	60.25	32.73	7.02
HG2	70.59	76.70	87.76	90.85	94.62	96.68	100.00	70.59	26.09	3.32
HG1	18.86	19.20	20.34	21.63	52.55	98.01	100.00	18.86	79.15	1.99
LT5	5.10	10.29	19.86	29.03	65.31	83.65	100.00	5.10	78.55	16.35
LT4	1.75	2.80	3.33	19.44	66.37	96.50	100.00	1.75	94.75	3.50
LT3	13.77	30.36	34.41	47.37	93.93	95.95	100.00	13.77	82.19	4.05
LT2	10.86	23.36	31.91	42.43	71.71	93.09	100.00	10.86	82.24	6.91
LT1	6.79	16.60	22.64	38.49	70.94	88.30	100.00	6.79	81.51	11.70

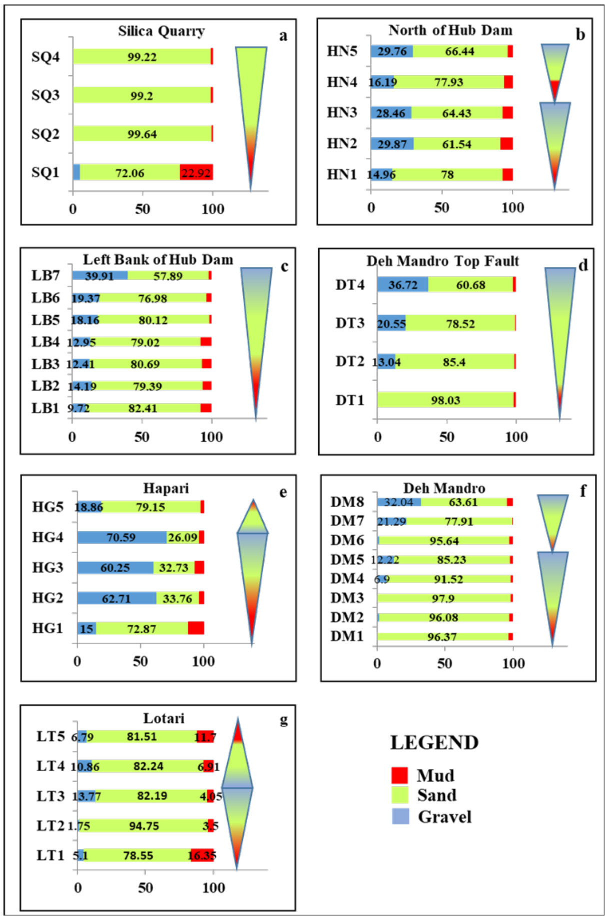

Fig. 3. Locality wise grain size fractions showing vertical distribution of grains (coarsening and finning sequences) and depositional cycles; fractions percentages are on x-axis and from bottom (older) to top (younger) samples are plotted on y-axis: (a) Silica Quarry, (b) North of Hub Dam, (c) Left Bank of Hub Dam, (d) Deh Mandro Top Fault, (e) Hapari, (f) Deh Mandro, and (g) Lotari.

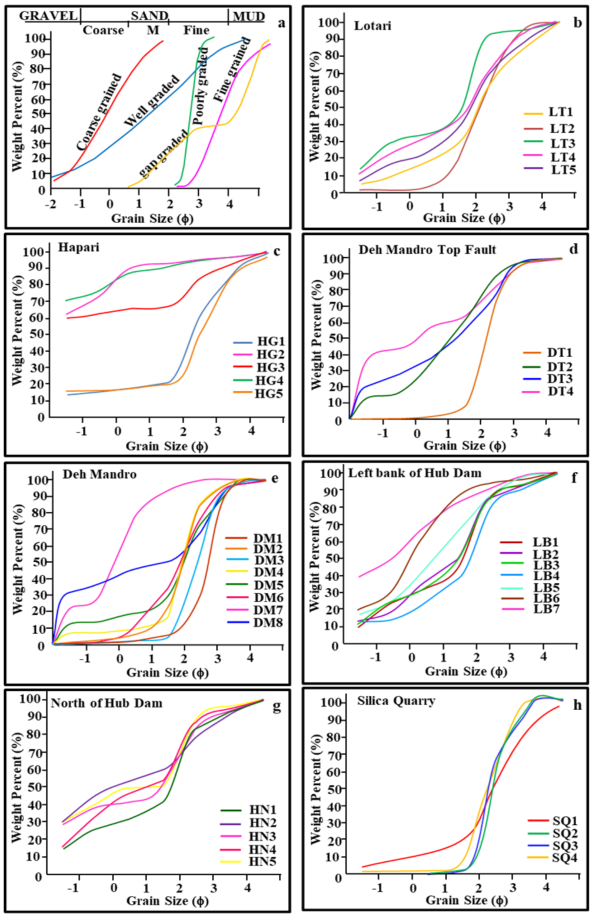

Fig. 4. Grain-size cumulative curves: (a) standard patterns, (b) Lotari, (c) Hapari, (d) Deh Mandro Top Fault, (e) Deh Mandro, (f) Left Bank of Hub Dam, (g) North of Hub Dam, and (h) Silica Quarry.

characteristics of sandstone reservoirs and the flow dynamics of systems [23]. Samples LT3, DT4, and DM7 (Figure 4(b, d-e)) exhibit curves resembling gap-graded pattern (Figure 4(a)); samples DT1, DM1-2 and 4 appear as poorly graded (Figure 4(d-e)). Sediment size grades provide important clues about the provenance and deposition of sediments [24]. Sand and gravel are coarse-grained sediments that are typically found in high-energy settings that can move larger particles, including rivers, near-shore zones, or areas that are impacted by waves or strong currents. Low-energy environments, such as deep lakes, estuaries, or offshore locations with weak currents, are associated with fine-grained sediments [25]. The sand was found to be the predominant component in the sieve analysis of the samples under study, followed by gravels (Figure 3). Only the SQ1 sample contains a significant percentage of fine-grained particles (i.e., 22.92%). The presence of a predominant coarse component in the examined samples suggests hydro-dynamically-driven deposition in rivers or near-shore settings.

5.2. Textural Parameters

For the textural study of sediments and depositional setting prediction, four key criteria are utilized: graphic mean size, sorting, skewness, and kurtosis. Folk [19] was the first to employ the graphic mean, which is the arithmetic average of the grain size in the sample. It shows the current velocity of the medium and turbulence in the deposition basin, together with the source's potential energy [25]. Amongst the 38 samples, twenty-four (63%) are medium-grained, and the remaining 37% samples are coarse-grained (Table 3). Overall, Orangi Sandstone samples are categorized as medium-grained. Such a grain pattern indicates that sandstone was formed under moderate to high energy conditions [26].

Table 2. Calculated values of textural parameters and classification of studied samples.

	Values				Classification			
Sample Number	**Mz**	**s_I**	**SKI**	**Kg**	**Mz**	**s_I**	**SKI**	**Kg**
SQ1	2.72	1.59	-0.08	1.51	Medium	ps	ns	vlk
SQ2	2.48	0.32	1.54	0.13	Medium	vws	vsfs	vpk
SQ3	2.45	0.39	1.41	0.16	Medium	ws	vsfs	vpk
SQ4	2.28	0.7	-0.05	00	Medium	mws	ns	vpk
HN1	1.7	1.56	-0.88	0.77	Medium	ps	scs	pk
HN2	0.22	1.55	1.21	0.32	Coarse	ps	vsfs	vpk
HN3	1.22	1.4	-0.96	0.28	Medium	ps	scs	vpk
HN4	0.83	1.46	-0.21	0.52	Coarse	ps	cs	vpk
HN5	0.72	1.36	-0.17	0.3	Coarse	ps	cs	vpk
LB1	1.4	1.08	-0.64	0.83	Medium	ps	scs	pk
LB2	0.95	1.38	-0.12	0.97	Coarse	ps	cs	mk
LB3	1.1	1.48	-0.27	1.42	Medium	ps	cs	lk
LB4	2.0	1.08	-0.84	1.35	Medium	ps	scs	lk
LB5	0.82	1.18	0.34	0.91	Coarse	ps	sfs	mk
LB6	0.37	0.78	0.87	0.43	Coarse	ms	sfs	vpk
LB7	0.35	0.83	1.49	0.51	Coarse	ms	vsfs	vpk
DM1	2.68	0.55	-0.34	1.87	Medium	mws	scs	vlk
DM2	1.93	0.39	-2.17	-2.46	Medium	ws	vscs	vpk
DM3	2.42	0.53	-0.02	0.87	Medium	mws	ns	pk
DM4	2.0	0.7	-0.72	2.97	Medium	mws	scs	vlk
DM5	1.42	1.49	-0.31	1.01	Medium	ps	scs	mk
DM6	1.85	1.03	-0.15	0.94	Medium	ps	cs	mk
DM7	-0.02	0.47	2.65	0.45	Coarse	ws	vsfs	vpk
DM8	1.52	1.27	0.03	0.52	Medium	ps	ns	vpk
DT1	2.25	0.53	0.14	1.2	Medium	mws	fs	lk
DT2	0.98	1.17	0.11	0.6	Coarse	ps	fs	vpk
DT3	0.65	1.59	-0.15	0.37	Coarse	ps	cs	vpk
DT4	0.2	1.61	0.53	0.35	Coarse	ps	sfs	vpk
HG1	2.5	1.08	-0.06	1.4	Medium	ps	ns	lk
HG2	0.02	0.54	1.0	-0.9	Coarse	mws	sfs	vpk
HG3	0.87	1.23	1.0	0.75	Coarse	ps	sfs	pk
HG4	0.07	0.6	1.0	-1.02	Coarse	mws	sfs	vpk
HG5	1.93	1.86	-0.77	0.6	Medium	ps	scs	vpk
LT1	1.92	1.45	-0.06	0.99	Medium	ps	ns	mk
LT2	2.16	0.99	-0.11	1.52	Medium	ms	cs	vlk
LT3	1.03	1.12	-0.32	0.42	Medium	ps	scs	vpk
LT4	1.33	1.59	-0.16	0.43	Medium	ps	cs	vpk
LT5	1.25	1.63	-0.09	0.65	Medium	ps	ns	vpk

Legend

ws	well sorted	ns	near symmetric	vpk	very platy kurtic
vws	very well sorted	vsfs	very strong finely skewed	vlk	very lepty kurtic
mws	moderately well sorted	vscs	very strong coarsely skewed	mk	meso kurtic
ms	moderately sorted	scs	strongly coarse skewed	lk	leptykurtic
ps	poorly sorted	sfs	strongly fine skewed	elk	extremely lepty kurtic
		cs	coarse skewed	pk	platy kurtic
		fs	finely skewed		

Sorting provides insights into the dependability of depositional and transportation processes. Better sorting will result from constant strength low or high currents, while poorly sorted sediments indicate mixed deposition and transportation [19]. Table 3 shows that the bulk of the samples (63%) are poorly sorted; 3 frequencies are classed as well sorted, 7 appear to be moderately well sorted, and

Table 3. Formulae, verbal limits and statistics of textural parameters [19, 20], and sample percentages.

Parameter/Class	Formula/Range	No. of Studied Samples in each class	Values/ Percentage of Studied Samples
Graphic Mean	$Mz = (f16 + f50 + f84)/3$	Minimum	-0.02
		Maximum	2.72
		Mean	1.38
Coarse grained	< 1	14	37%
Medium Grained	3-1	24	63%
Fine Grained	> 3	-	-
Inclusive Graphic Standard Deviation	$s_I = [(\phi_{84} - \phi_{16})]/4 + [(\phi_{95} - \phi_5)]/6.6$	Minimum	0.32
		Maximum	1.86
		Mean	1.09
Very well sorted	0.0 - 0.35	1	2.63%
Well sorted	0.35 - 0.50	3	7.89%
Moderately well sorted	0.50 - 0.71	7	18.42%
Moderately sorted	0.71 - 1.0	3	7.89%
Poorly sorted	1.0 - 2.0	24	63%
Very poorly sorted	2.0 - 4.0	-	-
Extremely poorly sorted	> 4	-	-
Inclusive graphic Skewness	$Sk_i = [(\phi16+\phi84-2\phi50)]/(2(\phi84-\phi16)] + [(\phi5+\phi95-2\phi50))/(2 (\phi95-\phi5)]$	Minimum	-2.17
		Maximum	2.65
		Mean	0.1
Very strongly fine skewed	> +1	5	13.16%
Strongly fine skewed	+1.0 to +0.30	6	15.79%
Fine skewed	+0.30 to + 0.1	2	5.26%
Near symmetry	+0.10 to -0.10	7	18.42%
Coarse skewed	-0.10 to -0.30	8	21.05%
Strongly coarse skewed	-0.30 to -1.0	9	23.68%
Very strongly coarse skewed	< -1.0	1	2.63%
Graphic Kurtosis	$K_G = [(\phi95- \phi5)]/[2.44(\phi5 - \phi25)]$	Minimum	-2.46
		Maximum	2.97
		Mean	0.55
Very platykurtic	< 0.67	21	55.26%
Platykurtic	0.67- 0.90	4	10.53%
Mesokurtic	0.90 - 1.11	5	13.16%
Leptokurtic	1.11 - 1.50	4	10.53%
Very leptokurtic	1.50 - 3.0	4	10.53%
Extremely leptokurtic	> 3.0	-	-

where ϕ_5, ϕ_{16}, ϕ_{25}, ϕ_{50}, ϕ_{75}, ϕ_{84} and ϕ_{95} represents 5th, 16th, 25th, 50th, 75th, 84th and 95th percentiles respectively on the cumulative curve.

3 samples are moderately sorted. It may be due to the rapid forth and backflow of the depositional environment as suggested by [27]. Poor sorting in sandstone is a sign that the basin contains variable-size sediments that may have been deposited by turbulent flow and currents with different velocities [28]. Present work also get support from the study of Kasim *et al*. [29] while working on onshore Peninsular Malaysia; showed that short-distance movement and deposition in a river environment are reflected by the predominance of poorly sorted sediments.

An imbalance in the grain size distribution curve is called skewness. According to Azidane *et al*. [30], skewness is a nuanced metric that may be used to assess subpopulation mixing and the energy circumstances that prevailed during deposition. Around 47% of samples have positive skewness values, followed by 34% with negative values and 18% with almost symmetrical values, which indicate mixing of the deposition and transit circumstances. Negatively skewed sediments are deposited because of high energy conditions, while symmetrically skewed sediments will thrive in low-intensity environments [31]. Mir and Jeelani [32] stated that positive skewness indicates unidirectional transportation and the deposition of sediments in low-energy settings. Additionally, Kasim *et al*. [29] reported that positive skewness in sediments is a result of fluvial settings. Most of the examined samples appear to originate from the fluvial environment, according to skewness and other textural metrics taken together. The degree of peakedness in the grain size distribution is known as graphic kurtosis [33-34]. According to Boboye *et al*. [22], it is a measure of the ratio between sorting the graph's center and tail. The mean values of studied samples reflect a preponderance of platykurtic character. Large variation in the values of kurtosis can be attributed to the fluctuation in depositional currents [35].

5.3. Environmental Interpretation

5.3.1. Bivariate analysis

By integrating several grain size factors in bivariate plots, one may reduce possible ambiguities associated with individual proxies and provide a more inclusive understanding of the paleo-environment/ paleo-provenance [36-37]. Additionally, it may be applied to distinguish between different sedimentation settings and analyze energy circumstances [30]. To interpret the paleo-environment based on sedimentological constraints, a few scatter plots were made, including mean vs. standard deviation [26], mean vs. skewness, sorting vs. skewness [27], and Stewart diagram [30].

To understand the origin of sediment, Ayodele and Madukwe [27] employed a bivariate visualization between sorting and mean grain size that showed the analyzed samples were deposited by fluvial processes (Figure 5(a)). The Figure 5(b), which distinguishes between overbank, river channel, and overbank-pool deposits, illustrates that majority of the samples are inclined towards river channel deposits. Using the same granulometric metrics, Elsherif *et al*. [34]; and Moiola and Weiser [38] also demarcated the fields of beach, coastal dune, and river-deposited sediments. Few samples diverged towards the coastal dune to beach habitat, while majority of the samples seemed to have been deposited by rivers (Figure 5(b)).

Mean sizes against skewness plots are another tool used by Ayodele and Madukwe [27] to identify overbank and overbank-pool as well as river channel deposits. Most of the examined samples are plotted around the deposits seen in river channels (Figure 6(a)). The above-stated outcome is further corroborated by research of Folk and Ward [20], Adeoye *et al*. [39], and Kasim *et al*. [29], who divide beach/near shore, tidal current and fluvial environment using a customized plot of skewness vs. standard deviation (sorting). Plots of the samples on skewness vs. standard deviation bivariate graph show that 71% of them are inside the river zone, suggesting that the samples were

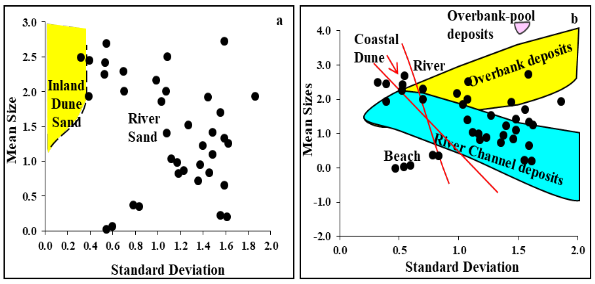

Fig. 5. Scattered plots between mean size and standard deviation reflecting: (a) nature of sediments after [27] and (b) type of deposits after [38]; while boundaries marked by red lines after [34].

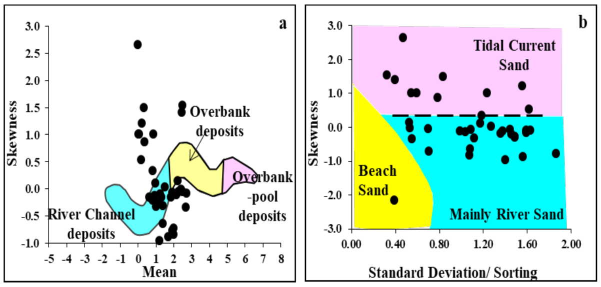

Fig. 6. Bivariate plots between: (a) mean vs. skewness after [27], and (b) standard deviation vs. skewness after [39].

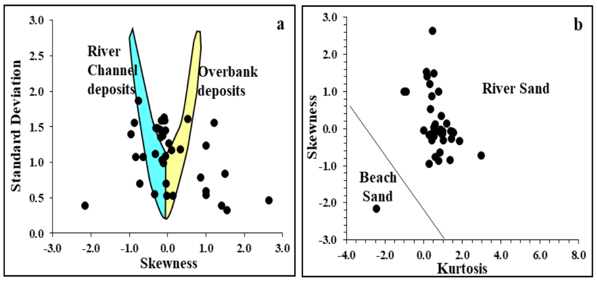

Fig. 7. Scattered plots between: (a) skewness vs. standard deviation after [27], and (b) Kurtosis and Skewness after [39].

transported and deposited by rivers (Figure 6(b)). In contrast, 23% of samples diverged and were deposited by tidal currents.

Furthermore, it is reinforced by research conducted by Ayodele and Madukwe [27], which used a graph between sorting and skewness to distinguish between overbank deposits and river channel fields. Although the plots of the analyzed samples are rather dispersed, most of them are oriented towards river deposits (Figure 7(a)). Adeoye *et al*. [39] distinguished between river and beach sands using a kurtosis vs. skewness plot. The fluvial provenance of sandstones is validated by the bivariate graph in Figure 7(b) that shows the dominance of river transportation between kurtosis and skewness of the studied samples.

5.3.2. Linear discriminant function (LDF)

A powerful method for determining the predominant sedimentation process in the area is Sahu's linear discriminant function, which was employed by several studies [29, 40]. Sahu [41] made use of statistical measures and constituted four LDFs (Y1, Y2, Y3, and Y4) to construe the energy and fluidity of depositional environments. Equations for LDFs, their ranges, interpretation of the deposition environment, and the estimated values of analyzed samples are shown in Table 4. About 76% of samples appear to have Y1 values > -2.7411, indicating a beach environment while nine samples have values less than -2.7411, indicating a tendency towards an aeolian environment of deposition. More than 92% of the samples reveal deposition in a shallow, turbulent marine environment, having a value of Y2 > 65.3650. Only three samples were recognized by the discriminant Y2 as deposits from the beach environment. When accounting for Y3, 100% of the samples had values less than -7.419 which indicates a fluvial environment. Mutual deposition in turbid and fluvial settings is implied by the Y4 values; 52.6% of the samples have values less than, and 47.4% of samples have values greater than -2.7411 (Table 4). The average values of all LDFs collectively, for all samples show shallow water to fluvial environment with minimal turbidity current effect.

The cross-plots Y2 vs. Y3 (Figure 8(a)) and Y3 versus Y4 (Figure 8(b)) are designed to verify the actual conditions that existed during the deposition of Orangi Sandstone. It was most likely deposited in the transitional zone under the combined effect of fluvial and shallow agitated water conditions, according to the bivariate plots. The worldwide eustatic curve pattern which shows constant variations in sea level throughout the Oligocene, lends more credence to this assumption. According to Welcomme *et al*. [45], the Nari Formation in the southernmost Kirthar Province is composed of well-developed transgressive marine sediments that were gradationally influenced by river circumstances.

5.3.3. Stewart diagram

Stewart [43] presented a graphical representation

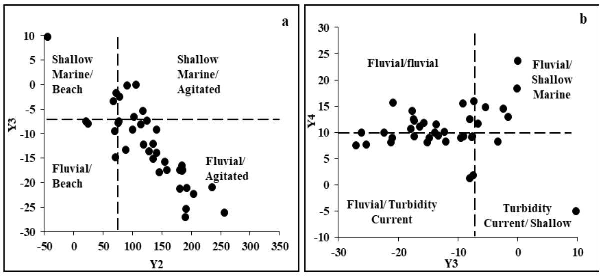

Fig. 8. Discrimination of environment of studied samples based on LDF plots: (a) Y2 vs. Y3 after [40], and (b) Y3 vs. Y4 after [29].

Table 4. Linear discriminate functions (LDF) formulae for calculation after Sahu [41] and environmental interpretation after [27].

Linear Discriminate Function	Environment	Formulae	Interpretation	Studied Samples
Y1	Aeolian and Beach	$Y1 = -3.5688\ Mz + 3.7016\ \sigma_i^2 - 2.0766\ SK + 3.1135\ KG$	$Y1 < -2.7411$ represents Aeolian deposition; $Y1 > -2.7411$ signifies Beach environment	Min. -11.2798 Max. 9.44 Mean 1.95 Aeolian 23.68% Beach 76.32%
Y2	Beach and Shallow Agitated Marine	$Y2 = 15.6534\ Mz + 65.7091\ \sigma_i^2 + 18.1071\ SK + 18.5043\ KG$	$Y2 < 65.3650$ indicates Beach deposition; $Y2 > 65.3650$ represents Shallow Agitated Marine environment	Min. -44.4302 Max. 255.87 Mean 126.10 Beach 7.89% Shallow Agitated Marine 92.11%
Y3	Shallow Agitated Marine and Fluvial	$Y3 = 0.2852\ Mz - 8.7604\ \sigma_i^2 - 4.8932\ SK1 + 0.0482\ KG$	$Y3 < -7.419$ characterize Fluvial environment; $Y3 > -7.419$ the environment is Shallow Marine.	Min. -27.0356 Max. 9.696 Mean -12.1759 Fluvial 100%
Y4	Fluvial and Turbidity Conditions	$Y4 = 0.7215\ Mz + 0.403\ \sigma_i^2 + 6.7322\ SK + 5.2927\ KG$	$Y4 < 10.000$ the environment is Fluvial and if > 10.000, the environment is Turbidity	Min. -4.9493 Max. 23.7029 Mean 10.5007 Fluvial 52.64% Turbidity 47.36%

of depositional processes utilizing median grain size and sorting in phi values. Three processes that reflect distinct sedimentary settings explained by the Stewart diagram are: (1) wave action-driven shoreward processes; (2) fluvial events, especially floods; and (3) slow deposition from calm seas. Lukman *et al*. [44] and Parthasarathy *et al*. [45] further revised it and demarcated the inner shelf environment on the Stewart diagram. Samples plotted on the Stewart diagram reveal that river activities had a major influence on the Orangi Sandstone, with wave action having a combined effect on a small number of samples (Figure 9). This behavior suggests that the Orangi Sandstone may have been deposited in a transitional environment.

5.3.4. Vertical-Lateral variation in studied samples

The exposition of depositional environment depends on studies of lateral and vertical variation in rock assemblage [46]. These differences may primarily be described for sedimentological investigations based on the lithology, grain size, colour, bed continuity, and primary structures. Sandstone was found to be the predominant lithology in the samples under study, followed by conglomerates.

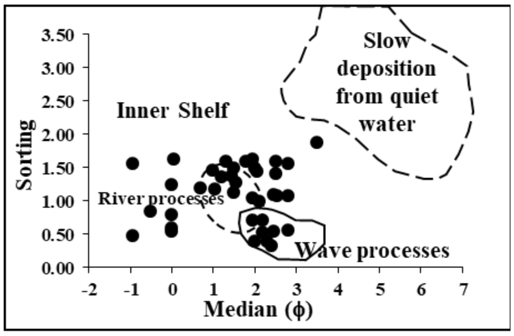

Fig. 9. Plots of studied samples on Stewart diagram [43] based on sorting and median values; boundaries after [30].

Additionally, variations in sandstone were observed, with the most common types being pure sandstone, muddy sandstone, gravelly sandstone; and just six samples make up the sandy conglomerate facies (see Figure 10).

The lithology's spatial distribution pattern (Figure 11) shows that in the extreme northeast (the Silica quarry site), the predominant facies is pure sandstone, while the amount of gravel and mud rises as one moves towards west (to the HN and LB). Little mud and coarse fraction of sandstone are present in the early stages of deposition; however, as time goes on, the amount of gravel in the strata rises steadily, causing the facies to transition from muddy gravelly sandstone to gravelly sandstone to sandy conglomerate. The repetition of facies in vertical succession is observed in the Lotari (LT) and Hapari (HG) sites in the southwest (Figure 3). Comparison of the locality-wise distribution of grain size (Figure 3) shows that there are two depositional sequences in southwest localities (LT and HG), from older to younger samples. In bottom samples, a coarsening upward pattern is observed, followed by a finning upward pattern in top samples that complies with Walther's law of facies. The existence of sole marks and the normal grading of sediments (upward finning) indicate that turbidity currents are responsible for deposition. Similar circumstances were also mentioned by Zou *et al.* [48] during their investigation of the Yanchang Formation in China. The samples taken from the north of Hub Dam (HN) and Deh Mandro (DM) sites showed two cycles of deposition. In each cycle, upward coarsening sequences were observed; in contrast, only one upward coarsening cycle was witnessed at the sites of DT, LB, and SQ (Figure 1). Hiatt [49] states that fining upward sedimentary facies successions are symbolic of point bar deposits (i.e., banks of meander bends) in the fluvial environment, while coarsening upward facies successions are suggestive of prograding shoreface and deltaic environments.

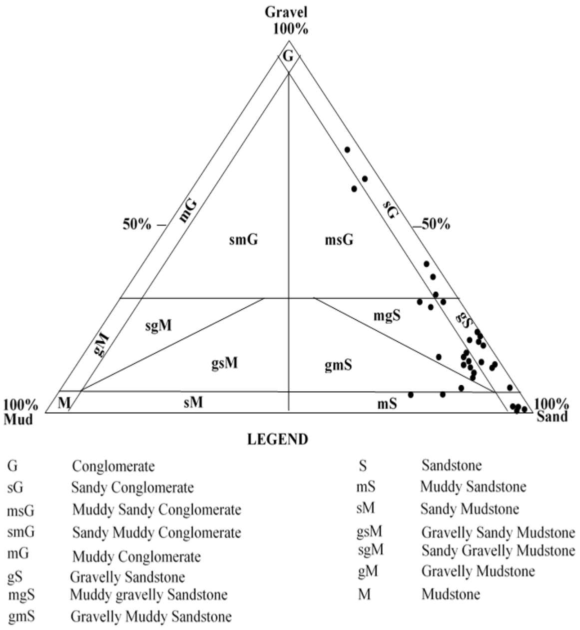

Fig. 10. Classification of studied samples on sand-gravel-mud diagram, fields after [47].

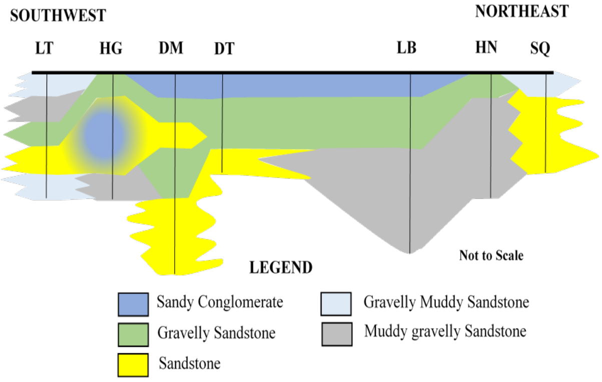

Fig. 11. Lateral variation in lithology of studied samples from southwest to northeast.

The primary ingredient that binds the sediments to create a consolidated rock is cement. This can indicate the depositional site's oxidation conditions and can originate from several sources during diagenesis. Cementing material's spatial distribution exhibits vertico-lateral variation within the samples (Figure 12(a)). Three different forms of cement are found in the samples under study, ranging in composition from calcareous, ferruginous to siliceous in varying proportions. Deposits of ferruginous material occur in conditions of high (hematite) to somewhat low (limonite) oxidation. The occurrence of iron oxide; hematite cement in the bottom samples and limonite in the top samples of the LT section (Figure 12(a)), indicates an oscillating environment that is also evident in the lithology and grain size. Towards NE, the ferrous material was altered to ferric oxide with the addition of calcareous cement. The calcareous cement samples are comparatively harder. The small-scale syn-depositional fault is the cause of the calcareous cement observed in the HG2-HG4 samples (Figure 12(a)). The distribution and content of cement are ultimately influenced by fractures and faults, which control the fluid movement across stratigraphic units [50]. Sample HG5 and SQ1 contain siliceous cementing material; the latter (SQ1) is collected from silica quarry. The reason for the low siliceous cement in other samples is that in the fluvial environment, shallow meteoric water produces very little siliceous content [51].

For the first time, textural factors (kurtosis and skewness) are utilized in addition to lithology and cementing material to create lateral variation within the Orangi Sandstone. Based on kurtosis analysis (Figure 12(b)), most samples exhibit very platykurtic distributions, indicating a wide spread in grain size and suggesting poor sediment sorting. When integrated with lithological characteristics and grain size data, this facies is divided into two: Subfacies-1with relatively coarse grains and a gritty texture found on top, whereas subfacies-2, located below the top, have a texture with medium sand grains. The platykurtic facies are mostly found in the lower sedimentary successions, indicating that they were deposited under conditions of rapid, erratic flow, perhaps as a result of abrupt sediment influx. Conversely, mesokurtic to very leptokurtic facies predominate in the central parts of the successions, especially those that trend southwestward. These are typically linked to fine to very fine-grained, poorly sorted sandstones, which are a sign of high-energy settings like swift-moving river systems that can carry finer sediments in suspension and deposit them selectively when energy levels are dropping [52]. These deposits' leptokurtic character indicates more consistent flow dynamics during deposition and reflects a narrower grain size distribution. Figure 12(c) shows the distribution of the skewness of studied samples. There are two distinct facies identified: the strongly to very strongly fine skewed and the coarse to strongly coarse skewed facies. For most of the research area, both facies are found parallel to one another (Figure 12(c)), indicating a fluctuating environment. On the other hand, symmetrical to very fine skewed facies predominate in the northeast site (SQ), whereas coarse skewed facies dominate at the extreme southwest site.

5.4. Depositional Model

A complete picture of the depositional basin and related geodynamic environment may be obtained from the variation in grain size, the difference in facies, and the variety of cementing materials in a clastic sequence [49]. In the fluvial-deltaic system of deposition, the vertico-lateral variation offers insights into flow regimes [31]. The tectonic system of an area is crucial in generating facies heterogeneity [53]. The Early Tertiary India-Eurasia convergence had effects on the research region [54]. Variations in sea level at the time of

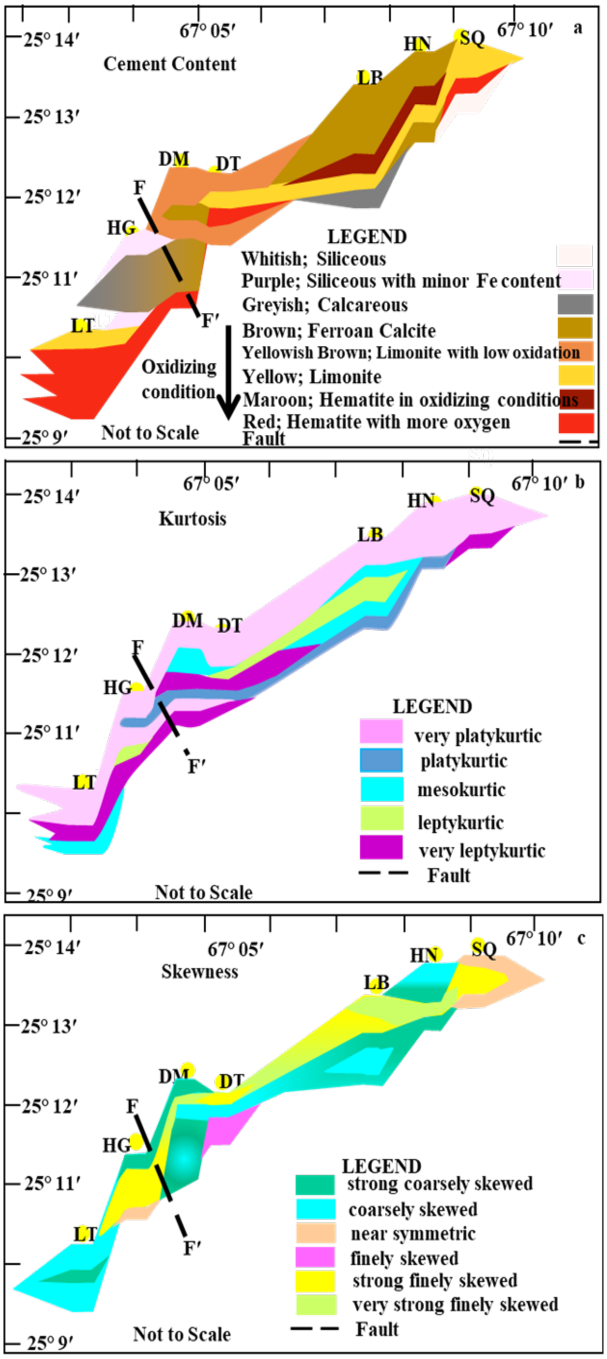

Fig. 12. Idiosyncrasy of studied samples based on variations in: (a) cement content, (b) kurtosis values, and (c) skewness values.

deposition also contribute to the supply of sediment [55]. An integrated approach is used to create a schematic depositional model below.

The Indian Plate had a major tectonic event near the end of the Cretaceous (65 Ma) when it crossed over the Réunion hotspot. This caused the Proterozoic Aravalli igneous and metamorphic complex to erode. According to Mehmood *et al*. [46], the weathered sediments were deposited as the Maastrichtian Pab Formation in the southern Indus Basin. Based on paleocurrent data and discrimination diagrams, Ahmed *et al*. [18] and Umar *et al.* [56] demonstrated that the sediments of the Pab Sandstone originated from the Precambrian Aravali Mountain belt, which is in the east and southeast along the boundary between Pakistan and India.

The deposition of the Nari and Gaj formations as well as the Siwaliks was caused by three different periods of sediment supply, which Kazmi and Jan [57] categorized from north to south. These stages are the Middle to Late Paleocene, Early Oligocene to Early Miocene, and Middle Pliocene to Pleistocene. Throughout the Cenozoic era, there were variations in the deposition of sediments in a variety of locations, mostly because of sea level oscillations. These changes included rising (Himalayan orogeny), erosion, and subsequent deposition. The sea receded southward until the Oligocene (40 Ma), when it formed shallow marine depositional basins in the Karachi region, mostly in the form of estuaries and embayments [58]. Sea level rise from 27 to 23 Ma was constant in the Orangi Sandstone unit of the Nari Formation, from 130 to 160 meters. The deposition of Orangi Sandstone in the variable environment is also reflected in the interpretation of grain size textural factors.

Keeping this in mind, a fabricated depositional model of the Orangi Sandstone in the research region is shown Figure 13. This model also gets support from the study Paryal *et al.* [59] and Samtio *et al.* [35] who also confirmed that the Nari Formation was deposited in a shallow marine basin, mostly as a beach and deltaic environment while working in the Kirthar Province.

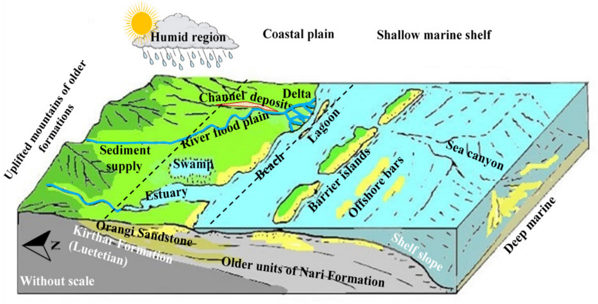

Fig. 13. Hypothetical sketch showing depositional model of Orangi Sandstone in the study area during Oligocene, marked by broken lines.

This diagram depicts a thorough depositional model moving from continental to deep marine environments revealing the deposition of various units of Nari Formation. Uplifted mountainous areas with a humid climate are the source of sediments, which causes severe weathering and erosion. These sediments eventually form deltaic deposits along the coast after being carried by a fluvial system that includes river flood plains, swamps, estuaries, and channel deposits. The Orangi Sandstone is stratigraphically positioned above older Nari Formation units, indicating a transgressive-regressive depositional history impacted by tectonic activity and variations in sea level. It is also supported by presence of cross-bedding and ripple marks reflecting river or tidal channel activity. Further, occurrence of honeycomb weathering suggests chemical weathering in a marine or tidal setting under humid or semi-arid conditions. The processes of sediment dispersal and facies variation throughout a foreland are well represented by this model. This model effectively captures the facies variation and sediment dispersal processes across a foreland basin system.

6. CONCLUSIONS

Based on lithology, grain size, and cementing material it is concluded that Orangi Sandstone is a pure sandstone that reflects medium to coarse-grain size sand particles. The sandstone exhibits gravelly to sandy-muddy texture with few exceptions. The presence of all three types of cement (calcareous, ferruginous, and siliceous) reveals the deposition of Orangi sandstone under variable flow conditions. The sedimentological statistics also certified the transitional fluctuating depositional environment. The extremely platykurtic to platykurtic-type facies are dominated and are mostly found in the upper parts of the studied section while the mesokurtic to leptokurtic facies are restricted to the southwest sections and are enclosed by extremely platykurtic to platykurtic-type facies. The pattern of kurtosis and simultaneous occurrence of coarse to extremely coarse and strong to very strongly fine skewed facies supports the deposition of Orangi Sandstone in the shallow marine to fluvial-deltaic zone, where the channel, tidal current, and beach/near coast environment existed. Conceptual model of deposition exhibited that accumulation of the Orangi Sandstone has occurred over older Nari Formation units, with sediments being transported from the uplifted northern terrain into the depositional basin. The model invokes an Upper Oligocene tectonic uplift, tied to Himalayan orogenic activity, and associated sea-level rise and fall, leading to fluctuating energy conditions and sedimentation patterns.

7. CONFLICT OF INTEREST

The authors declare no conflict of interest.

8. REFERENCES

1. D. Liu, Z. Gu, R. Liang, J. Su, D. Ren, B. Chen, and C. Yang. Impacts of pore-throat system on fractal characterization of tight sandstones. *Geofluid* 2020(1): 4941501 (2020).
2. J.E. Houghton, J. Behnsen, R.A. Duller, T.E. Nichols, and R.H. Worden. Particle size analysis: A comparison of laboratory-based techniques and their application to geoscience. *Sedimentary Geology* 464: 106607 (2024).
3. R. Khalil. Investigating the depositional environments using particle-size analysis of Lower Cretaceous sandstone reservoirs, Biyadh Formation, Saudi Arabia. *Journal of Taibah University for Science* 18(1): 1-9 (2024).
4. C.A. Allen, I.G. Udo, T.A. Harry, and A.E. Ekot. Granulometric and Pebble Morphometric Analyses of Sandstone Lithofacies of the Ameki Formation in Northeastern Part of Akwa Ibom State, Niger Delta, Nigeria. *Researchers Journal of Science and Technology* 4(1): 32-44 (2024).
5. A. Khan, U. Khadim, and S. Anjum. Assessment of Orangi Sandstone Unit of Nari Formation, Karachi: Industrial Applications with Special Focus on Glass Making. *International Journal of Ground Sediment & Water* 7(1): 365-380 (2018).
6. G. Wang, Q. Lei, Z. Huang, G. Liu, Y. Fu, N. Li, and J. Liu. Genetic Relationship between Mississippi Valley-Type Pb–Zn Mineralization and Hydrocarbon Accumulation in the Wusihe Deposits, Southwestern Margin of the Sichuan Basin, China. *Minerals* 12(11): 1447 (2022).
7. R.M. Abraham-A, F. Taioli, and A.I. Nzekwu. Physical properties of sandstone reservoirs: Implication for fluid mobility. *Energy Geoscience* 3(4): 349-359 (2022).
8. M.T. Sohail, A. Hussan, M. Ehsan, N. Al-Ansari, M.M. Akhter, Z. Manzoor, and A. Elbeltagi. Groundwater budgeting of Nari and Gaj formations and groundwater mapping of Karachi, Pakistan. *Applied Water Science* 12(12): 267 (2022).
9. Y. Yan, L. Zhang, X. Luo, K. Liu, B. Yang, and T. Jia. Simulation of ductile grain deformation and the porosity loss predicted model of sandstone during compaction based on grain packing texture. *Journal of Petroleum Science and Engineering* 208 (1): 109583 (2022).
10. N.K. Siddiqui (Ed.). Petroleum Geology, Basin Architecture and Stratigraphy of Pakistan. *Nusrat K. Siddiqui* (2016).
11. S.M.I. Shah. Stratigraphy of Pakistan. Volume 22. *Geological Survey of Pakistan* (2009). https://hostnezt.com/cssfiles/geology/STRATIGRAPHY%20OF%20PAKISTAN%20BY%20S.M.%20IBRAHIM%20SHAH.pdf
12. G. Li, C. Qi, Y. Sun, X. Tang, and B. Hou. Experimental Study on the Softening Characteristics of Sandstone and Mudstone in Relation to Moisture Content. *Shock and Vibration* 14(1): 4010376 (2017).
13. J. Alali. Mineral Processing of Silica Sand in Hanout Area South of Jordan. *Open Journal of Geology* 13(7): 667-696 (2023).
14. C. Zoramthara, V.Z. Ralte, and Lalramdina. Grain-size analysis of Tipam sandstones near Buhchang village, Kolasib district, Mizoram. *Science Vision* 15(Supplementary issue): 43-51 (2015).
15. R. Khalil. Grain-Size Analysis of Middle Cretaceous Sandstone Reservoirs, the Wasia Formation, Riyadh Province, Saudi Arabia. *Sustainability* 15(10): 7983 (2023).
16. S.A. Khan, Z. Saeed, A. Khan, G. Hamid, and S.W. Haider. Assessment of Soil Liquefaction Potential in Defence Housing Authority, Karachi, Pakistan. *International Journal of Economic and Environmental Geology* 8(2): 63-68 (2017).
17. I.B. Kadri (Ed.). Petroleum Geology of Pakistan. *Pakistan Petroleum Limited* (1995).
18. Z. Ahmed, A. Khan, and B. Ahmed. Sandstone Composition and Provenance of the Nari Formation, Central Kirthar Fold belt, Pakistan. *Pakistan Journal*

of Geology 4(2): 90-96 (2020).

19. R.L. Folk (Ed.). Petrology of Sedimentary Rocks. *Austin, Hemphill Publishing Company* (1956).
20. R.L. Folk and W.C. Ward. Brazos River Bar: A Study in the Significance of Grain Size Parameters. *Journal of Sedimentary Research* 27(1): 3-26 (1975).
21. Y. Shi, E. Chongyi, Z. Zhang, Q. Peng, J. Zhang, W. Yan, and C. Xu. Comparison and significance of grain size parameters of the Menyuan loess calculated using different methods. *Open Geosciences* 15(1): 20220474 (2023).
22. O.A. Boboye, O.K. Jaiyeoba, and E.E Okon. Characteristics and mineralogical studies of some Cretaceous sandstones in Nigeria: implications for depositional environment and provenance. *Journal of Sedimentary Environments* 6(4): 531-550 (2021).
23. H.L. Brooks, E. Steel, and M. Moore. Grain Size Analysis of Ancient Deep-Marine Sediments using Laser Diffraction. *Frontiers in Earth Science* 10: 820866 (2022).
24. G. Li, R. Du, J. Tang, Z. Li, Q. Xia, B. Shi, L. Zhou, Y. Yang, and W. Zhang. Comparison of the graphic and moment methods for analyzing grain-size distributions: A case study for the Chinese inner continental shelf seas. *International Journal of Sediment Research* 37(6): 729-736 (2022).
25. M. Roem, M. Musa, and Y. Risjani. Sediment dynamics and depositional environment on Panjang Island reef flat, Indonesia: insight from grain size parameters. *Aquaculture, Aquarium, Conservation & Legislation* 14(1): 357-370 (2021).
26. G.O. Aigbadon, A. Ocheli, O.C. Akakuru, E.O. Akudo, S.D. Christopher, O. Esharive, and J.A Francis, Paleoenvironments and hydrocarbon reservoir potentials from the selected sedimentary basins in Nigeria using sedimentary facies and textural analyses. *Journal of Sedimentary Environments* 7(3): 371-401(2022).
27. O.S. Ayodele and H.Y. Madukwe. Granulometric and Sedimentologic Study of Beach Sediments, Lagos, Southwestern Nigeria. *International Journal of Geosciences* 10(3): 295-316 (2019).
28. A.D. Miall (Ed.). The geology of fluvial deposits: Sedimentary facies, basin analysis and petroleum geology. *Springer* (1996).
29. S.A. Kasim, M.S. Ismail, and N. Ahmed. Grain size statistics and morphometric analysis of Kluang-Niyor, Layang-Layang, and Kampung Durian Chondong Tertiary Sediments, Onshore Peninsular Malaysia: Implications for paleoenvironment and depositional processes. *Journal of King Saud University-Science* 35(2): 102481 (2023).
30. H. Azidane, B. Michel, M.E. Bouhaddioui, S. Haddout, B. Magrane, and A. Benmohammadi. Grain size analysis and characterization of sedimentary environment along the Atlantic Coast, Kenitra (Morocco). *Marine Georesources & Geotechnology* 39(5): 569-576 (2021).
31. T.J. Arun, K.R. Prasad, T.D. Aneesh, A.T. Limisha, M.K. Sreeraj, and R. Srinivas. Studies on the Textural Characteristics of Sediments from Periyar River Basin, Kerala, Southern India. *International Journal of Applied Environmental Sciences* 14(5): 495-526 (2019).
32. R.A. Mir and G.H. Jeelani. Textural characteristics of sediments and weathering in the Jhelum River basin located in Kashmir Valley, western Himalaya. *Journal of the Geological Society of India* 86: 445-458 (2015).
33. R.L. Folk. A review of grain-size parameters. *Sedimentology* 6(2): 73-93 (1966).
34. E.A. Elsherif, A. Badawi, and T. Abdelkader. Grain size distribution and environmental implications of Rosetta beach, Mediterranean Sea coast, Egypt. *Egyptian Journal of Aquatic Biology & Fisheries* 24(1): 349-370 (2020).
35. M.S. Samtio, A.A.A.D. Hakro, R.A. Lashahri, A.S. Mastoi, R.H. Rajper, and M.H. Agheem. Depositional Environment of Nari Formation from Lal Bagh Section of Sehwan Area, Sindh Pakistan. *Sindh University Research Journal* 53(01): 67-76 (2021).
36. Q. Zhang, Y. Wang, X. Wang, H. Yang, and T. Wang. Grain-size characteristics and sedimentary environmental significance of terrestrial red sandstone in the Dongying Depression with a gentle slope zone. *Bulletin of Geological Science and Technology* 43(5): 81-94 (2024).
37. S. Mishra, R.N. Hota, and B. Nayak. Grain size analysis and an overview of the sedimentary processes in Chandrabhaga beach, east coast of India. *Arabian Journal of Geosciences* 17(7): 214 (2024).
38. R.J. Moiola and D. Weiser. Textural parameters; an evaluation. *Journal of Sedimentary Research* 38(1): 45-53 (1968).
39. J.A. Adeoye, V.O. Jolayemi, and S.O. Akande. Sedimentology and foraminiferal paleoecology of the exposed Oligocene–Miocene Ogwashi-Asaba Formation in Issele-Uku area, Anambra Basin, southern Nigeria: A paleoenvironmental reconstruction. *Journal of Palaeogeography* 11(4): 618-628 (2022).

40. C. Baiyegunhi, K. Liu, and O. Gwavava. Grain size statistics and depositional pattern of the Ecca Group sandstones, Karoo Supergroup in the Eastern Cape Province, South Africa. *Open Geosciences* 9(1): 554-576 (2017).
41. B.K. Sahu. Depositional Mechanisms Form the Size Analysis of Clastic Sediments. *Journal of Sedimentary Petrology* 34(1): 73-83 (1964).
42. J.L. Welcomme, M. Benammi, J.Y. Crochet, L. Marivaux, G. Métais, P.O Antoine, and I. Baloch. Himalayan Forelands: palaeontological evidence for Oligocene detrital deposits in the Bugti Hills (Balochistan, Pakistan). *Geological Magazine* 138(4): 397-405 (2001).
43. H.B. Stewart. Sedimentary Reflections of Depositional Environments in San Miguel Lagoon, Baja California, Mexico. *American Association of Petroleum Geologists Bulletin* 42(11): 2567-2618 (1958).
44. A.M. Lukman, R. Ayuba, and T.S. Alege. Sedimentology and depositional environments of the Maastrichtian Mamu Formation, Northern Anambra Basin, Nigeria. *Advances in Applied Science Research* 9(2): 53-68 (2018).
45. P. Parthasarathy, G. Ramesh, S. Ramasamy, T. Arumugam, P. Govindaraj, S. Narayanan, and G. Jeyabal. Sediment dynamics and depositional environment of Coleroon river sediments, Tamil Nadu, Southeast coast of India. *Journal of Coastal Sciences* 3(2): 1-7 (2016).
46. M. Mehmood, A.A. Naseem, M. Saleem, J.U. Rehman, G. Kontakiotis, H.T. Janjuhah, and S.M. Siyar. Sedimentary Facies, Architectural Elements, and Depositional Environments of the Maastrichtian Pab Formation in the Rakhi Gorge, Eastern Sulaiman Ranges, Pakistan. *Journal of Marine Science and Engineering* 11(4): 726 (2023).
47. K.M. Farrell, W.B. Harris, D.J. Mallinson, S.J. Culver, S.R. Riggs, J. Pierson, J.M. Self-Trail, and J.C. Lautier. Standardizing Texture and Facies Codes for a Process-Based Classification of Clastic Sediment and Rock. *Journal of Sedimentary Research* 82(6): 364-378 (2012).
48. C. Zou, L. Wang, S. Tao, L. Hou, and A.J. Van Loon. Debrite turbidite transitions in the Chang 6 Oil Member of the Yanchang Formation (Ordos Basin, China). In: The Ordos Basin. R. Yang and A.J. Van Loon (Eds.). *Elsevier* pp. 411-420 (2022).
49. E.E. Hiatt. Sedimentology and sequence stratigraphy in basin analysis and paleohydrologic studies. In: Fluids and Basin Evolution. K. Kyser (Ed.). *Mineralogical Association of Canada, Ottawa* pp.19-38 (2000).
50. X. Sun, E. Gomez-Rivas, D. Cruset, J. Alcalde, D. Muñoz-López, I. Cantarero, and A. Travé. Origin and distribution of calcite cements in a folded fluvial succession: The Puig-reig anticline (south-eastern Pyrenees). *Sedimentology* 69(5): 2319-2347 (2022).
51. E.F. McBride. Quartz cement in sandstones: A review. *Earth-Science Reviews* 26(1-3): 69-112 (1989).
52. H.G. Reading (Ed.). Sedimentary Environments: Processes, Facies, and Stratigraphy *Blackwell Science Ltd*. (1996).
53. S. Hossain, H. Shekhar, and N. Rahman. Facies and architectural element analysis of the Upper Bokabil Sandstone in the Bengal Basin. *Sedimentary Geology* 453: 106433 (2023).
54. M. Yoshida and Y. Hamano. Pangea breakup and northward drift of the Indian subcontinent reproduced by a numerical model of mantle convection. *Scientific Reports* 5(1): 8407 (2015).
55. Z.F.M. Burton, T. McHargue, C.H. Kremer, R.B. Bloch, J.T. Gooley, C. Jaikla, J. Harrington, and S.A. Graham. Peak Cenozoic warmth enabled deep-sea sand deposition. *Scientific Reports* 13(1): 1276 (2023).
56. M. Umar, H. Friis, A.S. Khan, G. Kelling, A.M. Kassi, M.A. Sabir, and M. Farooq. Sediment Composition and Provenance of the Pab Formation, Kirthar Fold Belt, Pakistan: Signatures of Hot Spot Volcanism, Source Area Weathering, and Paleogeography on the Western Passive Margin of the Indian Plate during the Late Cretaceous. *Arabian Journal for Science and Engineering* 39: 311-324 (2014).
57. A.H. Kazmi and M.Q. Jan. (Eds.) Geology and Tectonics of Pakistan. *Graphic Publisher*s (1997).
58. A.H. Kazmi and I.A. Abbasi (Eds.). Stratigraphy and Historical geology of Pakistan. *Department & National Centre of Excellence in Geology, Peshawar, Pakistan* (2008).
59. M. Paryal, M.H. Agheem, G. Hussain, M.A. Kalwar, M. Hussain, and H. Asghar. Petrography of upper Nari Formation, Gandri Jabal, Pakistan. *North American Academic Research* 3(5): 178-199 (2020).

Proceedings of the Pakistan Academy of Sciences: A Physical and Computational Sciences 62(2): 165-173 (2025)
Copyright © Pakistan Academy of Sciences
ISSN (Print): 2518-4245; ISSN (Online): 2518-4253
http://doi.org/10.53560/PPASA(62-2)692

Pakistan Academy of Sciences

Research Article

Electro-remediation of Chromium and Associated Heavy Metals from Soils Affected by Leather Tannery Waste Effluents in Sambrial Town, Pakistan

Maria Khalid[1*], Sajid Rasheed Ahmad[1], Riffat Mahmood Qureshi[2], Naseer Ahmed[3**], Sheeraz Mehboob[2], Syed Zahid Hussain[2**], and Muhammad Iqbal[2**]**

[1] College of Earth and Environmental Sciences, University of the Punjab, Lahore, Pakistan

[2] Pakistan Institute of Nuclear Science & Technology (PINSTECH), Nilore, Islamabad, Pakistan

[3] Institute of Geology, University of The Punjab, Lahore, Pakistan

Abstract: A locally fabricated electrokinetic remediation apparatus was used for laboratory scale electrokinetic remediation of aqueous phase Cr and associated metals in coarse silty clay soil affected by waste effluents released from leather tanning factory located in the jurisdictions of Sambrial Town (Punjab), Pakistan. Acetic acid (0.1 M CH_3COOH: pH = 3.9 and EC = 0.4 mS/cm at the start of the experiment) was applied as electrolyte for electrokinetic washing of aqueous phase Cr and associated metal species in field collected test soil contained in an electrolytic soil cell by applying a constant 30 V DC (equivalent to 1 V cm^{-1}) across the cell for a period of 216 hours (~9 days). The pH and electrical conductivity of electrolytes (catholyte and anolyte) were measured at different time intervals during the course of electro-remediation. Inductively Coupled Plasma-Optical Emission Spectrometry (ICP-OES) has been employed to determine the contents of metals like Cr, Fe, Ni, Zn, Mn, Co, Pb and Sr in the test soil. Morphological changes in the test soil were observed through scanning electron microscope in response to electrokinetic washing of the soil. It is observed that after electro-remediation soil samples show that particles segregate and surface becomes more porous. It is noted that initially pH varies and then becomes constant, whereas electrical conductivity increases with time.

Keywords: Electro-remediation, Washing, Heavy Metals, Tannery Effluents, Waste Soils, Scanning Electron Microscopy.

1. INTRODUCTION

The leather tannery is the second largest export earning sector in Pakistan [1]. At present, there are over 250 tanneries functioning mainly in the Punjab Province of Pakistan. Most of these tanneries are situated in and around Sialkot city and alongside roads leading to Sialkot from Sambrial, Pasrur, Daska, and Head Marala. Most of these tanneries are working without any proper system of waste disposal [2]. In leather tanning industry, chrome is applied in the form of Basic Chromium Sulphate (BCS). About 60-70% of this chrome is reported to be absorbed by the hides and skins during process and the remaining is discharged as waste. The tannery effluents (wastewater) are reported to have Chemical Oxygen Demand (COD) values between 3800 mg/L to 41300 mg/L in contrast to the COD limit of 150 mg/L imposed by the National Environmental Quality Standards (NEQS) for the tannery wastewater [3]. The tannery effluents (wastewater) quality analysis along Sambrial-Sialkot road in the past for a range of parameters involving pH (3.1-3.4), COD (609-3413 mg/L), total dissolved solids (6456-91972 mg/L), and toxic metals including Cr (220-2877 mg/L) has clearly indicated an alarming soil contamination by effluents of leather tanning industry in the area [1, 3]. The continuous use of the contaminated potable groundwater (drinking water), causes various types of diseases, that are increasing rapidly and over 70% citizens are reportedly suffering from stomach and liver diseases, 60% from dysentery and 85% from stomach diseases in these areas [4]. The

---

Received: October 2023; Revised: April 2025; Accepted: June 2025

[*] Corresponding Author: Maria Khalid <mariaartandcrafts21@gmail.com>

[**] Retired from respective institutions.

tannery effluents are, therefore, held responsible for the serious pollution threat to the soil-water and subsoil water adjacent to leather tanning industrial sites. It is feared that if adequate remedial measures are not taken promptly, the inhabitants living in the vicinity of tannery waste sites may eventually develop diseases like cancer and tuberculosis.

With the advances in waste soil remediation technology, the conventional procedures such as flushing of waste soil by water admissible suitable solvents, and/or bioremediation are now being recognized as ineffective and costly tools for on-site remediation of contaminated soils [5]. In contrast, electro-kinetic decontamination process (also called electro-remediation process) has emerged as a very promising technology for on-site decontamination of aqueous phase/leachable toxic species of a variety of contaminants including metals, radionuclides, organics from wastewater environment (e.g., contaminated ponds, sub-soil environment specially, low hydraulic permeability soils like clayey soils). The electro-kinetic remediation process utilizing the electro-kinetic phenomenon was initially reported way back in the beginning of eighteenth century [6-8]. During the past fifty years, the process of electro-remediation has been extensively studied, upgraded and effectively utilized for decontamination of a variety of waste soils, particularly the clayey soils hosting inorganic contaminants such as toxic metal ions etc. [1, 2], organic contaminants [9, 10], and radionuclides such as thorium and radium [11-14].

From practical view point, for electro-kinetic washing of contaminants from soil or water environment, it is necessary that these contaminants are present in the soil-water environment in ionic or nonionic form within the soil-water environment or these can be brought into aqueous phase using chelating agents for movement across the electrolytic soil geometry. The electro-kinetic process is actuated by applying low DC voltage or current across a set of two or more electrode systems installed at suitable depths and locations in a specific geometry across the contaminated soil geometry, whereby the ionic and nonionic contaminant species are transported to respective electrodes (anode or cathode) under the influence of DC voltage gradient across electrodes. As such, the electro-kinetic decontamination is actuated by the following three processes:

(i) The electrically induced (i.e., electrolytic) migration of ionic, non-ionic and/or polar contaminant species through the pore fluids in a soil-water environment as well as the transport of hydrogen ions (H^+) generated at the anode and the hydroxyl (OH^-) generated at the cathode toward opposite electrodes. Accordingly, the temporal migration of an acid front from the anode to the cathode is, therefore, an important feature of the electro-kinetic washing/remediation procedure in the contaminated soil-water systems [5-7, 15, 16].

(ii) Electro-osmosis, i.e., displacement of smaller significant layers of water molecules due to migration of ions toward an electrode in cases where the soil pore water has elevated ionic content. Significant flux of water produced by electro-osmosis may be able to move both the ionic and non-ionic species through soil-water system commonly mostly toward the cathode [17-19].

(iii) Electrophoresis, i.e., transport of charged colloids (containing contaminant species) in the soil-water environment towards electrodes for subsequent extraction above ground.

This paper documents the first ever laboratory scale electro-kinetic remediation of aqueous phase Cr and associated metal species from coarse silty clay soils in Sambrial Town affected by tannery waste effluents under the influence of low DC voltage. The key objectives of the present study are:

(i) To examine the practical efficacy and usefulness of an indigenously developed electro-remediation apparatus for laboratory scale electro-remediation of aqueous phase Cr and associated species in soil affected by effluents released from leather tanning industry in Sambrial Town.

(ii) To learn about the electro-remediation procedures and to overcome unforeseen issues that may arise during the course of electro-remediation (such as failure of DC supply across the electrochemical cell, leakage of electrochemical cell, etc.) and hinder the progress and efficiency of electro-remediation.

(iii) To quantify electro-remediation efficiencies of Cr and associated metal species in soil affected by tannery waste effluents.

2. MATERIALS AND METHODS

2.1. Soil Sampling

Coarse silty clay soil (hereafter referred to as SAMB Soil) was collected from a tannery waste effluent pond (Figure 1(a)) adjacent to Chromium Recovery Plant (Figure 1(b)), located on main Wazirabad-Sambrial-Sialkot road (Pakistan) within the jurisdiction of Sambrial Town. This plant was used for the treatment of effluents from the leather tanneries in the area.

2.2. Soil Analysis

For experimental purposes, the collected SAMB soil (Cr content: ~1054 mg/L) was sieved (Sieve No. 80, mesh size 180 µm) to attain a fine-grained soil. The morphological characteristics of the soil were determined with scanning electron microscope (Model: Leo 440I).

2.3. Metal Analysis

The concentrations of metals (Cr, Fe, Ni, Zn, Mn, Co, Pb, and Sr) in test soil sampled before and after electro-remediation process, and in aliquots of anolyte (A) and catholyte (C) sampled during the course of electroremediation were determined by Inductively Coupled Plasma-Optical Emission Spectrometry (ICP-OES/iCAP 6500 Thermo Fisher) technique.

2.4. Electro-remediation Apparatus

Figure 2 shows the locally fabricated experimental electrokinetic remediation apparatus used in the present study. The detailed schematics and design of the apparatus are given elsewhere [12, 13]. Briefly, the experimental device consisted of the following key apparatuses: (a) One electrokinetic soil cell (dimentions: 30 × 13 × 10 cm^3) and two electrolyte compartments made by 1 cm thick acrylic sheet (dimentions: 13 × 10 × 3.6 cm^3); (b) Two 1mm thick titanium (99.9% pure) plates; (c) Five Tungsten wire electrodes (length = 15 cm, thickness = 0.1 cm); (d) Two Pyrex glass reservoirs (700 mL); and (e) One DC Power Supply (100 V and 2 Amps.). The electrokinetic soil cell was sandwiched between the electrolyte compartments while the titanium plates were inserted in the electrolyte compartments and used as anode and cathode. Similarly, the Tungsten wire electrodes were interspaced across the test soil bed to measure voltage gradient in the soil cell and used as dummy electrodes to measure potential across the soil cell. The Pyrex glass reservoirs were used to supplement electrolyte solutions (anolyte and catholyte) to respective electrolyte compartments as well as to measure the water volume transported across the soil cell.

Fig. 1. Soil sampling site near Sambrial (Punjab), Pakistan (a) Waste effluent pond near plant and (b) Chrome recovery plant.

Other tools included a multi-meter used to gauge the current and voltage across the electrokinetic soil cell during the electrokinetic washing of soil; a pH meter (Model PP– 201 K); an electrical conductivity meter (Model WTW–LF 95) used to measure electrical conductivity (including H^+ ion concentration) of the electrolytes (anolyte and catholyte) and the test soil; and plastic syringes were used to extract electrolyte samples for chemical analysis and to purge the electrolytes for the purpose of homogeneity of solutions in the anolyte and catholyte compartments.

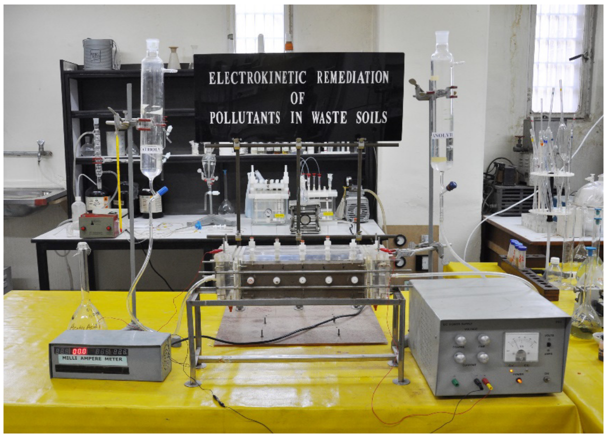

Fig. 2. Indigenous laboratory scale electrokinetic remediation apparatus.

2.5. Electroremediation Procedure

Well homogenized moist SAMB soil (weight = 4.5 kg) was gradually loaded into the electrokinetic soil cell which was then gently vibrated/shaken on table to settle the soil and to remove the trapped air. Acetic acid (0.1 M (CH_3COOH), pH = 3.9, and EC = 0.4 mS/cm at the start of experiment) was used as electrolyte both for the anolyte and catholyte compartments. About 370 mL of 0.1 M CH_3COOH was added each to the anolyte and catholyte compartments. Similarly, 0.1 M CH_3COOH was added to the electrolyte storage reservoirs. Acetic acid was used as catholyte to avoid precipitation of transported cationic species in test soil because of high pH conditions in the immediate vicinity of the cathode compartment [6]. The levels of anolyte and catholyte in electrolyte compartments and the level of soil bed across electrolytic soil cell were kept similar for hydraulic reasons. The level of acetic acid in electrolyte compartments (mainly anolyte) was maintained by adding 0.1 M CH_3COOH solution from the relevant electrolyte storage reservoirs. A zero hydraulic head was maintained across the soil cell so as to ensure, ionic transport solely due to electro-kinetic mechanism. The current across anode and cathode and the voltage between anode, cathode and dummy electrodes (D1, D2, D3, D4, and D5) was monitored [20]. The electro-remediation process was initiated by applying constant 30 V DC (equivalent to 1 V cm^{-1}) across the soil compartment for a total period of 216 hours (~9 days). During the course of electro-remediation experiment, no pH control was applied in order to simulate natural hydrogeological conditions of the contaminated site. The electrolytes in the storage reservoirs and the electrolyte compartments were purged throughout the experiment to maintain homogeneity of electrolytes therein. Similarly, the electrical conductivity and pH of both anolyte and catholyte were monitored at various time intervals during the experiment.

3. RESULTS AND DISCUSSION

3.1. Characterization of Soil

The salient mineralogical phase analyses and physicochemical of SAMB soil are summarized in Table 1. The mineralogical phase analysis shows that the SAMB test soil consists of silicate minerals, mainly SiO_2 (Quartz) and $NaAlSi_3O_8$ (Albite), and clay minerals mainly: Chamosite $[(Fe,Al,Mg,Mn)_6(Si,Al)_4O_{10}(OH)_8]$ and Muscovite $[KAl_2(AlSi_3O_{10})(OH)_2]$. Moderate contents of clay minerals namely Muscovite and Chamosite, and significantly high contents of Quartz show that the SAMB soil represents texture of coarse silty clay soil. Further, the fair proportion of Chamosite in the test soil gives a swelling character to the SAMB soil. The physicochemical analysis shows that the SAMB soil with pH = 6.72 is slightly acidic which might be due to the impact of acidic effluents from the close-by leather tanning factory in the soil sampling zone. The electrical conductivity of the test soil is 3.85 mS/cm which shows high proportion of soluble mineral contents. The bulk density of the test soil is 1.064 g/cm^3, while its specific gravity ranges from 1.87 to 1.93 which is quite low. Similarly, the moisture content of the test soil is also very low (θ = 8.4%). The porosity of the test soil ranges between 31.9% to 36.6% which is on the high soil porosity, reflecting large inter-granular spaces in the coarse silty clay soil which is also quite visible in SEM images of the SAMB soil. The acidic buffering capacity of the test soil ranges between 0.33 mM/g to 1.77 mM/g which is mildly on the lower side. In general, soils containing high contents of exchangeable ions like Ca, Mg, Na, and Al possess high buffering capacity. The moderately

Table 1. Physicochemical characteristics of experimental soil (SAMB Soil).

Analysis Type	**Value**
Mineralogical Phases	**% of bulk soil**
Quartz (SiO_2)	74 - 77
Albite ($NaAlSi_3O_8$)	4.7 - 13
Chamosite $[(Fe,Al,Mg,Mn)_6(Si,Al)_4O_{10}(OH)_8]$	04 - 5.9
Muscovite $[KAl_2(AlSi_3O_{10})(OH)_2]$	07 - 11.6
Physicochemical	
Cr content mg/L	1054
pH	6.72
Moisture Content (%)	8.4
Bulk Density (g/cm^3)	1.064
Porosity (%)	31.9 - 36.6
Specific Gravity	1.87 - 1.93
Organic Content (%)	0.43 - 0.64
Acidic Buffering Capacity (mM/g)	0.33 - 1.7
Electrical Conductivity (mS/cm)	3.85

low buffering capacity of SAMB soil signifies that the test soil may slightly impede to the production and/or transport of acidic front throughout the electro-kinetic remediation process.

3.2. SEM Analysis

Figure 3 shows the SEM images of SAMB soil before and after electro-remediation. It is observed that before electro-remediation, the particles are well connected and have larger grain size (Figure 3(a)). However, after electro-remediation, the clay morphology changes, the particles are segregated and porosity is increased size (Figure 3(b)). This could be due to the washing of soil with 0.1 M CH_3COOH (acetic acid: pH = 3.9), there may be some dissociation of clay minerals in the test soil resulting in partial destruction of some of the soil particles and/or precipitation of mineral phases at low soil pH, thereby altering the morphological nature of the soil particles.

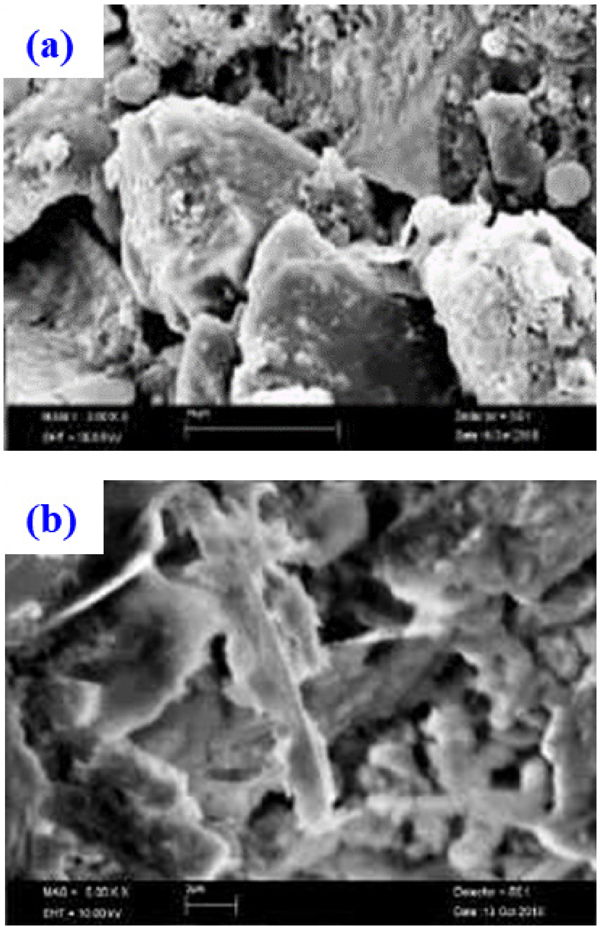

Fig. 3. SEM images of SAMB soil (a) before electroremediation and (b) after electroremediation.

3.3. Variations in the Electrolytes pH and Electrical Conductivity

The overall variations in the pH and electrical conductivity (EC) of the electrolytes (0.1 M CH_3COOH with initial pH = 3.9 and EC = 0.4 mS/cm) in the catholyte and the anolyte compartments during the course of electro-kinetic washing of SAMB soil in the electro-kinetic cell are illustrated in Figure 4 and Figure 5, respectively. Interestingly, the rate of decrease or increase in the pH of electrolytes was quite rapid during the first 20-25 hours of electro-remediation process and after this the pH kept almost constant till the experiment was terminated [1].

Figure 5 shows a rise in the electrical conductivity of catholyte from 0.4 mS/cm up to 28.8 mS/cm was observed during the course of electro-remediation. Whereas, the anolyte electrical conductivity increased from 0.4 mS/cm to 22 mS/cm during electro-remediation.

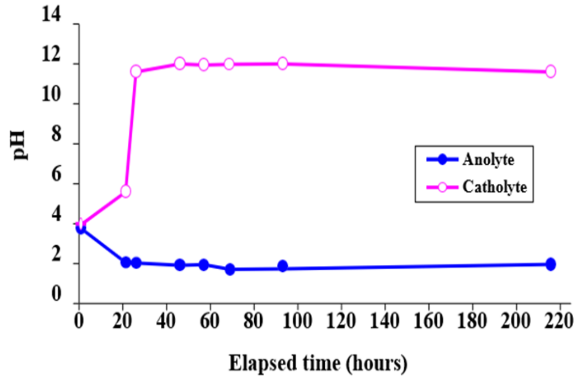

Fig. 4. Temporal variations of pH of catholyte and anolyte with time.

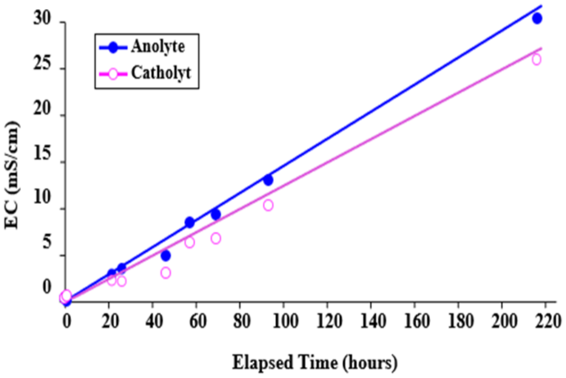

Fig. 5. Temporal variation of electrical conductivity of catholyte and anolyte.

It is observed that electrical conductivity of both anolyte and catholyte increased with time, that might of due to the accumulation of metallic ions in both electrolyte compartments.

3.4. Transport of Contaminant Across the Electrolytic Soil Cell

Both anolyte and catholyte were initially colorless. However, during the process of electro-remediation, the color of anolyte and catholyte changed along with occurrence of osmotic flow. The change in color of electrolytes depended upon the type of species received at respective electrolyte compartments. The change in color of electrolytes and the occurrence of osmotic flow from the anolyte compartment to the catholyte compartment in fact provided an indication of successful electro-kinetic washing of the soil matrix. Throughout the experiment, the anolyte colour constantly changed. Approximately, after 22 hours of electrokinetic washing, the color of the anolyte turned to yellow. After 24 hours of the electrokinetic washing, the color of the anolyte turned to dark red. After 30 hours of the electrokinetic washing, the color of the anolyte turned to slightly violet; while after 48 hours it turned to reddish colour and ultimately to green color towards the end of experimentation with a corresponding decrease in pH from 3.9 to 1.95. Likewise, after 22 hours of electro-remediation, slight yellowish turbidity was noticed in the catholyte compartment. After 26 hours of electro-remediation, the yellowish turbidity turned to deep yellowish red. With the progression of electro-remediation experiment, a yellow precipitate started settling at the bottom of the catholyte compartment and towards the end of the electro-remediation experiment, the catholyte solution started becoming colorless again with a change in pH from 3.9 to 11.6.

The heavy metals like Co, Cu, Ni, Pb, Cd, etc. may coexist with Cr within the contaminated aquatic and/or hydrogeological system in the form of cationic species [9, 21-23]. Figure 6 shows the variation in the concentrations of Cr, Fe, Ni, Zn, Mn, and Co in anolyte, measured during the course of electro-remediation of SAMB soil. It may be observed that Fe, Cr and Ni were more efficiently remediated at anode as compared to Mn and Zn. The remediation efficiency of Fe was much higher as compared to Cr and Ni. In contrast, no appreciable concentration of the metal ions, Cr, Mn, Ni, Pb, Sr, and Zn were detected in the catholyte compartment during the course of electro-remediation. This may also be attributed to precipitation of these metals as different mineral phases in the catholyte compartment in response to increasing trend of pH during the first 20-25 hours of electro-remediation process.

Although, in the present investigations, Cr species were not analyzed/quantified chemically, it is important to reiterate the Cr redox chemistry to address the observed major transport of Cr towards the anolyte compartment (anode side) as compared to the feeble transport of Cr towards the catholyte compartment (cathode side). The kinetics and redox chemistry of chromium in terms of its distribution, speciation, and transformation in the saturated/unsatuarated contaminated posrous media (soils and aquifer sediments) have been extensively addressed by several researchers [24-30]. In nature, Cr is found to exist in valence states ranging from -2 to +6. However, in the subsurface soil-water environment, Cr is found to exist in the form of cationic species or anionic species depending upon its valence states +3 [Cr(III)/trivalent chromium] and +6 [Cr(VI)/hexavalent chromium] [40]. Further, Cr(VI) is found to be much highly mobile as compared to Cr(III); due to existence of Cr in the above mentioned two different forms within the subsurface soil-water environment, the electromigaration of Cr in clayey soils can be quite a complex phenomenon [22]. For example, in the subsurface environment, naturally occurring substances like organic matter, sulfides, and ferrous iron may donate electrons and therefore, reduce hexavalent Cr to trivalent Cr. In laboratory scale electro-remediation of clays contaminated

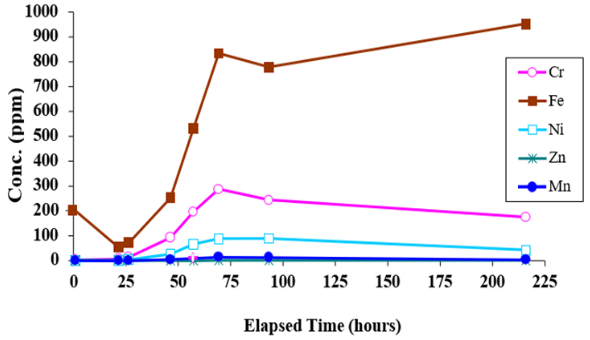

Fig. 6. Temporal variations in the concentration of metal ions in anolyte.

with electroplating wastes like Cr, Cd, and Ni, the transport of Cr(VI)/hexavalent chromium towards anode was attributed to be very much dependent on the soil type, soil mineralogy as well as presence of iron oxides in the soil [6, 9, 21, 22]. Depending upon the pH and redox conditions, Cr(VI) may exist as soluble oxyanions specifically in the form of hydrochromate ($HCrO_4^-$), dichromate ($Cr_2O_7^{2-}$) and chromate (CrO_4^{2-}) that remain in solution over a fairly wide range of pH and that these species can migrate towards anolyte compartment/anode during the electro-remediation process [25, 26, 31].

Reddy and Chinthamreddy [22] demonstrated that under applied electric field, the anionic hexavalent Cr species get easily migrated towards anolyte compartment/anode due to low adsorption of hexavalent Cr on to soil surfaces over a fairly wide range of pH. However, the cationic trivalent Cr species migrate a bit slowly towards the catholyte compartment due to higher adsorption of trivalent Cr and its precipitation as Cr(III) hydroxyl solids under slightly acidic to fairly alkaline conditions. The cationic trivalent Cr species such as $Cr(OH)^{2+}$, $Cr(OH)_2^+$ have been reported to exist over a wide range of low pH/acidic conditions and at comparatively low redox potentials, and that these may migrate towards cathode during the electro-kinetic remediation [7, 32]. At higher pH, Cr(III) precipitates as its hydroxides [$Cr(OH)_3$] between pH of 6.8 and pH of 11.3, while at higher pH values, the cationic trivalent Cr species may form anionic hydroxo-complexes like $Cr(OH)_4^-$, and $Cr(OH)_5^{2-}$ that may transport towards anode. It has also been reported that the reduction of chromium from Cr(VI)/hexavalent chromium to Cr(III)/trivalent chromium may occur before the process of electro-kinetic washing of soil depending upon amount and the type of reducing agents present in the soil [21, 32].

Reddy and Chinthamreddy [21] and Saleh *et. al* [24] have extensively discussed the impact of soil geochemical composition on electro-migration of Cr species. These researchers reported that in the presence of humic acid, minimum reduction of Cr(VI) to Cr(III) occurred, whereas in the presence of sulfides, maximum reduction of hexavalent Cr to trivalent Cr was found to occur and therefore, the presence of sulfides significantly retarded the electro-migration of hexavalent Cr due to reduction of Cr (VI) to Cr(III) as well as due to increase in the soil pH. In addition, the naturally occurring organic matters, ferrous iron, and sulfides in the subsurface soil environment may contribute/donate electrons and reduce hexavalent Cr to trivalent Cr, the extent of which depends upon prevailing geochemical conditions such as pH, redox potential, etc., as well as on the type and concentration of reducing agent(s)/ligands [21, 24]. Kim *et al*. [29] also reported Chromium(VI) reduction by Hydrogen Sulfide in aqueous media. In experimental studies of hexavalent Cr reduction by the organic matter in various types of soils, it was reported that Cr(VI) reduction was higher in low pH soils [27]. Laboratory investigations on hexavalent Cr reduction in different subsoils containing small amounts of Fe(II) and organic matter revealed that only acidic subsoils caused reduction of hexavalent Cr [26]. The rate of reduction of Cr(VI) to Cr(III) was found to increase with decrease in pH below 4. Under acidic conditions, the reduction of Cr(VI) by Fe(II) and by organic matter were equally important. It was also reported that depending on pH, the Cr(VI) reduction in acidic subsoils also resulted in the precipitation of $(Fe,Cr)(OH)_3$(am). The type of subsoil material, the content and the form of Fe as well as the solid to solution ratio may pose significant effect on the reduction of hexavalent Cr [27, 33]. Laboratory investigations revealed that Cr(VI) may be reduced in the presence of Mn^{2+} at pH values higher than 7.2 [27]. The reduction of anionic Cr(VI) to cationic Cr(III) species may be caused to various extents by different reducing agents present in the soil/water environment. In a sandy aquifer, about 30% of Cr(VI) was found reduced to Cr(III) [28]. Lastly, as mentioned earlier, mostly, heavy metals like Pb, Cd, Ni, Co, Cu, Cr, etc. may coexist in the form of cationic species within a specific contaminated hydrogeological system and that depending upon the soil type, there may be synergistic effects of co-existing Ni(II) and/or Cd(II) on removal of Cr(VI) [21, 33].

4. CONCLUSIONS

In the present study bench scale electrokinetic remediation experiment on SAMB soil collected besides tannery waste effluent pond in Sambrial town (Punjab Province, Pakistan) has been investigated. The electrokinetic remediation efficiency for Cr and associated metals such as Cu, Fe, K, Mn, Ni, Pb and Zn was established through mass balance calculations using the contents of these metals in the SAMB test soil contained within the electrolytic cell before and after electroremediation. Cr was mainly detected in the anolyte compartment and it was quite feebly detected in the catholyte compartment. This shows that Cr was present in the test soil in the form of Cr(VI) as well as Cr(III) depending upon the redox of the cell during the course of experiment. It is presumed that the reduction of Cr(IV) into Cr(III) might have been triggered by the presence of reducing agents like Mn and Fe, changes in redox conditions within the test soil (due to significant changes in the pH and redox potentials at the electrodes owing to electrolysis reactions under the influence of applied electric field); and soil moisture contents, which ultimately retarded the transport of Cr(III) due to high pH conditions in soil in the vicinity of catholyte compartment. It is concluded that further experimentation is recommended to identify the most appropriate recipe for efficient removal of Cr and associated contaminants from tannery waste affected soils such as in Sambrial (Pakistan) in a cost effective and environmentally safe manner.

5. ACKNOWLEDGEMENTS

Financial support provided by the Higher Education Commission (HEC), Islamabad to Ms. Maria Khalid facilitated accomplishment of field sampling, laboratory scale electro-remediation studies and metal analysis in soil and aqueous electrolyte samples in connection with PhD studies at the Institute of Geology as well as College of Earth & Environmental Sciences, University of the Punjab, Lahore, Pakistan. Metal analysis and SEM analysis at CAF Division and Physics Division, respectively, PINSTECH are gratefully acknowledged.

6. CONFLICT OF INTEREST

The authors declare no conflict of interest.

7. REFERENCES

1. G.J. Hashmi, G. Dastageer, M.S. Sajid, Z. Ali, M.F. Malik, and I. Liaqat. Leather Industry and Environment: Pakistan Scenario. *International Journal of Applied Biology and Forensics* 1(2): 20-25 (2017).
2. M. Sikander, L. Kumar, S.A. Naqvi, M. Arshad, and S. Jabeen. Sustainable practices for reduction of environmental footprint in tanneries of Pakistan. *Case Studies in Chemical and Environmental Engineering* 4: 100161 (2021).
3. The Gazette of Pakistan. (Extraordinary published by Authority), Islamabad, Pakistan (August 29, 1993). Part-II Statutory Notification [S.R.O 742(I)/93]. *Government of Pakistan, Ministry of Environment, Local Government and Rural Development Notification, Islamabad, the 24th August 1993*. Registered No. M-302/L.7646. (1993). https://fwegb.gov.pk/wp-content/uploads/2021/12/SRO742-I93-SRO1023-I95-NEQS.pdf
4. M.K. Daud, M. Nafees, S. Ali, M. Rizwan, R.A. Bajwa, M.B. Shakoor, M.U. Arshad, S.A.S. Chatha, F. Deeba, W. Murad, I. Malook, and S.J. Zhu. Drinking Water Quality Status and Contamination in Pakistan. *BioMed Research International* 2017: 7908183 (2017).
5. U. Michael-Igolima, S.J. Abbey, and A.O. Ifelebuegu. A systematic review on the effectiveness of remediation methods for oil contaminated soils. *Environmental Advances* 9: 100319 (2022).
6. K.R. Reddy, M. Asce, and S. Chinthamreddy. Enhanced Electrokinetic Remediation of Heavy Metals in Glacial Till Soils Using Different Electrolyte Solutions. *Journal of Environmental Engineering* 130: 442-455 (2004).
7. Y.B. Acar, R.J. Gale, A.N. Alshawabkeh, R.E. Marks, S. Puppala, M.Bricka and R. Parkar. Electrokinetic remediation: basics and technology status. *Journal of Hazardous Materials* 40(2): 117-137 (1995).
8. Y. Wang, A. Li, and C. Cui. Remediation of heavy metal-contaminated soils by electrokinetic technology: Mechanisms and applicability. *Chemosphere* 265: 129071 (2021).
9. K.R. Reddy and U.S. Parupudi. Removal of chromium, nickel and cadmium from clays by in-situ electrokinetic remediation. *Journal of Soil Contamination* 6(4): 391-407 (1997).
10. T. Vengris, R. Binkiene, and A. Sveikauskaite. Electrokinetic remediation of lead-, zinc- and cadmium-contaminated soil. *Journal of Chemical Technology and Biotechnology* 76: 1165 (2001).
11. K.H. Kim, S.O. Kim, C.W. Lee, M.H. Lee, and K.W. Kim. Electrokinetic processing for the removal of radionuclides in soils. *Journal of Separation Science and Technology* 38(10): 2137-2163 (2003).
12. M. Khalid, R.M. Qureshi, and N. Ahmed. Step toward electrokinetic remediation of contaminated soils in Pakistan. *The Nucleus* 44(1-2): 11-17 (2007).
13. M. Khalid, N. Ahmed, and R.M. Qureshi. Laboratory scale electrokinetic remediation of hexavalent chromium from contaminated soil. *The Nucleus* 45(1-2): 55-61 (2008).
14. P.V. Sivapullaiah, B.S.N. Prakash, and B.N. Suma.

Electrokinetic removal of heavy metals from soil. *Journal of Electrochemical Science and Engineering* 5(1): 47-65 (2015).

15. J. Hamed, Y.B. Acar, and R.J. Gale. Pb(II) removal from kaolinite by electrokinetics. *Journal of Geotechnical Engineering* 117(2): 241-271 (1991).
16. S. Pamukcu and J.K. Wittle. Electrokinetic removal of selected heavy metals from soil. *Environmental Progress* 11(3): 241-249 (1992).
17. A.P. Shapiro, P.C. Renaud, and R.F. Probstein. Preliminary Studies on the Removal of Chemical Species from Saturated Porous Media by Electro-Osmosis. *Physico Chemical Hydrodynamics* 11(5): 785-802 (1989).
18. C.J. Bruell, B.A. Segall, and M.T. Walsh. Electro-osmotic removal of gasoline hydrocarbons and TCE from clay. *Journal of Environmental Engineering* 118: 68-83 (1992).
19. G.R. Eykholt and D.E. Daniel. Impact of system chemistry on electro-osmosis in contaminated soil. *Journal of Geotechnical Engineering, ASCE* 120(5): 797-815 (1994).
20. M. Villen-Guzman, J.M. Paz-Garcia, J.M. Rodriguez-Maroto, C. Gomez-Lahoz, and F. Garcia-Herruzo. Acid Enhanced Electrokinetic Remediation of a Contaminated Soil using Constant Current Density: Strong vs. Weak Acid. *Separation Science and Technology* 49: 1461-1468 (2014).
21. K.R. Reddy and S. Chinthamreddy. Electrokinetic remediation of heavy metal-contaminated soils under reducing environments. *Waste Management* 19(4): 269-282 (1999).
22. K.R. Reddy and S Chinthamreddy. Effects of initial form of chromium on electrokinetic remediation in clays. *Advances in Environmental Research* 7(2): 353-365 (2003).
23. D. Rai, L.E. Eary, and J.M. Zachara. Environmental chemistry of chromium. *Science of the Total Environment* 86(1-2): 15-23 (1989).
24. F.Y. Saleh, T.F. Parkerton, R.V. Lewis, J.H. Huang, K.L. Dickson. Kinetics of chromium transformations in the environment. *Science of the Total Environment* 86(1-2): 25-41 (1989).
25. L.E. Eary and D. Rai. Chromate reduction by subsurface soils under acidic conditions. *Soil Science Society of America Journal* 55(3): 676-683 (1991).
26. James B.R. Hexavalent chromium solubility and reduction in alkaline soils enriched with chromate ore processing residue. *Journal of Environmental Quality* 23(2): 227-233 (1994).
27. T. Henderson. Geochemical reduction of hexavalent chromium in the trinity sand aquifer. *Groundwater* 32(3): 477-486 (1994).
28. A. Ugaz, S. Puppala, R.J. Gale, and Y.B. Acar. Electrokinetic soil processing: Complicating features of electrokinetic remediation of soils and slurries: Saturation effects and the role of the cathode electrolysis. *Chemical Engineering Communication* 129: 183-200 (1994).
29. C. Kim, Q. Zhou, B. Deng, E.C. Thornton, and H. Xu. Chromium(VI) Reduction by Hydrogen Sulfide in Aqueous Media: Stoichiometry and Kinetics. *Environmental Science & Technology* 35(11): 2219 (2001).
30. D.A. Brose and B.R. James. Hexavalent Chromium Reduction by Tartaric Acid and Isopropyl Alcohol in Mid-Atlantic Soils and the Role of Mn(III,IV) (hydr)oxides. *Environmental Science & Technology* 47(22): 12985 (2013).
31. E.R. Lindgren, M.W. Kozak, and E.D. Mattson. Electrokinetic remediation of unsaturated soils. In: Emerging Technologies in Hazardous Waste Management IV. D.W. Tedder and F.G. Pohland (Eds.). *American Society Symposium Series, Washington, DC, USA* pp. 33-50 (1994).
32. S. Chinthamreddy. Geochemical characterization and enhanced mobilization of heavy metals during electrokinetic remediation of soils. Ph.D. Dissertation. *University of Illinois at Chicago, Chicago, USA* (1999).
33. R.M. Powell, R.W. Puls, S.K. Hightower, and D.A. Sabatini. Coupled iron corrosion and chromate reduction: Mechanisms for subsurface remediation. *Environmental Science and Technology* 29(8): 1913-22 (1995).

Proceedings of the Pakistan Academy of Sciences: A Physical and Computational Sciences 62(2): 175-191 (2025)
Copyright © Pakistan Academy of Sciences
ISSN (Print): 2518-4245; ISSN (Online): 2518-4253
http://doi.org/10.53560/PPASA(62-2)690

Pakistan Academy of Sciences

Research Article

A New Parametrization Framework for Dark Energy and Total Cosmic Fluid

Chandrahasan Sivakumar*

Department of Physics, Maharaja's College, Ernakulam (Affiliated to MG University, Kottayam), Kerala, India

Abstract: A novel parametrization of the Equation of State (EoS) for a dynamic dark energy is introduced and its consequences in cosmology including the late time transition from a decelerating expansion to an accelerating expansion of the universe are investigated. We introduce a simple parametrization of EoS for the dynamic dark energy using a smooth sigmoid function that contains a transition redshift (z_t) at which a switch over in the dynamics of the universe observed to be occurred. The present parametrization involves three model parameters ω_0, ω_m and Δ constrained by the observational values of cosmological parameters from recent cosmological data. This EoS model introduces a continuous and smooth transition between matter-dominated and dark energy-dominated epochs as well. Such a parametrization enables dark energy to influence the late time cosmic dynamics of the universe without disturbing the early expansion dynamics involving cosmic microwave background radiation of the universe. We formulate the corresponding Friedmann theoretical framework through cosmological parameters like Hubble parameter, density parameter and deceleration parameter. It is then generalised to the total effective EoS parameter by the same function. By performing an analytical study of the cosmological parameters, the proposed model is compared with the standard cosmological model. The constraints derived for the sigmoid-based phenomenological dark energy parametrization describes its wide applicability to dynamic dark energy models that account for late-time cosmic acceleration and the overall evolution of the universe.

Keywords: Equation of State, Flat Universe, Effective Pressure Parameter, Dark Energy, Sigmoid Function.

1. INTRODUCTION

The late-time accelerated expansion of the universe, marked by a transition around redshift $z \sim 0.57$ has been firmly established by a range of observational evidence, including Type Ia supernovae (SN Ia) [1, 2], large-scale structure surveys [3], and cosmic microwave background (CMB) anisotropies [4]. These findings have fundamentally transformed our understanding of cosmic dynamics. In response, cosmologists have adopted two major approaches to explain this phenomenon. The first involves modifying the gravitational sector of general relativity while keeping the matter sector unchanged, leading to a class of models collectively known as modified gravity theories [5-13]. The second approach introduces a hypothetical but observationally motivated component called dark energy (DE) [14-16], which is thought to drive the accelerated expansion. Observations suggest that this acceleration is a relatively recent development, becoming significant at $z < 0.6$ [1, 2], thereby altering the evolution of the universe during the matter-dominated era. This behaviour challenges the conventional view of gravity as a purely attractive force, implying the need for new physics beyond our current understanding to explain the recent observation of accelerated expansion of the universe. Identifying the true nature of dark energy, still lacking direct observational evidence or definitive theoretical grounding, remains one of the most profound challenges in modern cosmology. Within a formal phenomenological framework, the recent accelerated expansion of the universe can be accounted for by introducing an effective negative pressure into the Friedmann equations. The most straightforward and widely used approach involves incorporating a positive cosmological constant (Λ)

Received: April 2025; Revised: May 2025; Accepted: June 2025

* Corresponding Author: Chandrahasan Sivakumar <sivakumar@maharajas.ac.in>

into Einstein's field equations, leading to the well-known Lambda Cold Dark Matter (ΛCDM) model [14-16]. In this context, dark energy is typically characterized by an equation of state (EoS) parameter, defined as the ratio of pressure to energy density given by $\omega = \frac{p}{\rho c^2}$. For acceleration, ω should be less than $-\frac{1}{3}$. Dark energy models are broadly classified based on whether the equation of state (EoS) parameter is constant or time-dependent. The most widely accepted model, ΛCDM, assumes a constant EoS with $\omega = -1$ and a constant energy density ρ, but it suffers from two significant theoretical issues: the fine-tuning problem [17, 18] and the cosmic coincidence problem [19, 20]. The fine-tuning problem arises from the vast discrepancy between the observed value of the cosmological constant Λ and the much larger value predicted by quantum field theory. The coincidence problem refers to the puzzling fact that, although matter and dark energy evolve differently over time, their energy densities are of the same order of magnitude in the present epoch, a situation often referred as the "why now?" question in cosmology. On the observational front, tensions have emerged between the predictions of the ΛCDM model and recent data, including analyses from the Planck 2018 mission [21], particularly regarding the current value of the Hubble parameter. Additionally, new low-redshift observations suggest that ΛCDM may not provide an accurate description of the late-time universe [22, 23]. These challenges have motivated the development of alternative models - particularly dynamic dark energy models - where the EoS parameter evolves with time (as in quintessence models), offering a better fit to observational data and addressing the limitations associated with the standard ΛCDM model.

A wide variety of dynamical dark energy (DE) models have been proposed in the literature, including quintessence [24-26], k-essence [27, 28], and Chaplygin gas models [29, 30]. In the present work, a novel sigmoid-type parametrization for the dark energy equation of state (EoS) is proposed and examined as a valuable tool for analysing the behaviour of dark energy and describing the expansion dynamics of the universe.

To investigate the characteristics of dark energy and its influence on cosmic evolution, parameterized models of the equation of state (EoS) have proven to be very effective. These models describe the evolution of dark energy through a set of phenomenological model-parameters that describe its behaviour across different cosmic epochs. By constraining these parameters using the latest observational data, one can assess the advantages of such models over the ΛCDM framework and gain deeper insights into the fundamental physics driving the recent accelerated expansion of the universe. A wide range of EoS parameterizations has been proposed in the literature, including the Chevallier-Polarski-Linder (CPL) model [31, 32], the Jassal-Bagla-Padmanabhan (JBP) model [33], logarithmic forms [34], and Pade approximants such as Pade (I) and Pade (II) [35], all aimed at explaining the dynamics of dark energy and the late-time evolution of the universe. The underlying idea is to formulate the EoS as a function of the scale factor or redshift and determine the model parameters through observational fitting. Alternatively, one can derive a suitable parametric form directly from observational data. Several recent efforts have explored dynamically evolving dark energy and modified gravity approaches to address the issues of cosmic acceleration and Hubble tension [36-40].

In the present paper, former approach is used, in which a new parametric DE equation of state is proposed and investigated. It is a 3-parameter model for ω as a function of scale factor or redshift z. The model is guided by the observation of recent acceleration at around $z \sim 0.5$ and other cosmological parameters like present value of deceleration parameter $q_0 \sim -0.5$ and $\omega_p \sim -0.6$ to -0.8. The new parametrization in the present paper is proposed to overcome the poor behaviour of ω in other mostly used parametrization models in the literature. It is a smooth sigmoid like model given by:

$$\omega(a) = \omega_m + \frac{\omega_0 - \omega_m}{1 + \exp((a_t - a)/a a_t \Delta)} \tag{1}$$

Where parameters ω_m and ω_0 represents asymptotic values of ω in the early and late epochs. a_t is a measure of transition epoch between deceleration and acceleration. Δ may be called a control parameter. It helps the smooth transition between different evolutionary phases of the universe. Apart from the density parameter Ω, the model parameters - ω_m, ω_0 and Δ are set by recent observational data and can be further fine-tuned with more accurate cosmic data. It is further proposed that applying this parametrized equation of state to the total cosmic fluid with many components offers valuable insights into the structure of the universe's evolutionary dynamics and history. The model presented here shows good agreement with current observational data and illustrates the importance of treating dark energy as a dynamically evolving component intrinsic to the fabric of space-time, rather than as a simple constant. This perspective not only addresses key shortcomings of the ΛCDM model but also provides a natural mechanism for driving the recent phase of cosmic acceleration through the emergence of negative pressure. Moreover, the proposed model can be easily incorporated within the Friedmann theoretical framework. Further comparisons with other recent models will be explored in future work.

In the present research work, the cosmological implications of a parametrized equation of state (EoS) for dark energy (DE) and the total fluid are analysed using observational values of relevant cosmological parameters [41, 42]. The study aims to explain the transition from a decelerated to an accelerated expansion of the universe, as well as its significance for the future dynamics of the universe.

2. METHODS AND MATHEMATICAL FORMULATION

The standard cosmological model, widely regarded as the most successful theoretical framework for describing the evolution of the universe and exhibiting strong consistency with observational data, is governed by the Friedmann equations derived from Einstein's gravitational field equations [43]:

$$R_{ik} - \frac{1}{2} g_{ik} R = -\frac{8\pi G}{c^4} T_{ik} \tag{2}$$

Where, R_{ik} is the Ricci tensor, g_{ik} is the metric tensor, R is the Ricci scalar and T_{ik} is the energy momentum tensor. Assuming the validity of the cosmological principle, that the three-dimensional space is maximally symmetric, even in the presence of a dynamic dark energy component, the background geometry of the universe is described by the standard Friedmann Lemaître Robertson Walker (FLRW) metric, which in polar coordinates is given by Narlikar [44],

$$ds^2 = c^2dt^2 - a(t)^2\left[\frac{dr^2}{1-kr^2} + r^2\left(d\vartheta^2 + \sin^2\vartheta d\phi^2\right)\right] \tag{3}$$

Where k is the space curvature parameter. $k = 0$ for flat universe, $k = +1$ for closed universe with positive curvature and $k = -1$ for open universe with negative curvature. In this study, the universe is assumed to be spatially flat, an assumption well supported by observational evidence from the cosmic microwave background (CMB), large-scale structure surveys, and predictions from inflationary cosmology [45]. The scale factor, denoted by a(t), is a time-dependent function that plays a central role in understanding the universe's dynamics within the Friedmann framework. It quantifies the expansion of space-time over time and is directly related to the observable redshift z. By convention, the scale factor is normalized such that $a(t_0) = 1$ at the present epoch. The rate of change of the scale factor is characterized by another fundamental cosmological parameter, the Hubble parameter, defined by $H(t) = \frac{\dot{a}}{a}$ This parameter describes the expansion rate of the universe and can be measured from the apparent magnitude-redshift data of standard candles like Type Ia supernovae.

To describe the dynamics of the universe, use above metric into Einstein's field equations, with energy content as that of a perfect fluid characterized by the divergence-less energy-momentum tensor

$$T_{ik} = (\rho c^2 + p)u_i u_k + p g_{ik} \tag{4}$$

Here ρc^2 is the total energy density, p is the total pressure and u_i is the 4-velocity vector of the perfect cosmic fluid. It leads to Friedmann equations:

$$\frac{\dot{a}^2}{a^2} + \frac{kc^2}{a^2} = \frac{8\pi G\rho(t)}{3} \tag{5}$$

$$2\frac{\ddot{a}}{a} + \frac{\dot{a}^2}{a^2} + \frac{kc^2}{a^2} = -\frac{8\pi Gp(t)}{c^2} \tag{6}$$

and

$$\frac{\ddot{a}}{a} = -\frac{4\pi G}{3c^2}(\rho c^2 + 3p) \tag{7}$$

The first Friedmann equation represents the expansion rate (velocity) of the universe. The second and third Friedmann equations govern whether the cosmic expansion accelerates or decelerates, depending on the sign of the term

$\rho c^2 + p$. In the realistic cosmological model, the total energy density ρ is composed of the sum of multiple components-radiation, matter (normal and dark) and DE (Λ or varying). So total energy density ρ composed of ρ_r of radiation, $\rho_{m(n)}$ of normal matter, $\rho_{m(d)}$ of dark matter and ρ_d of dark energy, which currently contribute approximately 0%, 5%, 25%, and 70% of the total energy density, respectively [46]. Usually, the equation of state that is needed to solve Friedman equations is written as $p = \omega\rho c^2$, ω is called equation of state parameter, $\omega = \frac{1}{3}$ for radiation, $\omega = 0$ for matter and $\omega = -1$ for cosmological constant. It varies between 0 and -1 for varying or dynamic dark energy. The universe expands with deceleration when the equation of state parameter satisfies $\omega > -\frac{1}{3}$, and with acceleration when $\omega < -\frac{1}{3}$ and uniformly when $\omega = -\frac{1}{3}$. Moreover, applying the energy conservation law, $dU + pdV = 0$, separately to each component of the cosmic fluid leads to a scaling relation for energy density given by $\rho \propto a^{-3(1+\omega)}$. $\rho \propto a^{-4}$ for radiation, $\rho \propto a^{-3}$ for normal matter, $\rho = \text{constant}$ for dark energy with $\omega = -1$, and it varies with time for dynamic DE as in the present work which is explored in the next section. The relative abundance of these components in the fluid determines the expansion history of the universe. Early universe is radiation dominated, followed by matter domination (deceleration). A phase shift occurred at about 5 billion years ago, to an accelerating expansion and ρ is dominated by DE at present epoch.

To compare the predictions of the model with observational values of cosmological parameters, cosmological redshift is defined and related to the scale factor by:

$$1 + z(t) = \frac{a(t_0)}{a(t)} = \frac{1}{a} \tag{8}$$

So, the Hubble parameter becomes

$$H(z) = -\frac{1}{1+z}\frac{dz}{dt} \tag{9}$$

The acceleration or deceleration of the expansion rate of the universe is characterized in cosmology by the dimensionless deceleration parameter q, which is defined by

$$q = -\frac{a\ddot{a}}{\dot{a}^2} \tag{10}$$

In terms of z

$$q(z) = -1 + \frac{1+z}{H}\frac{dH}{dz} \tag{11}$$

q must be negative, if present expansion is accelerating. This means that at some epoch the deceleration parameter must undergo a change of sign in any acceptable cosmological model. The transition point of the universe from decelerating phase to accelerating phase is characterized by a null value of q. The corresponding redshift (z_t) is the transition redshift.

3. THE NEW PARAMETRIZATION

Type Ia supernova observations have provided compelling evidence that the universe transitioned from a decelerating phase to an accelerating one roughly five billion years ago. In the standard ΛCDM framework, this late-time acceleration is attributed to a cosmological constant (Λ), characterized by a fixed equation of state parameter ω = -1. However, many alternative theories suggest that a dynamic equation of state may offer a more realistic description of the universe's evolving expansion rate. Present-day observational data indicate that dark energy-a mysterious component exerting negative pressure-constitutes about 70% of the universe's total energy density. The remaining 30% is composed of non-relativistic matter, which includes both ordinary (baryonic) matter and dark matter.

The dark energy component is typically characterized by its equation of state (EoS) parameter ω, defined by, $\omega = \frac{p}{\rho c^2}$. While the cosmological constant with cold dark matter (ΛCDM) model remains consistent with many current observations, numerous alternative models have been proposed in the literature that predict a dynamically evolving EoS. Among the numerous dynamical dark energy models, notable examples include quintessence, where dark energy emerges from a time-evolving scalar field, and barotropic models, in which the pressure is explicitly defined as a function of the energy density [47]. Given the overwhelming variety of such models, it has become both practical and insightful to classify them through simple parametrizations of the equation of state parameter ω. The most basic approach assumes a constant ω; however, aside from the special case ω = -1, such constant values rarely align with physically well-motivated models. Furthermore, a constant EoS often yields misleading or inaccurate cosmological predictions, particularly when compared to models where ω varies with time [48]. Consequently, attention has shifted to more flexible formulations-most commonly two-parameter models-where ω evolves as a function of either the scale factor a or redshift z. Among these, the Chevallier-Polarski-Linder (CPL) parametrization stands out, describing ω as a linear function of the scale factor, namely: $\omega(a) = \omega_0 + \omega_a(1\text{-}a)$. In terms of redshift, it becomes $\omega(z) = \omega_0 + \omega_a \frac{z}{1+z}$ where ω_0 and ω_a are constants. The Jassal-Bagla-Padmanabhan (JBP) Parametrization: $\omega(z) = \omega_0 + \omega_a \frac{z}{(1+z)^2}$ is better at early epochs where it evolves slowly. In CPL, the early and late-time limits are fixed: $\omega(z = 0) = \omega_0$, $\omega(z \rightarrow \infty) = \omega_0 + \omega_a$. No flexibility for more general asymptotics. If this is not set to 0 (matter-like), it may give unrealistic early universe behaviour. In JBP as well, at $z \rightarrow \infty$, $\omega(z) \rightarrow \omega_0$. So, no way to model matter-like behaviour in early universe unless $\omega_0 = 0$. Looking for new models (like sigmoid/tanh/Gaussian) allow better control over transition scale, sharpness, and asymptotic behaviour. We expect the transition from deceleration to acceleration is a smooth process, not necessarily linear or polynomial. In this manuscript, we explore a smooth sigmoid form for the effective EoS parameter as a function of redshift.

We define the effective equation of state parameter $\omega(a)$ as: $\omega(a) = \omega_m + \frac{\omega_0 - \omega_m}{1 + e^{(\frac{a_t - a}{a a_t \Delta})}}$. In terms of redshift z, it becomes:

$$\omega(z) = \omega_m + \frac{\omega_0 - \omega_m}{1 + e^{(\frac{z - z_t}{\Delta})}} \qquad (12)$$

Where, ω_0 is the asymptotic value of ω(z) at low redshift (present epoch), ω_m is the asymptotic value at high redshift (matter-dominated era, typically $\omega_m \approx 0$). z_t transition redshift, when ω(z) transitions from ω_m to ω_0. Δ represents the transition width, which governs the gradualness or sharpness of the change.

To get an idea regarding the variation of ω as a function of z, for different set of model parameter values, ω(z) is plotted against z for different transition redshifts in Figure 1 and Figure 2.

At high redshift of early epoch, $z \gg z_t$, $\omega(z) \rightarrow \omega_m$, behaves like matter ($\omega_m = 0$). At low redshift, $z \ll z_t$, $\omega(z) \rightarrow \omega_0$ and can represent dark energy domination if it is negative. For instance, if it is -1, it corresponds to dark energy in the form of cosmological constant. The model naturally allows a smooth transition around $z = z_t$, matching supernova observations. The derivative of $\omega(z)$ is given by:

$$\frac{d\omega}{dz} = \frac{(\omega_m - \omega_0)}{\Delta} \frac{e^{(\frac{z - z_t}{\Delta})}}{(1 + e^{\frac{z - z_t}{\Delta}})^2} \qquad (13)$$

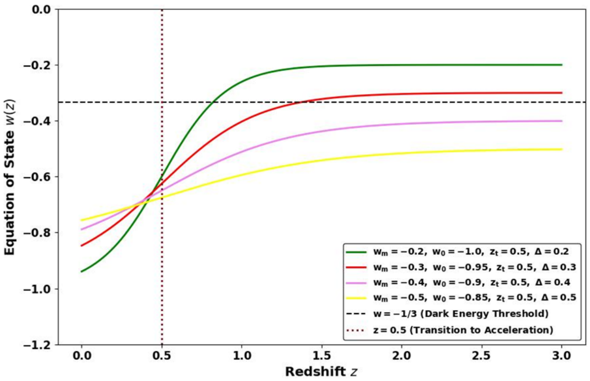

Fig. 1. Equation of state parameter is plotted as a function of redshift for a transition redshift of 0.5.

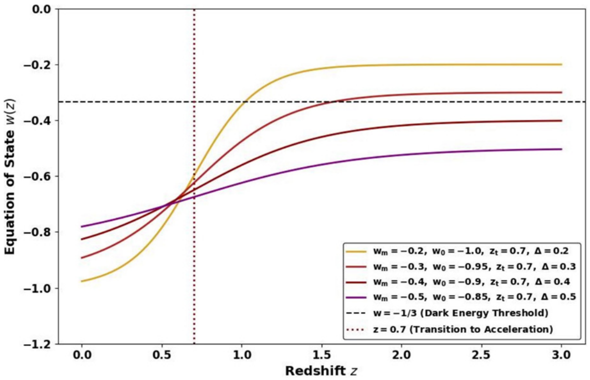

Fig. 2. Equation of state parameter is plotted as a function of redshift for a transition redshift of 0.7.

This derivative peaks at $z = z_t$, indicating the maximum rate of change - a physically meaningful feature. This parametrization is not linear or polynomial (like CPL/JBP) and avoids divergence or high-z inconsistencies and characterised by physically intuitive parameters: early-time state, late-time state, transition redshift, and smoothness. Also, it can be derived from some scalar field dynamics with sigmoid-type potentials (if needed) and is expanded (e.g., double sigmoid or asymmetric sigmoid) for more complex behaviour.

The Friedmann equations incorporating the new sigmoid model for the dark energy equation of state ω(z) is formulated and then apply the same parametrization to the total or effective equation of state parameter defined by $\omega_{eff}(z) = \frac{P_{tot}(z)}{\rho_{tot}(z)c^2}$. This will allow us to track how the expansion rate H(z) evolves and explain the transition from deceleration to acceleration in the universe's history. The cosmological scale factor a is related to the redshift z due to the expansion of the universe, by, $a(z) = \frac{1}{1+z}$ Present scale factor is normalised to one. If the space time geometry is flat as suggested by recent observations, then Friedmann velocity equation is

$$H^2 = \frac{8\pi G}{3}\rho(a) \tag{14}$$

$\rho(a)$ representing the energy density of all the components contributing to the stress-energy tensor including radiation, matter (baryonic and dark) and dark energy.

$$\rho = \rho_r + \rho_m + \rho_d \tag{15}$$

One can arrive at the continuity equation either from Friedmann equations or the energy conservation law for each component separately as

$$\dot{\rho} = -3H(\rho + \frac{P}{c^2}) \tag{16}$$

With the equation of state $P_i = \omega_i \rho_i c^2$, above equation can be solved to give

$$\rho_i \propto a^{-3(1+\omega_i)} \tag{17}$$

In terms of redshift

$$\rho_i(z) \propto (1+z)^{3(1+\omega_i)} \tag{18}$$

ω_i for radiation, matter and cosmological constant is $\frac{1}{3}$, 0 and -1 respectively. In this work, however a dynamic dark energy term is introduced in the total energy density rather than a cosmological constant to better suit the recent observation and to get rid of the notorious cosmological problems. Introducing the critical density for the flat universe as $\rho_c = \frac{3H_0^2}{8\pi G}$, Friedmann equations can be rearranged as:

$$H^2 = H_0^2 \sum_i \frac{\rho_{0i}}{\rho_c} h_i(z) \tag{19}$$

Here '0' stands for present epoch. 'i' stands for various components in energy density and h_i represent the dependence on redshift for various components in energy density. For dark energy term, we are using the time dependent equation of state parameter, ie., $\omega_d = \omega_d(a) = \omega_d(z)$ in the continuity equation to solve. If we further introduce the density parameter $\Omega_i = \frac{\rho_i}{\rho_c}$, Hubble parameter for flat model is represented as:

$$H^2(z) = H_0^2[\Omega_r(1+z)^4 + \Omega_m(1+z)^3 + \Omega_d.\exp\left(3\int_0^z \frac{1+\omega(z')}{1+z'}dz'\right)] \tag{20}$$

To evaluate that exponential term using our new sigmoid ω(z) model, let

$$I(z) = \int_0^z \frac{1+\omega(z')}{1+z'}dz' \tag{21}$$

Substitute for $\omega(z)$,

$$I(z) = (1+\omega_m)\ln(1+z) + (\omega_0 - \omega_m)I_s(z) \tag{22}$$

where,

$$I_s(z) = \int_0^z \frac{1}{(1+z')(1+e^{\frac{(z'-z_t)}{\Delta}})}dz' \tag{23}$$

Hence,

$$H^2(z) = H_0^2[\Omega_r(1+z)^4 + \Omega_m(1+z)^3 + \Omega_d.(1+z)^{3(1+\omega_m)}.\exp(3(\omega_0 - \omega_m)I_s(z))] \tag{24}$$

This is not reducible to a simple power law, unlike CPL-type models. Making it genuinely new and distinct. One can numerically integrate above equation using a standard computational tool. To compute the transition redshift, deceleration parameter ($q(z)$) to be evaluated in such a way that the switch over corresponds to $q(z) = 0$.

The deceleration parameter is

$$q(z) = -\frac{\ddot{a}}{aH^2} = -1 + \frac{(1+z)}{H(z)}\frac{dH}{dz} \tag{25}$$

If we introduce the normalised Hubble parameter as

$$E^2(z) = \frac{H^2}{H_0^2} = \Omega_r(1+z)^4 + \Omega_m(1+z)^3 + \Omega_d.(1+z)^{3(1+\omega_m)}.\exp(3(\omega_0 - \omega_m)I_s(z)) \tag{26}$$

$$q(z) = -1 + \frac{(1+z)}{2E^2(z)}\frac{dE^2(z)}{dz} \tag{27}$$

After some simplifications, deceleration parameter is evaluated for the present model as

$$q(z) = -1 + \frac{1+z}{2E^2}[4\Omega_r(1+z)^3 + 3\Omega_m(1+z)^2 + D(z)(\frac{3(1+\omega_m)}{1+z} + \frac{3(\omega_0 - \omega_m)}{(1+z)(1+e^{\frac{z-z_t}{\Delta}})})] \tag{28}$$

Here,

$$D(z) = \Omega_d(1+z)^{3(1+\omega_m)}.\exp[3(\omega_o - \omega_m).I_s(z)] \tag{29}$$

The proposed parametrisation for dark energy can be very well fit with the recent observational data.

If we use the best fit values of present deceleration parameter as $q_0 = -0.56$ and transition redshift $z_t \sim 0.5$, the following plot (Figure 3) will be obtained which shows the variation of deceleration parameter over redshift:

The density parameters chosen here is $\Omega_r = 0$, $\Omega_m = 0.3$ and $\Omega_d = 0.7$. $\omega_m = -0.21$, $\omega_0 = -0.60$ and $\Delta = 0.26$. Another similar plot if $z_t = 0.7$ is given in Figure 4.

Another important parameter in analysis of cosmological models is the cosmic age parameter due to the associated cosmic age problem with this parameter. Expansion age of the universe is given by,

$$t_0 = \int_0^a \frac{da}{\dot{a}} = \int_0^a \frac{da}{aH(a)} \tag{30}$$

In terms of redshift z,

$$t_0 = \int_0^{\infty} \frac{dz}{(1+z)H(z)} = \int_z^{\infty} \frac{dz}{(1+z)H_0\sqrt{\Omega_r(1+z)^4 + \Omega_m(1+z)^3 + D(z)}} \tag{31}$$

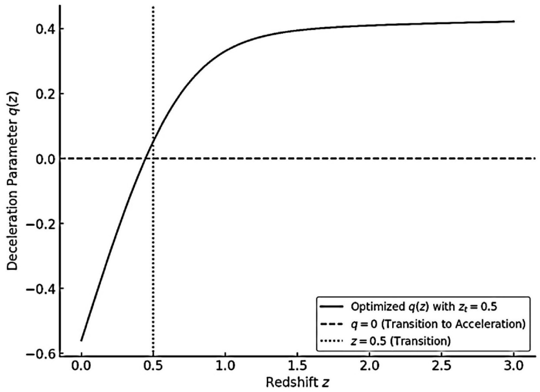

Fig. 3. Variation of the deceleration parameter as a function of redshift for a transition redshift of 0.5.

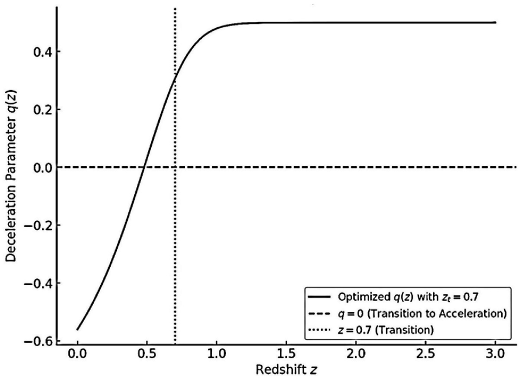

Fig. 4. Variation of the deceleration parameter as a function of redshift for a transition redshift of 0.7.

To get the present age of the universe, set $z = 0$, and upper limit as say, 1000. With $H_0 = 68$ Km/s/Mpc, $\omega_0 = -0.72$, $\omega_m = -0.08$, $\Delta = 0.45$, $z_t = 0.65$, present age of the universe is evaluated as 13.7 billion years. Corresponding deceleration parameter is $q_0 = -0.56$. Thus, it finds a value of cosmic age which is close to standard model and in this regard, the age problem is not relevant in the present model. Fine tuning can be done with more accurate cosmological data.

If we treat $\omega(z)$ not just as a property of dark energy, but as the effective equation of state parameter of the total cosmic fluid (matter + radiation + dark energy). The effective equation of state parameter governs the overall expansion dynamics of the universe, encapsulating all components:

$$\omega_{eff}(z) = \frac{p}{\rho} \tag{32}$$

p and ρ as total pressure and energy of cosmic fluid. So, Hubble parameter from Friedmann equations becomes,

$$H^2(z) = \frac{8\pi G}{3}\rho(z) \tag{33}$$

Conservation of energy of total fluid leads to:

$$\rho(z) = \rho_0(1+z)^{3(1+\omega_m)}.\ \exp[3(\omega_0 - \omega_m)I_s(z)] \tag{34}$$

Hence Hubble parameter is:

$$H^2(z) = H_0^2.\exp\left(3\int_0^z \frac{1+\omega_{eff}(z')}{1+z'}dz'\right) \tag{35}$$

With the present parametrization:

$$H^2(z) = H_0^2(1+z)^{3(1+\omega_m)}\ .\ \exp(3(\omega_0 - \omega_m)I_s(z)) \tag{36}$$

And q(z) directly related to effective ω parameter by, $q = \frac{1}{2}(1+3\omega_{eff}(z))$.

Hence,

$$q(z) = \frac{1}{2}\left[1+3\left(\omega_m + \frac{\omega_0-\omega_m}{1+e^{\frac{z-z_t}{\Delta}}}\right)\right] \tag{37}$$

At high redshifts ($z \gg 1$), $\omega_{eff} \approx \omega_m = 0$, so $q = \frac{1}{2}$, corresponding to a matter-dominated universe. At transition redshift z_t, $q \approx 0$ (switch from deceleration to acceleration). At present time ($z = 0$), if $\omega_0 \approx -1$, then $q(z) \approx -1$, matching observations. Figure 5 illustrates this.

This Figure 5 represents the variation of deceleration parameter q(z) as a function of redshift. The transition redshift $z_t = 0.5$, marks the switch from deceleration (q > 0) to acceleration (q < 0), and at present epoch (z = 0), q ≈ −1 (case of cosmological constant dominated), as expected. If we set $\omega_0 = -0.7$, the variation of q(z) is shown below in Figure 6.

The transition from deceleration to acceleration occurs around $z \approx 0.5$, and at $z \approx 0$, q ≈ −0.56, matching with recent observations. For the present parametrization, one can compute the cosmic age at redshift z as,

$$t(z) = \int_z^{\infty} \frac{dz'}{(1+z')H_0\sqrt{(1+z')^{3(1+\omega_m)}\exp(3(\omega_0-\omega_m)I_s(z'))}} \tag{38}$$

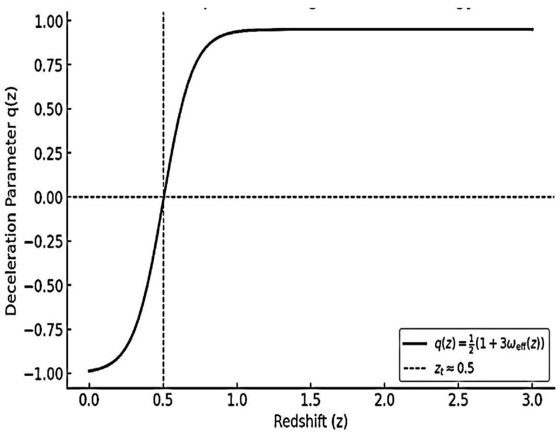

Fig. 5. Deceleration parameter versus redshift for a transition redshift of 0.5 and ω_0, -1.

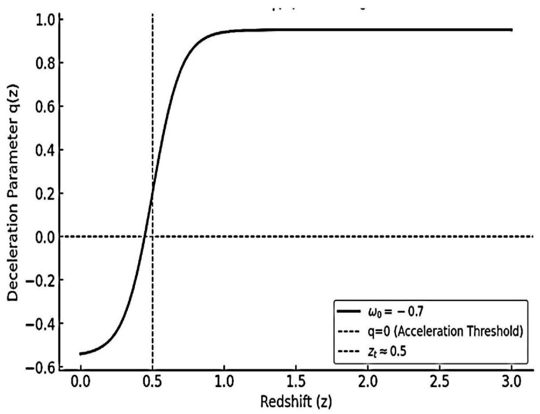

Fig. 6. Deceleration parameter versus redshift for a transition redshift of 0.5 and ω_0, -0.7.

Also, the observationally significant luminosity distance is:

$$d_L(z) = \frac{(1+z)}{H_0}\int_0^z \frac{dz'}{E(z')} \tag{39}$$

Where, the normalised Hubble parameter is:

$$E(z) = \sqrt{\exp(3\int_0^z \frac{1+\omega_{eff}(z')}{1+z'}dz')} \tag{40}$$

3.1. Comparison with Existing Dark Energy Parametrizations

Over the years many DE parametrized equation of state models is proposed to study the late cosmic acceleration, notably the Chevallier-Polarski-Linder (CPL), Jassal-Bagla-Padmanabhan (JBP), logarithmic and Pade-type DE models. Eventhough, these models offer varying degree of simplicity and observational compatibility, they also suffer from many drawbacks, especially in terms of controlling the transition behaviour, high-redshift divergence and future phantom behaviour. However, the sigmoid-based parametrization introduced in the present work offers a flexible, smooth observationally consistent approach to model the transition from a decelerating phase to an accelerating phase. In the present model, the parameters ω_m and ω_0 define the equation of state in the early and late universe, respectively. This makes the model compatible with matter-dominated behaviour ($\omega \approx 0$) at high redshift and dark energy domination ($\omega < -\frac{1}{3}$) at low redshift, consistent with recent observations. This leads to tunable asymptotic limits in the present proposed model. The parameter z_t specifies the redshift at which the transition occurs. The width parameter Δ offers an explicit control over the sharpness or smoothness of this transition. This is not possible in CPL or JBP parametrizations, which implicitly set this behaviour. This controlled transition epoch and width is an important point in the present model. The sigmoid form ensures a smooth and differentiable evolution of $\omega(z)$, free from breaks or cusps, and it avoids divergences at high redshift, a common issue in logarithmic models. Also, by adjusting the parameters, the model can closely match the observed values of the deceleration parameter $q_0 \sim -0.56$, transition redshift $z_t \sim 0.5 - 0.6$, and cosmic age ~13.7 Gyr, while maintaining consistency with Planck 2018 data and H(z) observations.

3.2. Comparison with Existing Sigmoid Type Models

Sigmoid-type equations of state have previously been proposed in the literature as smooth, physically plausible alternatives to more traditional parametrizations such as CPL or JBP. A typical example involves tanh-based or logistic function-based transitions designed to capture the gradual shift from matter like behaviour to dark energy dominance. John et al [49] proposed tanh-based transitions of the form $\omega(z) = \omega_0 + \omega_1 \tanh\left(\frac{z - z_t}{\Delta}\right)$ Such models often lack explicit control over asymptotics and not structured for observational fitting beyond low redshift expansions. Escamilla *et al.* [37] analysed multiple sigmoid inspired EoS forms in light of cosmic data concluding that such smooth models may provide transitions but are under constrained unless tied to physically meaningful parameters. Unlike tanh or fixed logistic models, the proposed model allows free adjustment of both early-time (ω_m) and late-time (ω_0) EoS values. This is in alignment with structure formation constraints at high redshift and late time acceleration behaviour. The control parameter Δ is a direct measure of the steepness of the transition. In contrast, tanh-based models often hide the transition scale within an amplitude parameter, making it comparatively less observationally viable. Also, in the present scenario, the sigmoid form is also used to describe the total effective equation of state, capturing both matter like and dark energy like epochs in a unified framework. The statistical analysis for fitness is performed in the following section. The model also guarantees a smooth evolution of cosmic pressure and sound speed, without the instabilities or divergences sometimes seen in other non-analytic parametrizations.

3.3. Scalar field and Theoretical Origins of the Sigmoid Form

An alternative and equally meaningful interpretation lies in reconstructing the model in terms of a canonical scalar field with a slowly varying potential V(φ). The smooth evolution of ω(z), makes it consistent with a thawing quintessence scenario, wherein the scalar field remains frozen at early times and begins to roll down its potential only in the recent cosmological past. This class of models is particularly appealing for avoiding early-time deviations from ΛCDM while offering dynamical features at late times that are testable with high-precision data. Scalar field models, such as quintessence and phantom fields, provide a bridge between cosmology and high-energy physics, and offer a physically transparent mechanism for dynamical dark energy. While our proposed model, defined by the redshift-dependent equation of state for ω(z), has so far been analysed phenomenologically, it is crucial to investigate whether this parametrization can be realized within a self-consistent scalar field theory. Such a reconstruction not only enhances the physical interpretability of the model but also embeds it within a broader theoretical framework that encompasses inflationary dynamics, scalar-tensor theories, and effective field theories of gravity. A scalar field description of dark energy offers a fundamental and field-theoretic perspective, where cosmic acceleration arises dynamically from a self-interacting field evolving in a potential. Any viable equation of state ω(z) can, in principle, be reproduced by an appropriate choice of the scalar field kinetic function ω(φ) and potential V(φ). Here, we construct a scalar field theory in which our proposed redshift-dependent dark energy EoS emerges naturally. The phenomenological sigmoid equation of state discussed in this work not only provides an excellent fit to observational data but also points at a deeper theoretical origin. In this section, it is demonstrated that the smooth evolution of $\omega(z)$ can naturally arise from the dynamics of a scalar field rolling in a logistic type potential. Quintessence models in their canonical form, describe dark energy as a slowly evolving scalar field φ, minimally coupled to gravity by matter, with its dynamics governed by a potential $V(\phi)$. For suitable choices of $V(\phi)$, the field evolves gradually from a kinetic energy-dominated (matter-like) phase at high redshift to a potential dominated (accelerating) phase at low redshift. A class of such potentials that produce sigmoid-like evolution in the equation of state are logistic-potentials:

$$V(\varphi) = \frac{1}{1+e^{\lambda\varphi}} \tag{41}$$

We show in the following derivation that our proposed sigmoid, $\omega(z)$ can be reproduced by assuming a monotonic mapping between redshift z and field value φ, leading to this logistic form. This strengthens the physical viability of the sigmoid model within a scalar field framework. We start with minimally coupled scalar field φ with energy density and pressure,

$$\rho_\phi = \frac{1}{2}\omega(\phi)\dot{\phi}^2 + V(\phi) \tag{42}$$

And

$$p_\phi = \frac{1}{2}\omega(\phi)\dot{\phi}^2 - V(\phi) \tag{43}$$

$$\omega_\phi(t) = \frac{p_\phi}{\rho_\phi} = \frac{\omega(\phi)\dot{\phi}^2 - 2V}{\omega(\phi)\dot{\phi}^2 + 2V} \tag{44}$$

Solving for $\dot{\phi}^2$ and $V(\phi)$ in terms of ω_ϕ and ρ_ϕ:

$$\dot{\phi}^2 = (1+\omega_\phi)\rho_\phi \tag{45}$$

$$V(\phi) = \frac{1}{2}(1-\omega_\phi)\rho_\phi \tag{46}$$

Now, assume a sigmoid form for $\omega(z)$ as in the present model. Change the independent variable from redshift z to scalar field ϕ by assuming $z = z(\phi)$. Let us assume that the redshift is monotonically related to ϕ via:

$$\phi(z) = \phi_0 + \frac{1}{\lambda}\ln\left(1+e^{\frac{z-z_t}{\Delta}}\right) \tag{47}$$

Using this, one can rewrite the sigmoid as a function of φ as:

$$\omega(\phi) = \omega_0 + \frac{\omega_m - \omega_0}{e^{\lambda(\phi-\phi_0)}} \tag{48}$$

Using the relation for potential, and assume a constant or slowly varying $\rho_\phi \sim \rho_0 e^{-3(1+\bar{\omega})\ln a}$ or treat ρ_ϕ approximately a constant during slow roll for qualitative understanding,

$$V(\phi) \propto 1 - \omega(\phi) = 1 - \left[\omega_0 + \frac{\omega_m - \omega_0}{e^{\lambda(\phi-\phi_0)}}\right] \tag{49}$$

So,

$$V(\phi) \approx \frac{A}{1+e^{\lambda(\phi-\phi_0)}} \tag{50}$$

A logistic potential. By expressing the cosmic dynamics encoded in the equation of state for ω(z) in terms of a minimally coupled scalar field with a self-interaction potential, we establish a concrete connection between phenomenological parametrizations and fundamental field dynamics. The reconstructed field exhibits quintessence-like behaviour, evolving down a gradually decaying logistic potential capable of driving late-time acceleration without invoking phantom instabilities or future singularities. The width parameter Δ in the proposed model represents the phenomenological characteristic of the time scale over which the unknown energy becomes dominant in the evolution history of the universe. In scalar field dynamics, it reflects the steepness or flatness of the logistic potential, analogous to how the slow-roll parameters control inflationary dynamics. A steeper potential for smaller Δ corresponds to a sharp transition and a flatter evolution for a smaller Δ, which corresponds to a rather gradual evolution. In scalar field theories, the speed of the transition is determined by the gradient of the potential. A steep potential causes the field to roll quickly causing a rapid evolution of the EoS, corresponds to a small **Δ**. In the other case, a flatter potential produces a slow-roll evolution, where the field frozen until relatively late times, yielding a larger **Δ**. Thus, this parameter is an effective characteristic which describes the ratio of the potential's curvature to the Hubble damping during the evolution of the cosmos. From a physical cause, this suggests that the transition speed is not arbitrary, but is controlled and determined by the competition between the potential force driving the scalar field and the Hubble friction opposing it. In many modified gravity theories like f(R) models, this means, the rate at which the additional scalar degree of freedom detaches from matter and starts to dominate curvature evolution.

In the present phenomenological model, **Δ** determines these effects in a single parameter. It describes how rapidly the dark energy fluid deviates from matter like behaviour and begins to accelerate the expansion. While we consider this parameter as a fit parameter, its magnitude may reflect underlying field dynamics or geometric transitions in the fundamental theory driving the late acceleration of the universe.

3.4. Early Universe Consistency

It is important that, any viable dark energy model must be consistent with established early-universe dynamics, including the era of primordial nucleo-synthesis and the formation of microwave background radiation. In the sigmoid-like evolution of the EoS, for $z \gg z_t$, the exponential term dominates and the equation of state asymptotically approaches the high redshift value, ω_m. In the present scenario, we take a very small ω_m, which ensures that dark energy behaves like pressureless matter in the early universe. This is important, since it means that the energy density of the dark energy component varies as $\rho \sim (1+z)^3$. Just like ordinary matter. This suggests that, dark energy contribution decouples from early radiation dominated phase dynamics and hence will not affect the thermal history of the early universe. Consequently, the model does not disturb the established features of conventional models, such as the abundance of light elements, nor does it alter the acoustic peaks in the microwave background power spectrum. Unlike some dark energy models, this feature confirms that the proposed parametrization is in accordance with early universe dynamics and become significant around the transition epoch.

4. STATISTICAL ANALYSIS WITH COSMIC CHRONOMETERS

A reliable assessment of any dynamical dark energy model requires direct confrontation with observational data. One of the most model-independent and precise probes of the universe's expansion history is provided by measurements of the Hubble parameter H(z) derived from cosmic chronometers (CC). These data points are based on differential age techniques applied to passively evolving galaxies and offer a clean observational window into the late-time dynamics of cosmic expansion. To evaluate the observational viability of our proposed sigmoid type dark energy parametrization, we utilize a compilation of 32 recent CC measurements of H(z) spanning the redshift range $0.07 \leq z \leq 1.965$ [50]. This is given in Table 1. This redshift coverage effectively captures both the decelerated expansion era and the current acceleration phase, making it highly suitable for testing time-evolving dark energy models. We compare the performance of our model against other well-established frameworks, including the Chevallier-Polarski-Linder (CPL) and Jassal-Bagla-Padmanabhan (JBP) parametrizations, as well as the concordance ΛCDM model. The theoretical predictions for each model are evaluated through chi-square minimization, and their statistical viability is quantified using the Akaike Information Criterion (AIC), which appropriately accounts for the trade-off between goodness of fit and the number of free parameters [51, 52]. This comprehensive approach enables a transparent and quantitative comparison of competing models in light of contemporary observational data. Use

Table 1. Compilation of Hubble parameter measurements (Cosmic chronometers).

z_i	$(H \pm \sigma) km/s/Mpc$
0.07	69.0 ± 19.6
0.09	69.0 ± 12.0
0.12	68.6 ± 26.2
0.17	83.0 ± 8.0
0.179	75.0 ± 4.0
0.199	75.0 ± 5.0
0.2	72.9 ± 29.6
0.27	77.0 ± 14.0
0.28	88.8 ± 36.6
0.352	83.0 ± 14.0
0.3802	83.0 ± 13.5
0.4	95.0 ± 17.0
0.4004	77.0 ± 10.2
0.4247	87.1 ± 11.2
0.4497	92.8 ± 12.9
0.47	89.0 ± 50.0
0.4783	80.9 ± 9.0
0.48	97.0 ± 62.0
0.593	104.0 ± 13.0
0.68	92.0 ± 8.0
0.75	98.8 ± 33.6
0.781	105.0 ± 12.0
0.875	125.0 ± 17.0
0.88	90.0 ± 40.0
0.9	117.0 ± 23.0
1.037	154.0 ± 20.0
1.3	168.0 ± 17.0
1.363	160.0 ± 33.6
1.43	177.0 ± 18.0
1.53	140.0 ± 14.0
1.75	202.0 ± 40.0
1.965	186.5 ± 50.4

updated cosmic chronometer data: $H_{obs}(z_i)$ with uncertainties σ_i . The chi-square is

$$\chi^2(\omega_0,\Delta,H_0,\Omega_m) = \sum_{i=1}^{32} \frac{(H_{th}(z_i;\omega_0,\Delta,H_0,\Omega_m) - H_{obs}(z_i))^2}{\sigma_i^2} \quad (51)$$

In the present analysis, we use $\omega_m = 0$, ensuring that dark energy behaves like matter at early times. The transition redshift $z_t = 0.65$ is fixed based on supernovae observations. Minimize χ^2 with respect to ω_0, Δ (and possibly H_0, Ω_m) in a flat universe, using nonlinear least squares. Best fit parameters from chi-square minimization are $H_0 = 67.64, \Delta= 0.35, \omega_0 = -0.8, \Omega_m = 0.25$. And minimum is $\chi^2_{min} = 14.74$. Reduced chi-square is $\chi_r^2 = \frac{\chi^2_{min}}{v}$, where v is the number of degrees of freedom. It is $v = 32 - 4 = 28$. So, $\chi_r^2 = 0.53$.

Figure 7 demonstrates excellent agreement between the proposed dark energy parametrization and observational data over the full redshift range $0.07 \le z \le 1.965$. The best-fit model captures the late-time acceleration while maintaining consistency with early-time expansion history, supporting its viability as a competitive alternative to ΛCDM and CPL models.

To quantitatively assess the statistical performance of each cosmological model in light of observational Hubble data, we employ the Akaike Information Criterion (AIC) [51], a model selection tool rooted in information theory. AIC provides a balance between goodness of fit and model complexity, penalizing models with more free parameters to avoid overfitting. It is defined as $AIC = \chi^2_{min} + 2k$, where k is the number of free parameters in the model. Lower AIC values indicate a more preferred model. To compare models, we compute the relative difference $\Delta AIC = AIC_{model} - AIC_{\Lambda CDM}$, which measures how much worse (or better) a model is compared to the reference ΛCDM scenario. According to standard AIC interpretation: $\Delta AIC < 2$ implies substantial support for the model; $4 < \Delta AIC < 7$ suggests considerably less support; and $\Delta AIC > 10$ indicates that the model is strongly disfavored. The best fit parameter values are chosen across all models to maintain fairness in comparison. The equation of state for each model is given by:

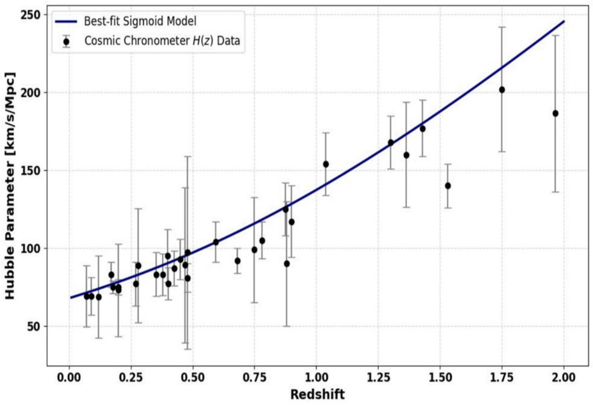

Fig. 7. Fitting the cosmic chronometer Hubble data with the present model.

Our model: $\omega(z) = \omega_m + \frac{\omega_0 - \omega_m}{1+e^{(\frac{z-z_t}{\Delta})}}$

CPL model: $\omega(z) = \omega_0 + \omega_1 \frac{z}{1+z}$

JBP model: $\omega(z) = \omega_0 + \omega_1 \frac{z}{(1+z)^2}$

ΛCDM: $\omega(z) = -1$ (constant)

and the Akaike Information Criterion:

$$AIC = \chi^2_{min} + 2k$$

where k is the number of free parameters (4 for our model, 2 for CPL and JBP, 1 for ΛCDM). The comparison table is given in Table 2.

The proposed sigmoid parametrization achieves an excellent statistical fit to the H(z) data, with a reduced χ^2 well below unity. Its AIC is competitive with CPL and JBP models and lies within the $\Delta AIC < 2$ region, indicating a good statistical support. Unlike CPL or JBP, the present model has a smooth and flexible structure with physically meaningful parameters with a progressive early-time limit, late-time EoS, sharpness and redshift of transition. This analysis confirms that the proposed sigmoid-type dark energy model is observationally competitive with current cosmological models. It provides an excellent fit to low and mid-redshift Hubble data without

Table 2. Comparison of AIC and ΔAIC with other models.

Model	χ^2_{min}	**AIC**	**ΔAIC (vs ΛCDM)**
Our DE Model	14.74	22.74	+1.67
CPL	14.34	22.34	+1.28
JBP	14.69	22.69	+1.62
ΛCDM	17.07	21.07	0 (reference)

requiring a cosmological constant or entering the phantom regime. These results further establish its potential as a viable alternative for describing late-time cosmic acceleration. In Figure 8, deceleration parameter is plotted against redshift using the fit parameter values and is in good agreement with current observations.

5. RESULTS AND DISCUSSION

In this work, a phenomenological cosmological model is developed in which cosmic fluid is many-component one. To avoid cosmological constant problem, cosmic coincidence problem etc., a dynamic dark energy is incorporated in the total energy density. Also, the EoS parameter has a crucial role in the dynamics of the universe. It has different values for matter, radiation, cosmological constant, quintessence etc. Moreover, varying EoS parameter can very much influence the expansion history of the universe including the switch over from decelerating phase to accelerating phase and fate of the universe. The present work is primarily aimed at examining how the parametrization of EoS for varying dark energy and then to total effective EoS could alleviate the shortcomings in the ΛCDM [17-20] models. The cosmological implications are investigated by formulating Friedmann equations with parametrized EoS parameter. The idea presented is a three-parameter (ω_0, ω_m and Δ) parametrization using a sigmoid type function. The model parameters are constrained by observational data. These parameters determine the EoS parameter during different evolutionary phases of universe. For example, at high redshift, the EoS parameter (effective EoS of total fluid) tends towards matter or radiation dominated era, while in the late universe, it tends to a DE dominated phase with a negative pressure. The logistic form is common in phase transition models, making it more theoretically justifiable in scenarios where dark energy behaves dynamically. The given sigmoid-type parametrization for the total equation of state (EoS): offers several advantages over commonly used parametrizations like Chevallier-Polarski-Linder (CPL) [32], Jassal-Bagla-Padmanabhan (JBP) [33], and Pade approximations [35]. The sigmoid function ensures a smooth and continuous transition between an early-time value ω_m and a late-time value ω_0. This controlled evolution is not guaranteed in CPL, JBP, or Pade parametrizations, which can lead to unrealistic extrapolations. For example, it can decay too fast at large z, affecting structure formation constraints. The transition redshift z_t and the width Δ allow fine-tuning of the evolution. This is particularly useful for modelling late-time dark energy evolution or early transition effects that CPL and JBP struggle with. Sigmoid functions are known for their ability to fit smoothly varying data, making this parametrization more suitable for describing supernovae, CMB [21], and BAO [46] constraints. The sigmoid-type parametrization is superior in terms of physical realism, numerical stability, and observational compatibility, making it a promising alternative to traditional linear models like CPL or JBP. However sigmoid models are less intuitive because the evolution depends on an exponential function rather than a simple linear or polynomial term. While the sigmoid function is useful phenomenologically, it lacks a strong derivation from fundamental physics (unlike quintessence models or specific dark energy theories). It is purely a parametric fit, rather than arising from a well-defined potential. The age of the universe is calculated using the best fit values $H_0 = 67.64, \Delta = 0.35, \omega_0 = -0.8, \Omega_m = 0.25$.

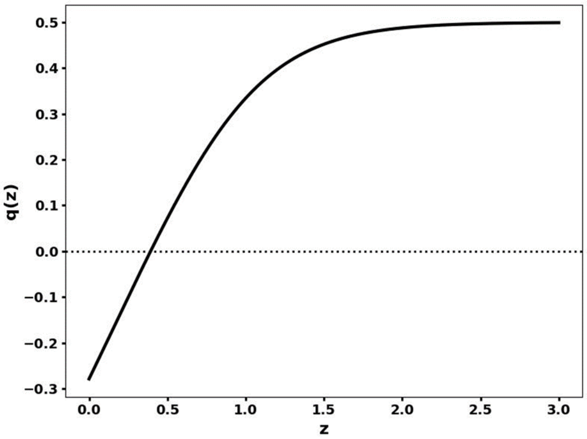

Fig. 8. Deceleration parameter versus redshift using the best fit parameters.

It is found to be 13.7 Gyr. Which is in excellent agreement with the value inferred from Plank 2018 data (t_0=13.80 ± 0.02 Gyr). This is derived using the Eq. (31). The deceleration parameter q is a crucial indicator of the expansion dynamics of the universe, helping to distinguish between decelerating and accelerating phases. In the matter dominated universe, it is positive. As DE becomes dominant, it switches over to a negative value. The present model can clearly fit with recent observational values of transition redshift $z_t \approx 0.5\text{-}0.7$, and present $q_0 = -0.5\sim -0.6$, with $\omega_0 \sim -0.80$. In the ΛCDM model, that is with matter, radiation and cosmological constant Λ, Hubble parameter is

$$H^2(z)=H_0^2[\Omega_r(1+z)^4+\Omega_m(1+z)^3+\Omega_\Lambda] \tag{52}$$

And deceleration parameter,

$$q(z)=\frac{1}{2}\frac{\Omega_m(1+z)^3+2\Omega_r(1+z)^4}{\Omega_m(1+z)^3+\Omega_r(1+z)^4+\Omega_\Lambda} \tag{53}$$

A comparison between present parametrized model and ΛCDM model almost exhibit similar behaviour, however the transition from deceleration to acceleration occurs at slightly different redshifts in the two models. The plot below (Figure 9) clearly favours a dynamically varying dark energy model, where transition redshift is ~ 0.5 and $q_0 \sim -0.5$. In the standard model, the deceleration parameter q approaches -1 as the universe evolves towards the present epoch.

The sigmoid type parametrized EoS model provides a promising theoretical framework for explaining the dynamics and evolution history of the universe, including the phase shift from deceleration to acceleration and also describes a natural and smooth dynamic evolution of a dynamic dark energy. The model effectively fit with observational data. More testing of the model and further observational constrains with data like Type Ia supernovae, BAO, CMB will be necessary to refine the model and also to refine the understanding of DE and future evolution dynamics of our universe. A thorough thermodynamic analysis of this three-parameter parametrized dark energy (DE) model remains an important avenue for future investigation. In the absence of a fundamental theory describing the true nature of dark energy, thermodynamics offers a powerful macroscopic framework. By examining the large-scale behaviour of the system without requiring knowledge of its microscopic structure, thermodynamic principles can serve as essential tools by assuming that dark energy obeys the established laws of thermodynamics. So, a thermodynamic analysis may put bounds on the parametrized dark energy.

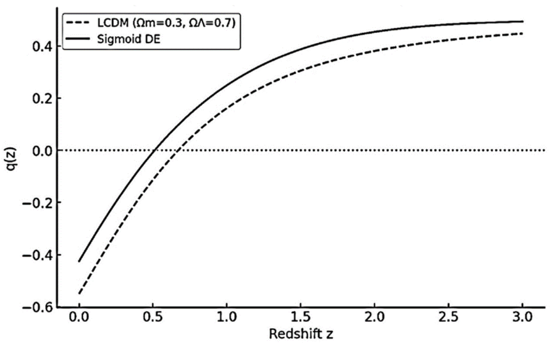

Fig. 9. Comparison of deceleration parameter versus z for present model and standard model.

5.1. Physical Interpretation and Observational Prospects

A qualitative feature of the present sigmoid-based equation of state is its smooth, controlled evolution of pressure, which not only avoids divergences at high redshift but also offers a good diagnostic tool for future cosmological observations. The model naturally mimics a slow-roll-like transition in cosmic pressure, analogous to scalar field dynamics, where a field gradually evolves from one vacuum dominated state to another, often seen in scalar field theories or thawing scenarios [53]. In such models, the dark energy component tracks the matter or radiation background until late times when it begins to dominate the cosmic expansion rate. The smoothness parameter Δ in the present model effectively controls the time scale over which the transition occurs. More significantly, the first derivative of the equation of state, $\frac{d\omega}{dz}$, exhibits a localized peak near the transition redshift z_t. This behaviour finely captures the redshift at which dark energy rapidly departs from matter like behaviour and begins to accelerate the universe. Some of the cosmological probes like Euclid, Roman Space Telescope and DESI data will provide more accurate measurements of Hubble parameter and angular diameter distance across a broad redshift range and may have the capacity to resolve such localized features in $\omega(z)$ or other parameters. Thus, the peak in $\frac{d\omega}{dz}$ may act as an observational feature of dynamical dark energy models, distinguishing them from constant ω or ΛCDM-like behaviour.

Also, the smooth pressure evolution governed by the sigmoid shape implies a continuous and stable sound speed evolution of dark energy, potentially impacting structure formation and growth index measurements. Such pressure driven deviations can be tested via weak lensing, redshift space distortions and integrated Sachs-Wolfe effect studies. Significantly, the avoidance of abrupt or oscillatory behaviour ensures that the present model does not induce artificial features in the matter power spectrum or CMB anisotropies, further supporting its viability. A detailed thermodynamic analysis will be done in future communications, which is beyond the scope of the present analysis.

6. CONCLUSIONS

In this work, a three-parameter sigmoid-type parametrization of the dark energy equation of state to model the dynamic evolution of dark energy and the cosmic fluid is developed. This formulation offers a smooth and realistic transition from matter-dominated deceleration to dark energy-driven acceleration, in close agreement with observational constraints, with best fit values such as the transition redshift $z_t \sim 0.65$, present-day deceleration parameter $q_0 \sim -0.5$ and age of the universe $t_0 \sim 13.7\ Gyr$ in agreement with Planck 2018 results. Compared to traditional models like ΛCDM, CPL, and JBP, the sigmoid parametrization demonstrates superior numerical stability, physical plausibility, and observational compatibility maintaining early universe consistency. Additionally, it has shown that this parametrization can be derived from a logistic potential within a scalar field framework, providing a possible theoretical origin. Although phenomenological in nature, it provides a robust framework to capture the essential features of cosmic expansion and the evolution of dark energy. Future work, including a detailed thermodynamic analysis and tighter observational constraints from supernovae, BAO, and CMB data, will further illuminate the viability of this model and deepen our understanding of the universe's fate.

7. ACKNOWLEDGEMENTS

The author acknowledges the Department of Higher Education and Department of Collegiate Education, Government of Kerala, for their support.

8. CONFLICT OF INTEREST

The author declares no conflict of interest.

9. REFERENCES

1. A.G. Riess, A.V. Filippenko, P. Challis, A. Clocchiattia, A. Diercks, P.M. Garnavich, R.L. Gilliland, C.J. Hogan, and *et al*. Observational evidence from supernovae for an accelerating universe and a cosmological constant. *The Astronomical Journal* 116: 1009-1038 (1998).
2. S. Perlmutter, G. Aldering, G. Goldhaber, R.A. Knop, P. Nugent, P.G. Castro, and *et al*. Measurement of Ω and Λ from 42 high redshift supernovae. *The Astrophysical Journal* 517(2): 565-586 (1999).
3. M. Tegmark, M. Strauss, M. Blanton, K. Abazajian, S. Dodelson, H. Sandvik, and *et al*. Cosmological parameters from SDSS and WMAP. *Physical Review D* 69: 103501 (2004).
4. D.N. Spergel, L. Verde, H.V. Peiris, E. Komatsu, M.R. Nolta, C.L. Bennett, and *et al.* First-year Wilkinson microwave anisotropy probe (WMAP) observations: Determination of cosmological parameters. *The Astrophysical Journal Supplement Series* 148: 175-194 (2003).
5. S.D. Odintsov and V.K. Oikonomou. Autonomous dynamical system approach for f(R) gravity. *Physical Review D* 96(10): 104049 (2017).
6. S. Capozziello, S. Nojiri, and S.D. Odintsov. The role of energy conditions in f(R) cosmology. *Physics Letters B* 781: 99-106 (2018).
7. S.D. Odintsov and V.K. Oikononou. Running of the spectral index and inflationary dynamics of f(R) gravity. *Physics Letters B* 833: 137353 (2022).
8. D. Liu and M. Reboucas. Energy conditions bounds on f(T) gravity. *Physical Review D* 86: 083515 (2012).
9. M. Zubair, A. Ditta, E. Gudekli. P. Bhar, and H. Azmat. Anisotropic compact models in f(T) gravity with Tolman-Kuchowics spacetime. *International Journal of Geometric Methods in Modern Physics* 18(04): 2150060 (2021).
10. J.B. Jimenez, L. Heisenberg, and T. Koivisto. Coincident general relativity. *Physical Review D* 98(4): 044048 (2018).
11. M. Koussour and A. De. Observational constraints on two cosmological models of f(Q) theory. *The European Physical Journal C* 83(5): 400 (2023).
12. A. Mussatayeva, N. Myrzakulov, and M. Koussour. Cosmological constraints on dark energy in f(Q) gravity: A parametrized perspective. *Physics of the Dark Universe* 42: 101276 (2023).
13. N. Myrzakulov, M. Koussour, and D.J. Gogoi. A new f(Q) cosmological model with H (z) quadratic expansion. *Physics of Dark Universe* 42: 101268 (2023).
14. M. Demianski and E. Piedipalumbo. The cosmological constant-A brief history and recent results. *Astronomy Reports* 59(6): 484-490 (2015).
15. P.J.E. Peebles and B. Ratra. The cosmological

constant and dark energy. *Reviews of Modern Physics* 75(2): 559-606 (2003).

16. T. Padmanabhan. Cosmological constant-The weight of the vacuum. *Physics Reports* 380: 235-320 (2003).
17. S. Weinberg. The cosmological constant problem. *Reviews of Modern Physics* 61: 1-23 (1989).
18. E.J. Copeland, M. Sami, and S. Tsujikawa. Dynamics of dark energy. *International Jornal of Modern Physics D* 15(11): 1753-1936 (2006).
19. I. Zlatev, L. Wang, and P.J. Steinhardt. Quintessence, Cosmic Coincidence, and the Cosmological Constant. *Physical Review Letters* 82(5): 896-899 (1999).
20. H.E.S. Velten, R.F. Vom Marttens, and W. Zimdahl. Aspects of the cosmological coincidence problem. *The European Physical Journal C* 74(11): 3160 (2014).
21. N. Aghanim, Y. Akrami, M. Ashdown, J. Aumont, C. Baccigalupi, M. Ballardini, and *et al*. Planck 2018 results VI Cosmological parameters. *Astronomy and Astrophysics* 641: A6 (2020).
22. L. Perivolaropoulos and F. Skara. Challenges of ΛCDM: An update. *New Astronomy Reviews* 95: 101659 (2022).
23. E.D. Valentino, O. Mena, S. Pan, L. Visinelli, W. Yang, A. Melchiorri, D.F. Mota, A.G. Riess, and J. Silk. In the realm of the Hubble tension-A review of solutions. *Classical and Quantum Gravity* 38(15): 153001 (2021).
24. R.R. Caldwell, R. Dave, and P.J. Steinhardt. Cosmological Imprint of an Energy Component with General Equation of State. *Physical Review Letters* 80(8): 1582-1585 (1998).
25. P.J. Steinhardt, L. Wang, and I. Zlatev. Cosmological Tracking Solutions. *Physical Review D* 59(12): 123504 (1999).
26. S. Tsujikawa. Quintessence: A Review. *Classical and Quantum Gravity* 30(21): 214003 (2013).
27. T. Chiba, T. Okabe, and M. Yamaguchi. Kinetically Driven Quintessence. *Physical Review D* 62(2): 023511 (2000).
28. C. Armendariz-Picon, V. Mukhanov, and P.J. Steinhardt. Dynamical Solution to the Problem of a Small Cosmological Constant and Late-Time Cosmic Acceleration. *Physical Review Letters* 85(21): 4438-4441 (2000).
29. M.C. Bento, O. Bertolami, and A.A. Sen. Generalized Chaplygin Gas, Accelerated Expansion, and Dark-Energy-Matter Unification. *Physical Review D* 66(4): 043507 (2002).
30. A.Y. Kamenshchik, U. Moschella, and V. Pasquier. An Alternative to Quintessence. *Physics Letters B* 511(2): 265-268 (2001).
31. M. Chevallier and D. Polarski. *International Journal of Modern Physics D* 10(2): 213-224 (2001).
32. E.V. Linder. Exploring the Expansion History of the Universe. *Physical Review Letters* 90(9): 091301 (2003).
33. H.K. Jassal, J.S. Bagla, and T. Padmanabhan. WMAP constraints on low redshift evolution of dark energy. *Monthly Notices of Royal Astronomical Society Letters* 356(1): L11-L16 (2005).
34. J.Z. Ma and X. Zhang. Probing the dynamics of dark energy with novel parametrizations. *Physics Letters B* 669(3): 233-238 (2011).
35. H. Wei, X.P. Yan, and Y.N. Zhou. Cosmological applications of Pade approximant. *Journal of Cosmology and Astroparticle Physics* 2014: 045 (2014).
36. B.R. Dinda and N. Banerjee. A comprehensive data-driven odyssey to explore the equation of state dark energy. *The European Physical Journal C* 84: 688 (2024).
37. L.A. Escamilla, W. Giare, E.D. Valentino, R.C. Nunes, and S. Vagnozzi. The state of the dark energy equation of state circa 2023. *Journal of Cosmology and Astroparticle Physics* 2405: 091 (2024).
38. J.K. Singh, P. Singh, E.N. Saridakis, S. Myrzakul, and H. Balhara. New parametrization of the dark energy equation of state with a single parameter. *Universe* 10: 246 (2024).
39. Y. Tiwari, B. Ghosh, and R.K. Jain. Towards a possible solution to the Hubble tension with horndeski gravity. *The European Physical Journal C* 84: 220 (2024).
40. G. Montani, M.D. Angelis, F. Bombacigna, and N. Carievaro. Metric f(R) gravity with dynamical dark energy as a scenario for the Hubble tension. *Monthly Notices of Royal Astronomical Society Letters* 527(1): L156-L161 (2024).
41. M. Koussour, S. Bekov, A. Syzdykova, S. Muminov, I. Ibragimov, and J. Rayimbaevetal. Observational constraints on a generalized equation of state model. *Physics of The Dark Universe* 45: 101799 (2025).
42. A. Aich. Phenomenological DE model with hybrid dynamic cosmological constant, *Classical and Quantum Gravity* 39(3): 035010 (2022).
43. A. Friedmann. On the curvature of space. *General Relativity and Gravitation* 31(12): 1991-2000 (1999).
44. J.V. Narlikar (Ed.). An Introduction to cosmology. *Cambridge University Press, Cambridge* (1993).
45. A.H. Guth. The inflationary universe: A possible

solution to horizon and flatness problems. *Physical Review D* 23(2): 347-356 (1981).

46. A.G. Adame, J. Aguilar, S. Ahlen, S. Alam, D.M. Alexander, M. Alvarez, O. Alves, A. Anand, U. Andrade, and E. Armengaud. DESI 2024 VI cosmological constraints from the measurements of Baryon acoustic Oscillations. submitted to the *Journal of Cosmology and Astroparticle Physics* 2025: 012 (2025).
47. J. Bielefeld, R.R. Caldwell, and E.V. Linder. Dark Energy Scaling from Dark Matter to Acceleration. *Physical Review D* 90(4): 043015 (2014).
48. I. Maor, R. Brustein, J. McMahon, and P.J. Steinhardt. Measuring the Equation of State of the Universe: Pitfalls and Prospects. *Physical Review D* 65(12): 123003 (2002).
49. R. John, N. Sarath, and T.K. Mathew. Thermal evolution and stability analysis of phenomenologically emergent dark energy model. *The European Physical Journal C* 83: 697 (2023).
50. S. Cao and B. Ratra. Using lower-redshift, non-CMB, data to constrain the Hubble constant and other cosmological parameters. *Monthly Notices of Royal Astronomical Society* 513: 5686 (2022).
51. S.D. Odintsov, D.S.C. Gomez, and G.S. Sharov. Modified gravity/dynamical dark energy vs ΛCDM: is the game over. *The European Physical Journal C* 85: 298 (2025).
52. H. Akaike. A new look at the statistical model identification. *IEEE Transactions on Automatic Control* 19: 716 (1974).
53. G. Gupta. S. Majumdar, and A.A. Sen. Constraining thawing quintessence. *Monthly Notices of Royal Astronomical Society* 420(2): 1309-1312 (2012).

Instructions For Authors

Manuscript Writing

The manuscript may contain a Title, Abstract, Keywords, INTRODUCTION, MATERIALS AND METHODS, RESULTS, DISCUSSION (or RESULTS AND DISCUSSION), CONCLUSIONS, ETHICAL STATEMENT (if applicable), ACKNOWLEDGEMENTS, CONFLICT OF INTEREST and REFERENCES, *and any other information that the author(s) may consider necessary*.

Title (Bold and font size 16): The title should be expressive, concise, and informative to the entire readership of the journal. It may include common terms, to make it more identifiable when people search online. Please avoid the use of long pervasive terms and non-standard or obscure abbreviations, acronyms, or symbols.

Abstract (font size 10, max 250 words)**:** Must be self-explanatory**,** stating the rationale, objective(s), methodology, main results, and conclusions of the study. Abbreviations, if used, must be defined on the first mention in the Abstract as well as in the main text. Abstracts of review articles may have a variable format.

Keywords (font size 10)**:** Provide five to eight keywords consisting of words and phrases that are closely associated with the topic depicting the article.

INTRODUCTION (font size 11)**:** Provide a clear and concise statement of the problem, citing relevant recent literature, and objectives of the investigation. Cite references in the text by number in square brackets**,** the reference must be cited in a proper English sentence [1]. or "... as previously described [3, 6–8]". For a single author: Bednorz [2] investigated the environmental pollution ... When there are only two authors: Bednorz and Allan [2] investigated the environmental pollution ... and for three or more authors: Bednorz *et al.* [2] investigated the environmental pollution ..; and list them in the REFERENCES section, in the order of citation in the text.

MATERIALS AND METHODS (font size 11)**:** Provide an adequate account of the procedures or experimental details, including statistical tests (if any), concisely but sufficiently enough to replicate the study. Relevant references to methodology must be cited.

RESULTS (font size 11)**:** Be clear and concise with the help of appropriate Tables, Figures, and other illustrations. Data should not be repeated in Tables and Figures but must be supported with statistics. The data presented in Tables and Figures must be elaborated in the main text.

DISCUSSION (font size 11)**:** Provide interpretation of the RESULTS in the light of previous relevant studies, citing published references.

CONCLUSIONS (font size 11)**:** Briefly state the implication of your study findings, and carefully address the study questions. Confine your conclusions according to the objectives of your study and the aspects covered in the abstract. Discuss both positive and negative findings.

ETHICAL STATEMENT (font size 10)**:** The statement of ethical approval by an appropriate ethics committee or review board must be included in the manuscript (if applicable), as per the Journal's policy.

ACKNOWLEDGEMENTS: (font size 10)**:** In a brief statement, acknowledge the financial support and other assistance.

CONFLICT OF INTEREST (font size 10)**:** State if there is any conflict of interest.

REFERENCES (font size 10)**:** References must be listed in numerical order as listed in the main text. Only published (and accepted for publication) journal articles, books and book chapters, conference proceedings, online reports, a degree thesis, and materials available on the website qualify for REFERENCES.

Declaration: Provide a declaration that: (i) the results are original, (ii) the same material is neither published nor under consideration for publication elsewhere, (iii) approval of all authors has been obtained, and (iv) in case the article is accepted for publication, its copyright will be assigned to the *Pakistan Academy of*

Sciences. Authors must obtain permission to reproduce, where needed, copyrighted material from other sources and ensure that no copyrights are infringed upon.

Manuscript Formatting

Manuscripts must be submitted in Microsoft Word (Latest Version .doc or .docx format); pdf files are not acceptable. Figures can be submitted separately in TIFF, GIF, JPEG, EPS, or PPT. Manuscripts, in *Times New Roman*, 1.15 spaced (but use single-space for Tables, long headings, and long captions of tables and figures). The Manuscript sections must be numbered, i.e., **1. INTRODUCTION, 2. MATERIALS AND METHODS,** and so on… (a) **Title** of the article **(**Capitalize the initial letter of each main word, font-size 16, **bold**), max 160 characters (no abbreviations or acronyms), depicting article's contents; (b) Author's complete name (font size 12, **bold**), and professional affiliation (i.e., each author's Department, Institution, Mailing address, and Email and Contact number, but no position titles) (font size 12); (c) Indicate the corresponding author with *; and (d) **Short running title**, max 50 characters (font size 10).

Headings and Subheadings (font size 11): All flush left

LEVEL-1: **ALL CAPITAL LETTERS; Bold**

Level-2: **Capitalize Each First Letter (**Except prepositions**); Bold**

Level-3: Capitalize the first letter only (Sentence case)***; Bold, Italic***

Level-4: *Run-in head*; *Italics*, *in the normal paragraph position. Capitalize the first letter only and end in a colon (i.e.,* ***:****)*

A list of REFERENCES must be prepared as under:

a. Journal Articles *(Name of journals must be stated in full)*

1. J. Rashid, A. Ahsan, M. Xu, I. Savina, and F. Rehman. Synthesis of cerium oxide embedded perovskite type bismuth ferrite nanocomposites for sonophotocatalysis of aqueous micropollutant ibuprofen. *RSC Advances* 13(4): 2574-2586 (2023).

2. A. Fayyaz, N. Ali, Z.A. Umar, H. Asghar, M. Waqas, R. Ahmed, R. Ali, and M.A. Baig. CF-LIBS based elemental analysis of Saussurea simpsoniana medicinal plant: a study on roots, seeds, and leaves. *Analytical Sciences* 40(3): 413-427 (2024).

3. W. Bialek and S. Setayeshgar. Cooperative sensitivity and noise in biochemical signaling. *Physical Review Letters* 100: 258–263 (2008).

b. Books

4. W.R. Luellen (Ed.). Fine-Tuning Your Writing. *Wise Owl Publishing Company, Madison, WI, USA* (2001).

5. U. Alon and D.N. Wegner (Eds.). An Introduction to Systems Biology: Design Principles of Biological Circuits. *Chapman & Hall/CRC, Boca Raton, FL, USA* (2006).

c. Book Chapters

6. M.S. Sarnthein, J.E. Smolen, and J.D. Stanford. Basal sauropodomorpha: historical and recent phylogenetic developments. In: The Northern North Atlantic: A Changing Environment. P.R. Schafer and W. Schluter (Eds.). *Springer, Berlin, Germany* pp. 365–410 (2000).

7. S. Brown and L.A. Boxer. Functions of Europhiles. In: Hematology, (4th ed). W.J. Williams, E. Butler, and M.A. Litchman (Eds.). *McGraw Hill, New York, USA* pp. 103–110 (1991).

d. Reports

8. M.D. Sobsey and F.K. Pfaender. Evaluation of the H_2S method for Detection of Fecal Contamination of

Drinking Water. Report No.-WHO/SDE/WSH/02.08. *Water Sanitation and Health Programme, WHO, Geneva, Switzerland* (2002).

e. Online References

These should specify the full URL for reference, please check again to confirm that the work you are citing is still accessible:

9. UNESCO. Global Education Monitoring Report 2024/5: Leadership in education−Lead for learning. *United Nations Educational, Scientific and Cultural Organization, Paris, France* (2024). https://digitallibrary.un.org/record/4066661?ln=en&v=pdf

10. L.M. Highland and P. Bobrowsky. The landslide handbook−A guide to understanding landslides. Circular 1325. *US Geological Survey, Reston, Virginia* (2008).

    https://pubs.usgs.gov/circ/1325/pdf/C1325_508.pdf

f. Conference Proceedings

11. M. Khalid, A.B. Majid, F. Mansour, and C.R. Smith. Word Representations with Recursive Neural Networks for Morphology. *27th European Conference on Signal Processing, (2nd - 6th September 2021), Madrid, Spain* (2021).

g. A Degree Thesis

12. M. Afzal. Investigation of structural and magnetic properties of nanometallic Fe-Mn Alloys. Ph.D. Thesis. *Quaid-i-Azam University, Islamabad, Pakistan* (2023).

Tables: Insert all tables as editable text, not as images. Number tables consecutively following their appearance in the text. A concise but self-explanatory heading must be given. Tables should be numbered according to the order of citation (like **Table 1.**, **Table 2.** (font size 10)). *Do not* abbreviate the word "Table" to "Tab.". Round off data to the nearest three significant digits. Provide essential explanatory footnotes, with superscript letters or symbols keyed to the data. Do not use vertical or horizontal lines, except for separating column heads from the data and at the end of the Table.

Figures: In the main text write Figure, not Fig. Figures may be printed in two sizes: column width of 8.0 cm or page width of 16.5 cm; In the Figure caption, number them as **Fig. 1.**, **Fig. 2.** Captions to Figures must be concise but self-explanatory (font size 10). Laser-printed line drawings are acceptable. Do not use lettering smaller than 9 points or unnecessarily large. Photographs must be of high quality. A scale bar should be provided on all photomicrographs. All Figures should have sufficiently high resolution (minimum 300 dpi) to enhance the readability. Figures as separate files in JPG or TIFF format may be provided.

SUBMISSION CHECKLIST

The following list will be useful during the final checking of an article before submission to the journal.

1. Manuscript in MS Word format
2. Cover Letter
3. Novelty Statement
4. Copyright Form
5. Figures in JPG or TIFF format

In case of any difficulty while submitting your manuscript, please get in touch with:

Editor-in-Chief

Pakistan Academy of Sciences
3-Constitution Avenue,
G-5/2, Islamabad, Pakistan
Email: editor@paspk.org
Tel: +92-51-920 7140
Websites: http://www.paspk.org/proceedings/; http://ppaspk.org/

PROCEEDINGS OF THE
PAKISTAN ACADEMY OF SCIENCES: PART A
Physical and Computational Sciences

CONTENTS

Volume 62, No. 2, June 2025 **Page**

Research Articles

Instructions for Authors

PAKISTAN ACADEMY OF SCIENCES, ISLAMABAD, PAKISTAN

HEC Recognized; Scopus Indexed

Websites: http://www.paspk.org/proceedings/; http://ppaspk.org